FINAL REPORT

ANNULAR MOMENTUM CONTROL DEVICE (AMCD)

PREPARED FOR

NATIONAL AERONAUTICS AND SPACE ADMINISTRATION

LANGLEY RESEARCH CENTER

HAMPTON, VIRGINIA

MAR 1976
RECEIVED
NASA STI FACILITY
INPUT BRANCH

Ball Brothers Research Corporation
SUBSIDIARY OF BALL CORPORATION

Aerospace Division

BOULDER, COLORADO 80302

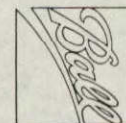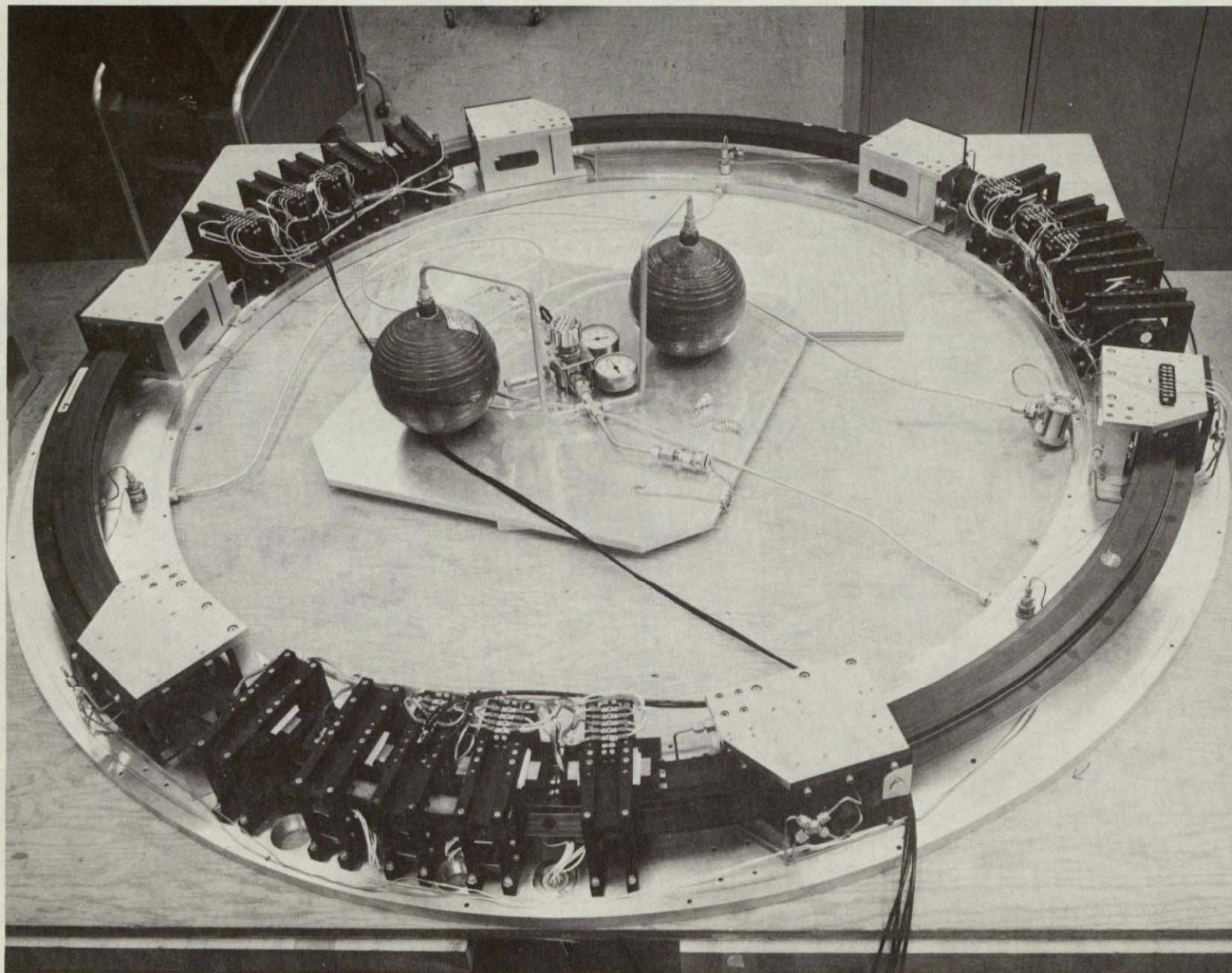NASA CR-144917

FINAL REPORT

ANNULAR MOMENTUM CONTROL DEVICE (AMCD) .

VOLUME I: LABORATORY MODEL DEVELOPMENT

Prepared under Contract No. NAS 1-12529 by
Ball Brothers Research Corporation
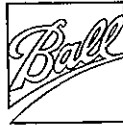Boulder, Colorado 80302

for

NATIONAL AERONAUTICS AND SPACE ADMINISTRATION

The AMCD in Final Stages of Assembly

SUMMARY

The annular momentum control device (AMCD) is a thin hoop-like wheel with neither shaft nor spokes (see Frontispiece). The wheel floats in a magnetic field and can be rotated by a segmented motor. Potential advantages of such a wheel are low weight, configuration flexibility, a wheel that stiffens with increased speed, vibration isolation, and increased reliability.

The AMCD is nearly 2 meters (6 feet) in diameter. An annular aluminum baseplate supports the entire wheel assembly. Vacuum operation is possible by enclosing the wheel in an annular housing attached to the baseplate. The rotor or "rim" has a diameter of about 1.6 meters (63 inches) and consists principally of graphite-epoxy composite material. It weighs 22.5 kilograms (49.5 pounds) and is strong enough to be spun at 3000 rpm. At this speed, it can store 2200 N-m-s (3000 ft-lb-sec) of angular momentum. A system of pneumatic bearings can support the rim in the event of a magnetic suspension failure.

The magnetic suspension system supports the rim both axially and radially at three points. Combinations of permanent magnets and electromagnets at each of the three suspension stations exert forces on ferrite bands imbedded in the rotating rim. The magnetic gaps are about 0.25 cm (0.1 inch) above, below, and inside the rim. The gaps are maintained by servo loops with 50 hertz bandwidths that respond to error signals generated by inductive sensors. The servo loops can be operated in either "positioning" or "zero-power" modes.

The rim is accelerated and decelerated by a large diameter, segmented, brushless d.c. motor. Electromagnet stator segments are placed at each suspension station and interact with samarium cobalt permanent magnets placed every 7.3 cm (2.9 inches) along the periphery of the rim. Commutation is achieved by Hall sensors that detect the passing permanent magnets.

Volume I of this report describes the analysis, design, fabrication, and testing of the laboratory model of the AMCD. Volume II contains a conceptual design and set of dynamic equations of a gimbaled AMCD adapted to a Large Space Telescope (LST). Such a system could provide maneuver capability and precision pointing by means of one external gimbal, wheel speed control, and small motions of the rim within the magnetic gap.
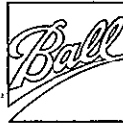
TABLE OF CONTENTS

APPENDICES

ACKNOWLEDGMENTS

The AMCD development to date has been the result of the efforts of a great many people. At BBRC, Frank Manders with help from Dick Mathews lead the mechanical design and fabrication effort, Dick Woolley strongly influenced the magnetic design and overall configuration, Jerry Wedlake developed the drive system, Glen King performed the dynamic analyses and Dave Giandinoto designed much of the interfacing electronics and did the final system integration.

At Cambion, Paul Simpson managed the magnetic suspension work with technical consulting provided by Joe Lyman and Lloyd Perper.

The rim fabrication at Bristol was headed by Tom Laidlaw with analytical assistance from Keith Kedward.

Analytic design of the back-up bearings at Shaker Research was conducted by Dr. Coda Pan and Warren Waldron.

The "customer" had a strong influence on the final system. At Goddard Space Flight Center, Phil Studer provided valuable suggestions on all magnetic aspects and the drive motor in particular. The primary influences and directions came, of course, from Nelson Groom and Dr. Willard Anderson of Langley Research Center who conceived of the AMCD and fostered its development.

My thanks to all of these people.

Carl Henrikson
AMCD Project Manager

1.0   INTRODUCTION

The AMCD concept was originated at the Langley Research Center of the National Aeronautics and Space Administration (Reference 1). Analysis, design, fabrication, and testing of development hardware was begun under contract to Ball Brothers Research Corporation in July of 1973. The contract was jointly sponsored by the Langley Research Center and the Goddard Spaceflight Center. The contract work statement was also a joint effort with the Goddard Spaceflight Center providing technical inputs on the magnetic bearings and drive motor portions. Hardware was delivered in February of 1975.

Several key subcontractors were used by BBRC during the program. Principal among these were:

1. Cambridge Thermionic Corporation (Cambion), Cambridge, Massachusetts - Development of the magnetic suspension system.

.2. Bristol Aerospace Limited, Winnipeg, Canada - Analysis and fabrication of the rim.

3. Shaker Research Corporation, Ballston Lake, New York - Design of the back-up air-bearing system.

These subcontractors performed well and made major contributions to the success of the program. One subcontract did not go well and caused a major delay in the program. Failure of the subcontractor for the baseplate and vacuum enclosure to meet flatness requirements necessitated rejection of the parts and placement of the subcontract with another firm.

This report is a description of the major hardware items and their design considerations. Details of the "as-delivered" hardware may be found in the Operations and Maintenance Manual that was delivered with the hardware.

The report is divided into four main parts covering the concept, the mechanical systems, the suspension system, and the drive system. Appendices are used to cover some of the details of the servo control loops.

2.0 THE AMCD CONCEPT

A purely annular wheel has many advantages. Principal among these is that all the rotating mass is at the greatest radius and hence can produce the greatest angular momentum storage. The shaft and spokes of a conventional wheel add weight but very little angular momentum storage.

Ball-bearing annular wheels have never been tried and for one obvious reason: The losses associated with a large diameter ball bearing would be intolerable. In order to make annular wheels practical, a low-loss magnetic suspension of the rotor (or rim) is necessary. This, then, is the AMCD concept: a narrow, annular rim supported by a magnetic suspension system.

Several other advantages accrue from the AMCD concept. First of all, conventional size constraints are removed. The wheel does not have to operate in an enclosure to preserve lubricants. If the diameter is increased greatly, the space is not wasted because a spacecraft or part of a spacecraft can be placed inside the wheel. Furthermore, motivation exists to go to larger wheels. It can be shown that for a given stress level in the rim, the mass efficiency of the rim increases as the diameter increases. The offsetting effects of increased stator weight can be alleviated by using basic spacecraft structure to support the stator elements. A further advantage of larger diameter is increased moment arm for spin and precessional torquing.

Another set of advantages of the AMCD concept is a result of the relatively thin annular rim. The stresses in such a shape are predominantly circumferential so that the structure lends itself to filament or tape wound composite materials. Furthermore, as spin rate increases, the rim tends to flatten and reduce dynamic imbalance. Also, it tends to become "stiffer" so that structrual

resonant frequencies increase. In fact, it can be shown that .
the conventional crossover frequency of a spinning wheel at
which the spin frequency becomes equal to the rotor structural
frequency cannot occur for an AMCD. The structural frequencies
are always greater than spin frequency no matter how limber the
rim is at .zero spin rate.

The use of a magnetic suspension gives rise to another set of
advantages. First, the suspension is relatively soft and forms
a sort of isolator between the rim and the spacecraft to which
it is attached. Any vibrations of the rim will be greatly at-
tenuated. This effect can be enhanced by proper filtering at
multiples of spin rate. The suspension is also a smooth, linear
force-producing system without mechanical nonlinearities such
as stiction. The result is that small, precision precessional
torques can be created by gimbaling the rim in the magnetic gaps.
The final advantage is related to the long life and, perhaps even
more important, predictable long-life capability of a magnetic
suspension system vis-a-vis a ball bearing. Ball bearing life-
times are short, dependent on number of revolutions, rotational
speed, and very susceptible to contamination. The lifetime of a
magnetic suspension is a function of the failure rate of electronic
components, an area that has been the subject of a great deal of
study. Moreover, redundant suspensions are fairly simple to
mechanize.
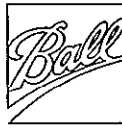
3.0 MECHANICAL SYSTEMS

The AMCD Mechanical Systems consist of 1) the rotor (or "rim"), 2) the back-up air bearing system and 3) the mounting base and vacuum enclosure.

The rim provides the angular momentum storage capability for the system. Embedded into the rim are ferrite rings and samarium cobalt permanent magnets. Three ferrite rings, composed of segments, located on each axial surface and on the inside radial surface react with the magnetic suspension system. Seventy-two permanent magnets, located near the periphery of the rim react with the segmented drive system.

The back-up air bearing system, initiated in the event of a magnetic suspension failure, is designed to slow and support the rim. The design provides hydrostatic air pads for radial control and hydrodynamic air pads for axial control.

The mounting base and vacuum enclosure completely surround the rim, magnetic suspension and motor components, and provide the mounting points for the torque measuring fixture brackets. The annular mounting base supports the magnetic suspension and motor lattice structure. The annular vacuum enclosure, U-shaped in cross-section, is bolted to the mounting base providing the capability to operate the rim in a vacuum and to add structural rigidity. The vacuum environment is necessary to reduce rim air drag.

3.1 Rim

The final rim configuration, Figure 3-1 shows that all components embedded into the rim are completely supported. The distance between the permanent magnets and ferrite bands is maximized within the dimensional constraints of the rim.
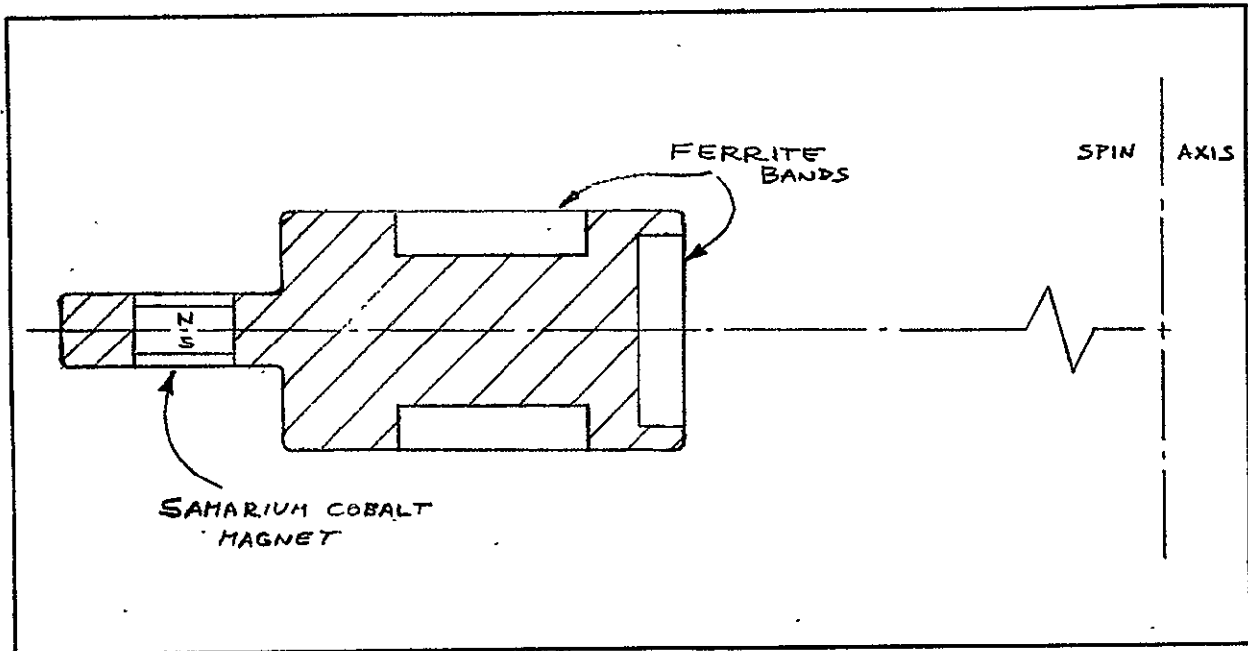
Figure 3-1 Rîm Confîguratîon

"Centrifugal" accelerations cause forces on the embedded com-
ponents which are reacted directly by the base rim material
minimizing the stresses on the adhesive which bonds the components.
to the rim. The samarium cobalt permanent magnets are spaced
a minimum of 0.85 inches from the closest ferrite band to mini-
mize the coupling between the permanent magnets and the mag-
netic suspension system.

The primary function of the rim is to provide maximum angular
momentum storage capacity within dimensional and weight con-
straints. The selection of the rim material, graphite filament -
epoxy laminate, is consistent with this function. The specific
momentum of a flywheel (H/M) is related to material characteristics
of the rim as follows:

$$H/M \propto \sqrt{\sigma/\rho} \qquad\qquad (3\text{-}1)$$

where σ is working stress in flywheel

ρ is flywheel material density

Hence, a high-strength, low-density material is ideal for a low-weight flywheel.

Table 3-1 shows the relationship of material ultimate tensile strength to material density for acceptable rim materials.

Table 3-1
RIM MATERIAL STRENGTH TO DENSITY RATIO

MATERIAL	STRENGTH/DENSITY (IN x 10^6)
Graphite A-S/Epoxy	3.6
Glass/Epoxy	3.4
Boron/Epoxy	3.1
Graphite M-S/Epoxy	3.0
Graphite HM-S/Epoxy	1.8
Beryllium*	1.0
6A1-4V Titanium*	1.0
7075 Aluminum*	0.8

*Not in Composite Form

Graphite AS fiber - epoxy laminate, therefore, will provide the largest specific momentum for the system. Graphite filament-epoxy laminate also has a relatively high elastic modulus (16×10^6 PSI), thus providing relatively low radial growth at high speeds. Furthermore, graphite-epoxy laminate is non-magnetic and non-conducting, essential characteristics for low drag operation of the magnetic suspension system.

3.1.1   Rim Description

The rim consists of three bands of ferrite material, made up
of 180 segments each, and 72 samarium cobalt permanent magnets
embedded and bonded into the AS graphite filament - DX210 epoxy
rim material. Figure 3-2 shows the rim dimensions.

The ferrite rings and permanent magnets are bonded to the basic
rim with Fuller 7004 adhesive. The rim is composed of two basic
rectangular cross-sections, the first, and larger, contains the
bulk of the graphite-epoxy material and the ferrite bands; the
second, smaller, section contains the remaining material and
the samarium cobalt permanent magnets.

The larger section has a cross-section 5.3 cm (2.1 inches) in radial
length by 3.18 cm (1.25 inches) deep, with an inner diameter of
154 cm (60.8 inches). Three channels are machined into this
section 2.54 cm (1.0 inches) wide by 0.57 cm (0.225 inches) deep,
to contain the ferrite bands. The smaller section, integral with
the larger, is axially centered, 2.8 cm (1.1 inches) in radial
length by 0.95 cm (0.375 inches) deep, with an outer diameter of
171 cm (67.25) inches. This section contains 72 holes which contain
the permanent magnets.

The samarium cobalt permanent magnets are 1.4 cm (0.55 inches) in
diameter by 0.64 cm (0.25 inches) long. The axial and radial
ferrite segments are shown in Figures 3-3 and 3-4, respectively.

The ferrite segments are machined from Ferroxcube 3C5 material.
The axial segment is slightly keystone in shape to minimize gap
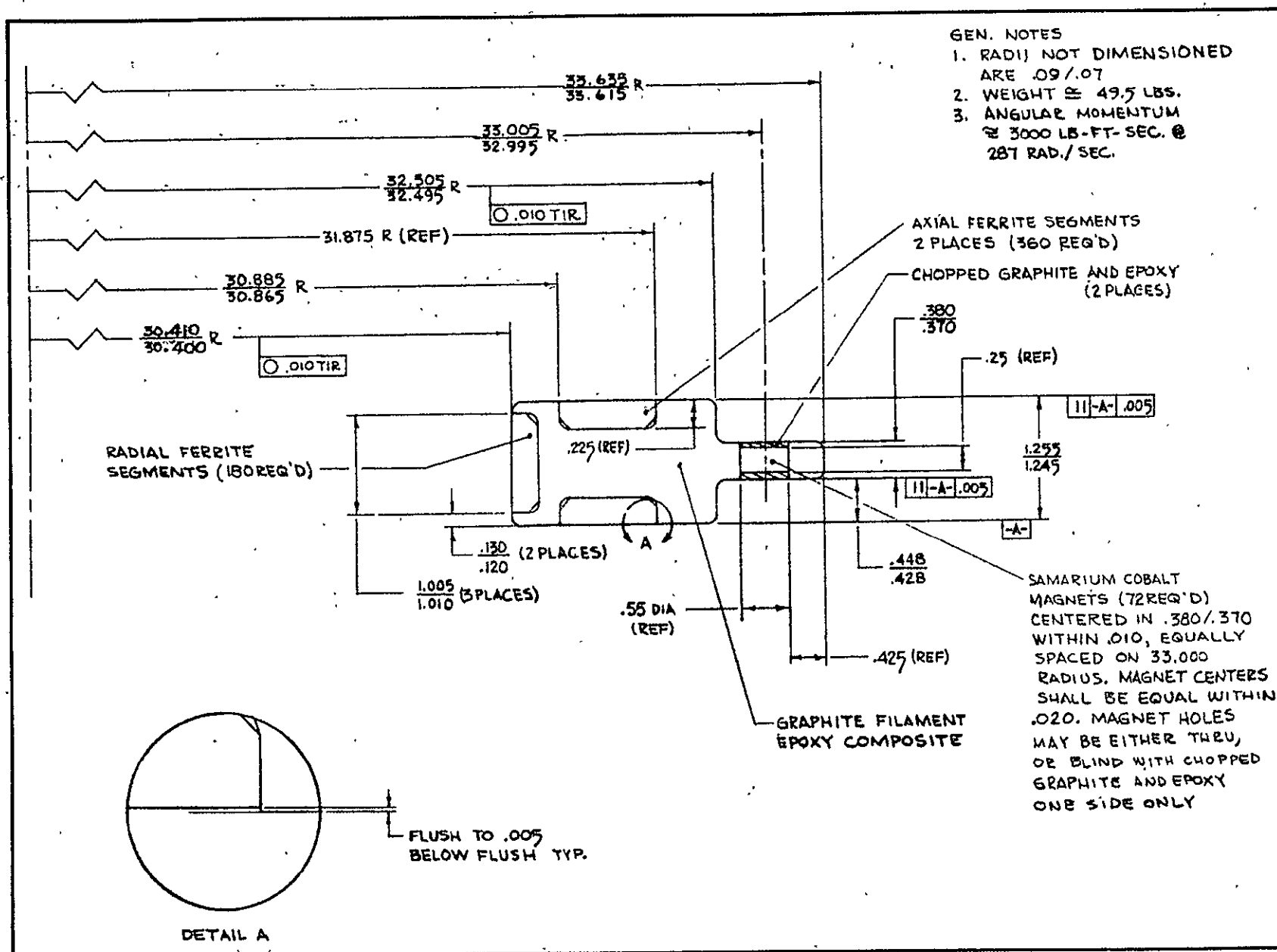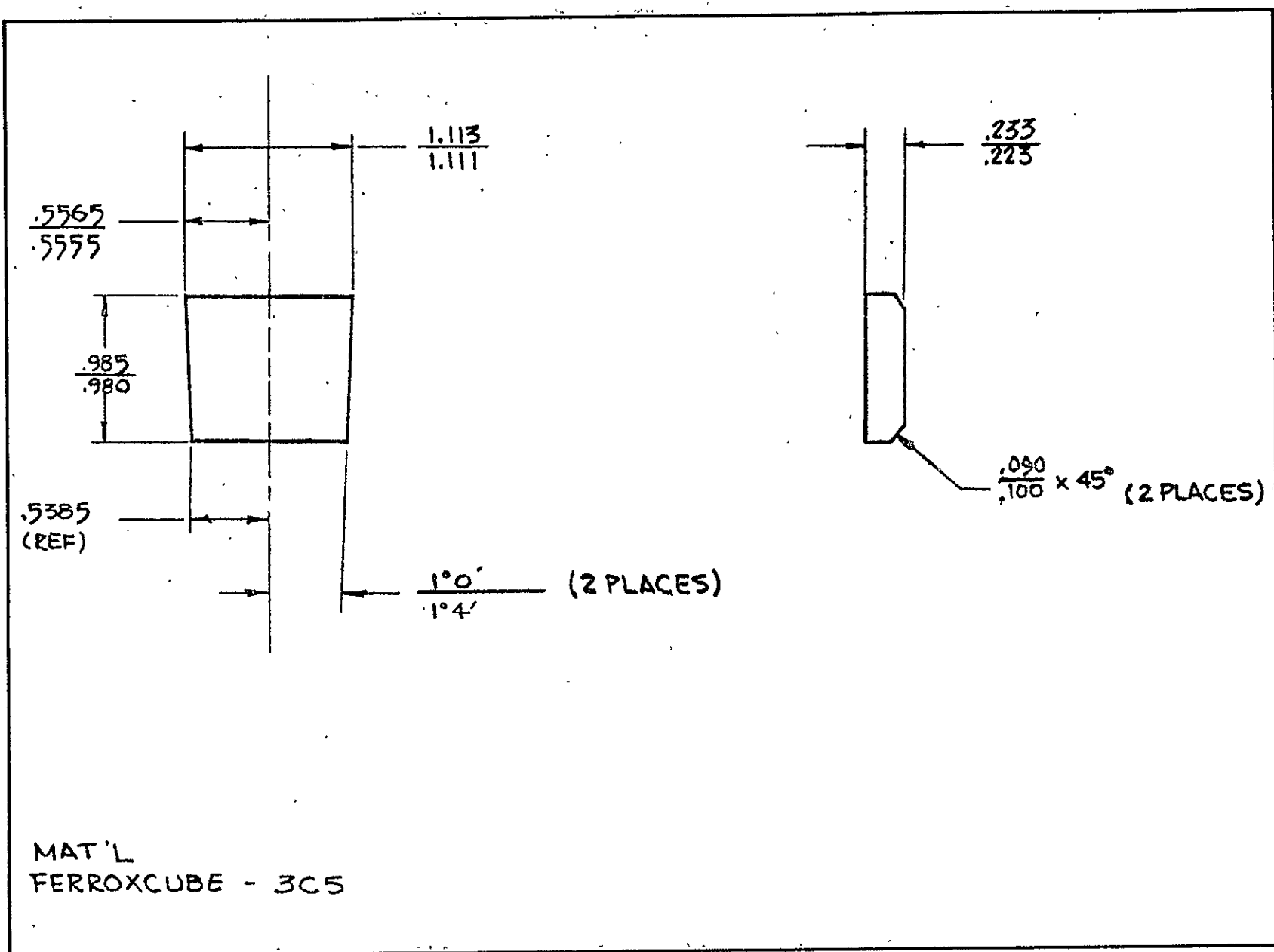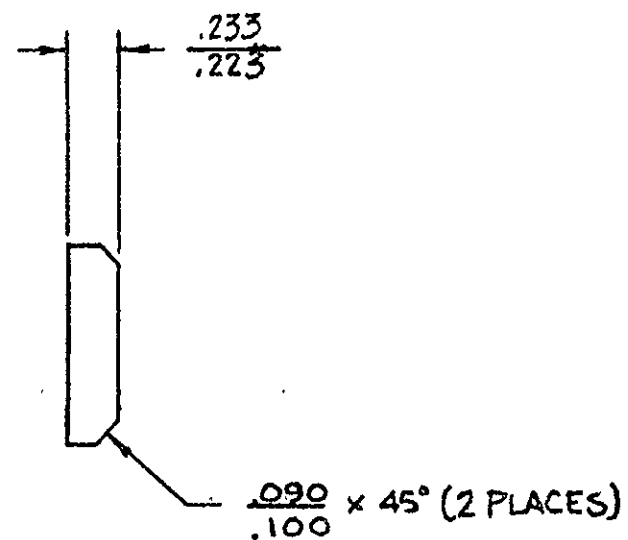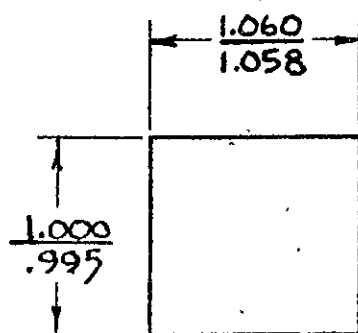distances. Each segment occupies 2 degrees of the band circum-
ference.

GEN. NOTES
1. RADII NOT DIMENSIONED
   ARE .09/.07
2. WEIGHT ≅ 49.5 LBS.
3. ANGULAR MOMENTUM
   ≈ 3000 LB-FT-SEC. @
   287 RAD./SEC.

33.638 R
33.615

33.005 R
32.995

32.505 R
32.495

⌀ .010 TIR.

31.875 R (REF)

30.885 R
30.865

30.410 R
30.400

⌀ .010 TIR

AXIAL FERRITE SEGMENTS
2 PLACES (360 REQ'D)

CHOPPED GRAPHITE AND EPOXY
(2 PLACES)

.380
.370

.25 (REF)

‖ -A- .005

1.255
1.245

‖ -A- .005

RADIAL FERRITE
SEGMENTS (180 REQ'D)

.225 (REF)

-A-

.130 (2 PLACES)
.120

.448
.428

1.005 (3 PLACES)
1.010

.55 DIA
(REF)

.425 (REF)

SAMARIUM COBALT
MAGNETS (72 REQ'D)
CENTERED IN .380/.370
WITHIN .010, EQUALLY
SPACED ON 33.000
RADIUS. MAGNET CENTERS
SHALL BE EQUAL WITHIN
.020. MAGNET HOLES
MAY BE EITHER THRU,
OR BLIND WITH CHOPPED
GRAPHITE AND EPOXY
ONE SIDE ONLY

GRAPHITE FILAMENT
EPOXY COMPOSITE

A

FLUSH TO .005
BELOW FLUSH TYP.

DETAIL A

Figure 3-2   Rim Dimensions

1.113
1.111

.5565
.5555

.233
.223

.985
.980

.090
.100 × 45° (2 PLACES)

.5385
(REF)

1° 0'
1° 4' (2 PLACES)

MAT'L
FERROXCUBE - 3C5

Figure 3-3   Axial Ferrite Segment

1.060
1.058

1.000
.995

.233
.223

.090
.100 × 45° (2 PLACES)

MAT'L
FERROXCUBE - 3C5

Figure 3-4 Radial Ferrite Segment.

The radial segment is rectangular in cross-section and when bonded in place produces a small wedge-shaped gap between segments. Each radial segment represents 2 degrees of the band circumference.

3.1.2   Rim Fabrication

The AMCD rim was fabricated by Bristol Aerospace Limited, Winnipeg, Canada. The material, AS graphite filament tape impregnated with DX210 resin, was wrapped on a special tool producing 100 percent circumferential fibers with a volume fraction of graphite of 55 percent.

The oversized cross-section rim was wound in 15 separate layers. Each layer was "B" stage cured with the following temperature cycle.
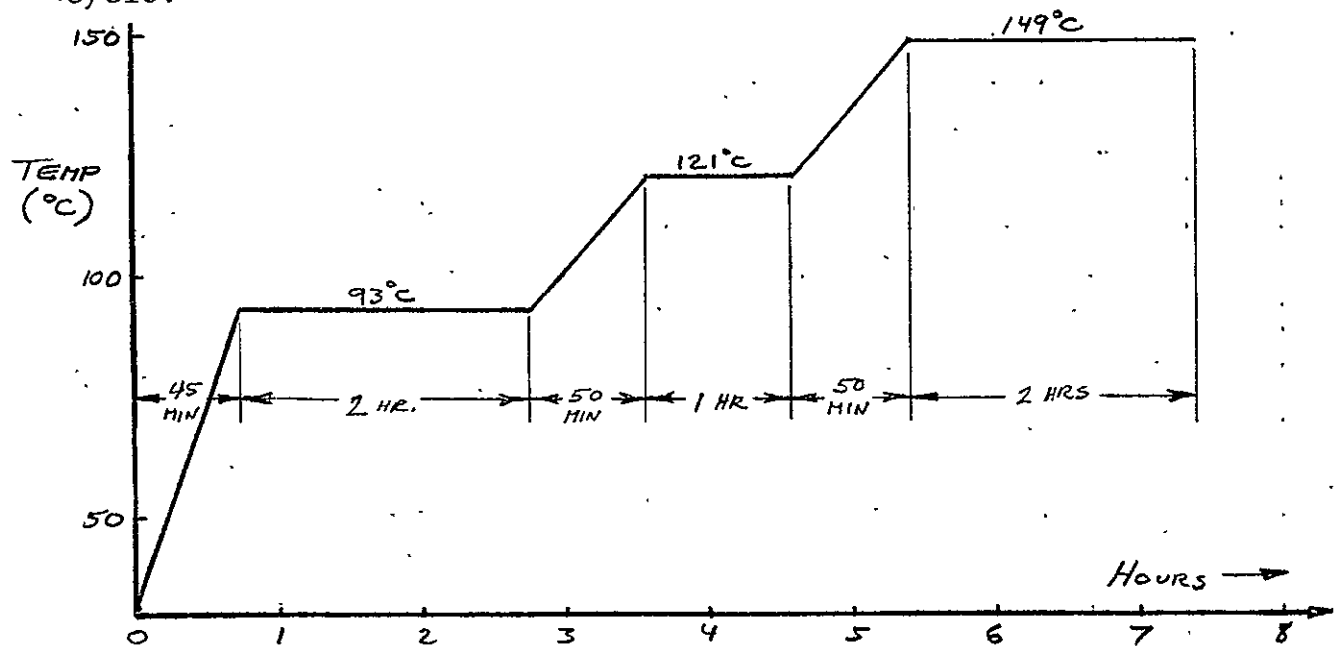
The post cure, after the fifteenth layer, was identical to the "B" stage cure except, the temperature was increased to 177°C in 50 minutes and held at 177°C for 2 hours after the 149°C exposure.

Figure 3-5 shows the specially constructed tool, containing heaters and insulation for "B" stage and final cure cycles.

The rim was removed from the tool and machined to nearly the final dimensions including ferrite channels and permanent magnet holes. These operations are shown in Figures 3-6 and 3-7.

The ferrite segments and magnets were bonded in place with Fuller 7004 adhesive and cured. The magnets were placed in the rim with alternating North-South poles and the ends were covered with a 0.16 cm (1/16 inch) thickness of chopped AS graphite-DX210 resin and cured. After final cure, the rim was machined (by grinding) to final dimension. The rim was coated with a 0.005 cm (0.002 inch) thick layer of Fuller 7220 adhesive as a final step to minimize rim water absorption. Figure 3-7A shows the final rim results.

3.1.3   Rim Analysis

The rim analysis, conducted by Bristol Aerospace, predicted the rim maximum stress and radial growth to be 38,250 N/cm^2 (55,434 PSI) and .3 cm (0.117 inches), respectively.

The rim was modelled using axisymmetric finite elements using the ANSYS system. The model characterizes the heterogeneity of the structure (including the ferrite bands and magnets) and the orthotropic elastic properties of the graphite-epoxy composite.

The results of the analysis are summarized in Table 3-2 and in Figures 3-8, 3-9 and 3-10 at a rim speed of 366 meters per second (1200 feet per second).
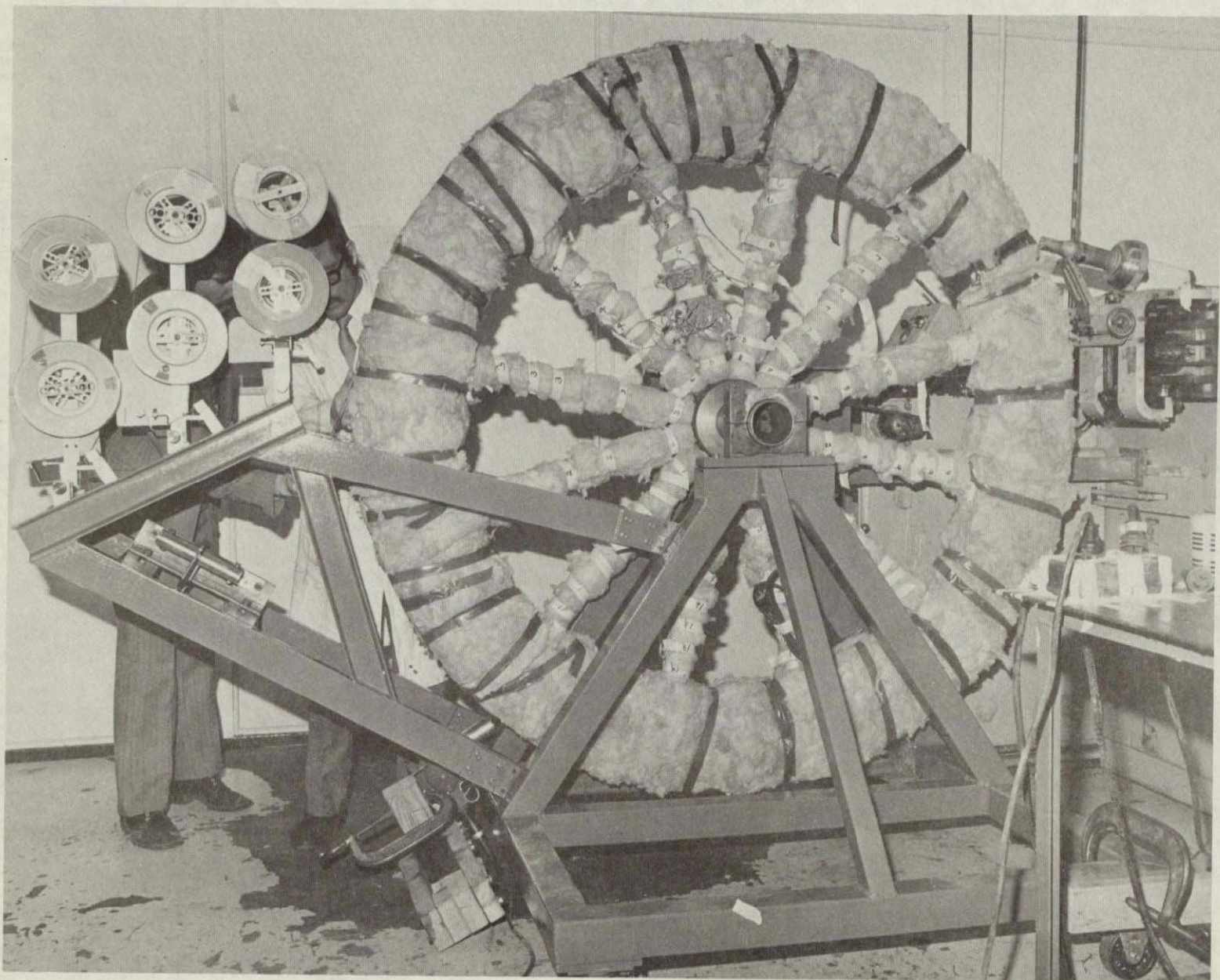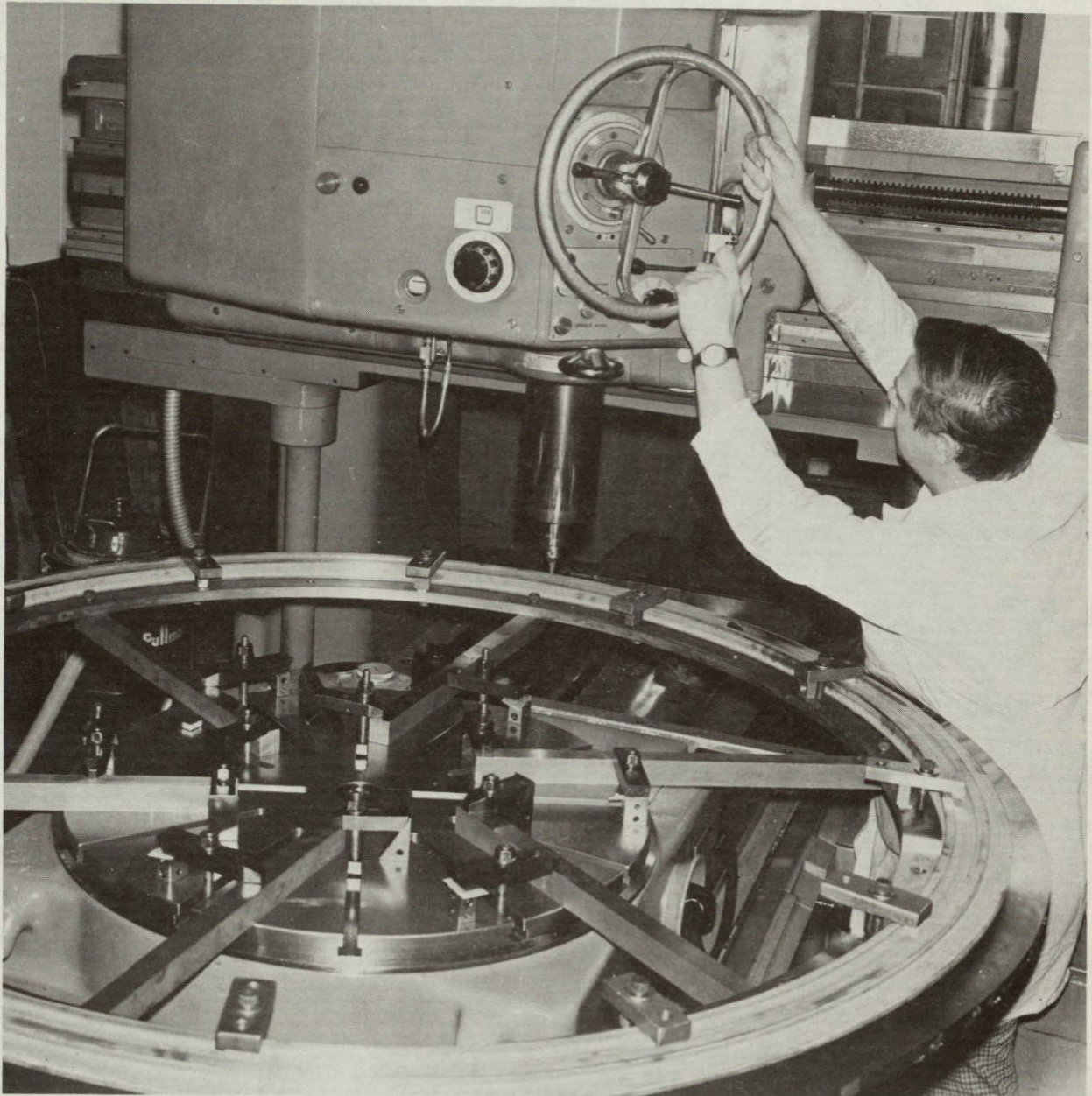
Figure 3-5 Lay-up Tool

F76-02

Figure 3-6   Rim Machining Operations
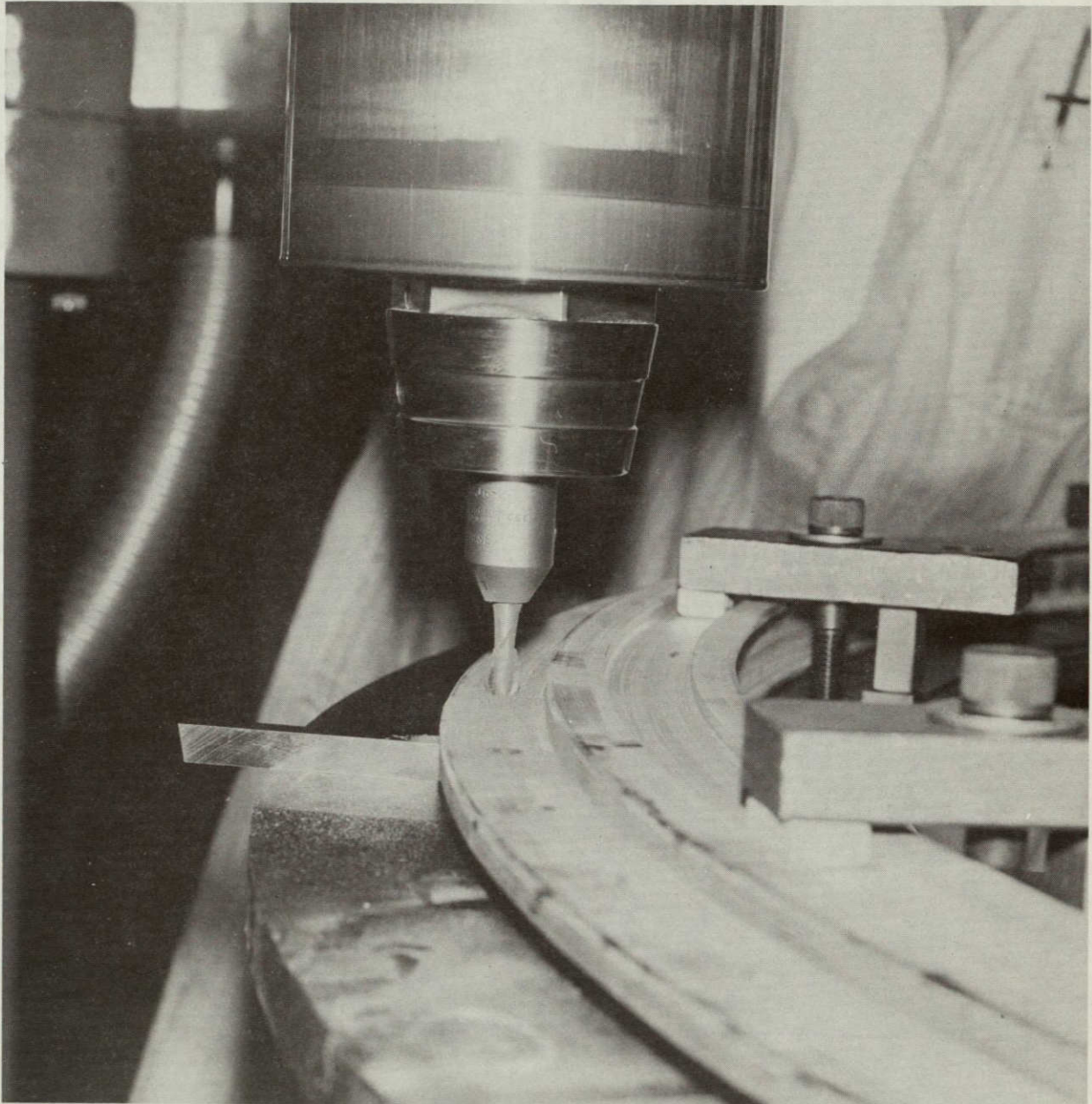
Figure 3-7 Drilling Permanent Magnet Holes in the Rim

STRESS COMPONENT	LOCATION	MAGNITUDE (PSI)
Radial or 'X' stress	carbon/epoxy "	+460 (max)* −891 (min)
Axial or 'Y' stress	carbon/epoxy "	+491 (max)* −433 (min)
Shear or 'XY' stress	carbon/epoxy "	+390 (max) −176 (min)
Hoop or 'Z' stress	carbon/epoxy "	+55,434 (max) 0 (min)
Radial Displacement (inches)	inner surface outer surface	+0.1166 (max) −0.1130 (min)

Table 3-2

MAXIMUM VALUES OF STRESS/DISPLACEMENT
AT 1200 FT/SEC. RIM SPEED

STEP=   1 ITERATION=   1   4000.00

X=55433
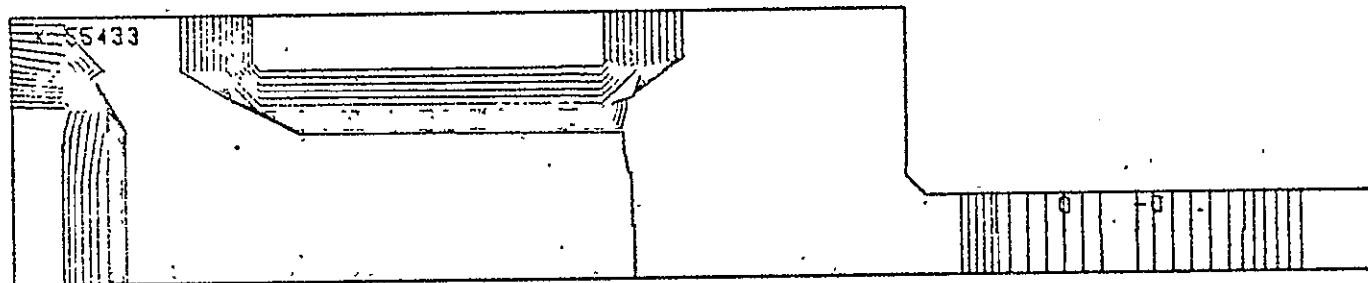
AMCO ANALYSIS   BRISTOL AEROSPACE LTD.   OCT. 73

HOOP STRESS   ANSYS   5
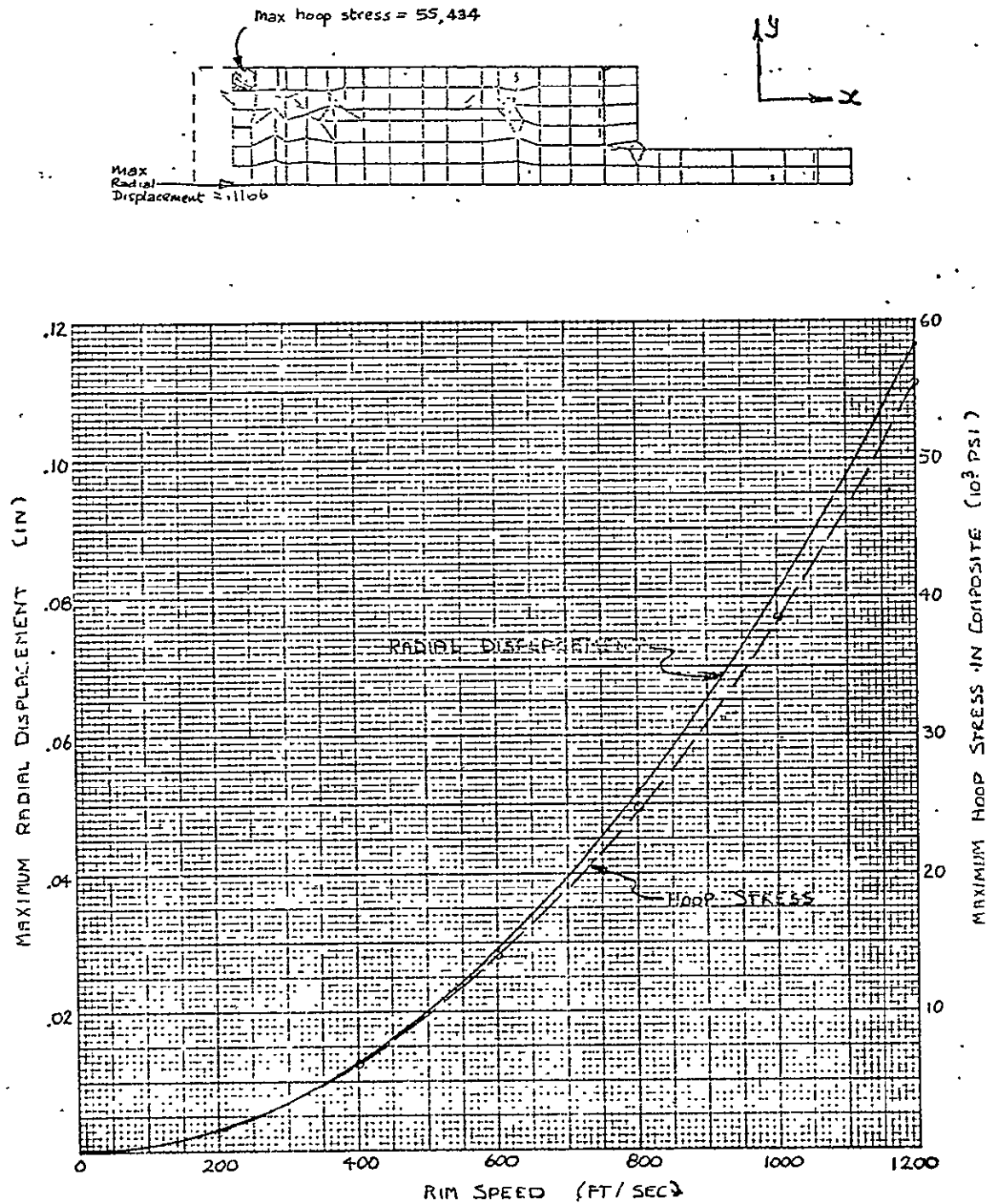
Figure 3-8 'Z' or Hoop Stress Contour Plot
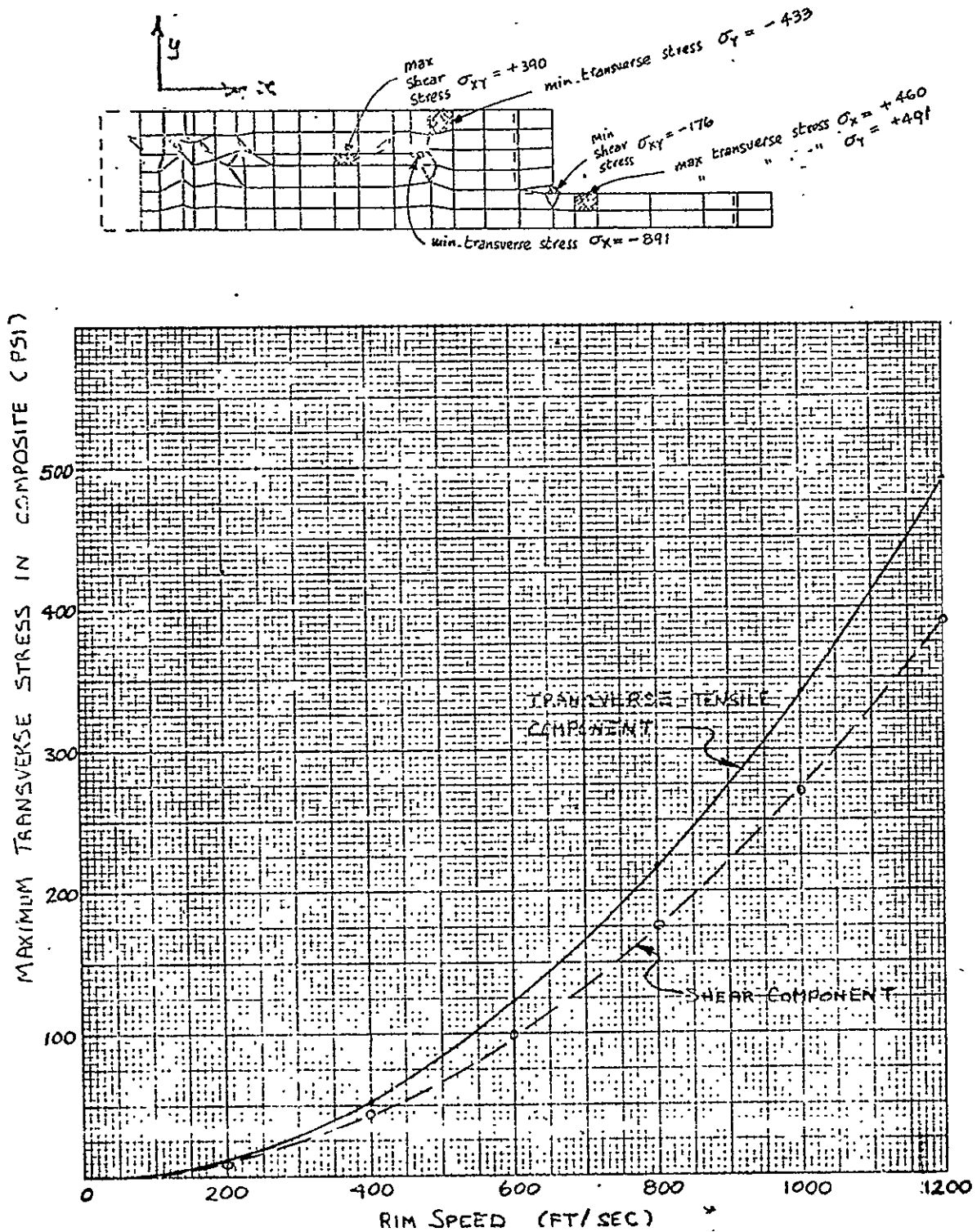
Figure 3-9 Hoop Stress and Growth With Speed

Figure 3-10 Transverse Stress Components With Speed

Figure 3-8 shows the computer-drawn plot of constant hoop tensile stress contours, the maximum being 38,252 N/cm^2 (55,438 PSI) occurring at the top and bottom inside corner.

Figure 3-9 shows the relationship of radial growth and hoop stress as a function of rim tip speed.

Figure 3-10 shows the relationship of transverse stress components with speed.

Since the material, void free, is capable of withstanding 110,400 N/cm^2 (160,000 PSI) in tension and 8280 N/cm^2 (12,000 PSI) in shear, the safety factor is 2.8 minimum. On a sample basis, the void fraction was determined to be less than 0.4 percent.

3.2:   Back-Up Air Bearing System

The design of the back-up air bearing system was completed and analyzed by Shaker Research Corporation, Ballston Lake, New York.

The back-up air bearing (BUB) system consists of six hydro-static radial pads and twelve hydrodynamic axial pads. These are arranged in six BUB sets consisting of two axial (one upper and one lower) and one radial pad and located at either end of a magnetic support station. Each BUB set is approximately 60 degrees from the adjacent set. The bearings are deployed toward the rim by air pressure when predetermined rim displacement limits are exceeded. The introduction of air through the pads as well as through a pneumatically operated valve in the vacuum enclosure provides the fluid for the BUB system and also introduces air drag for a faster coast-down. Hydrostatic bearings were selected for radial use instead of hydrodynamic types because the rather small rim depth (1.25 inches) allows insufficient area to produce the required reaction forces. The back-up bearing system is shown in Figures 3-11 and 3-12.
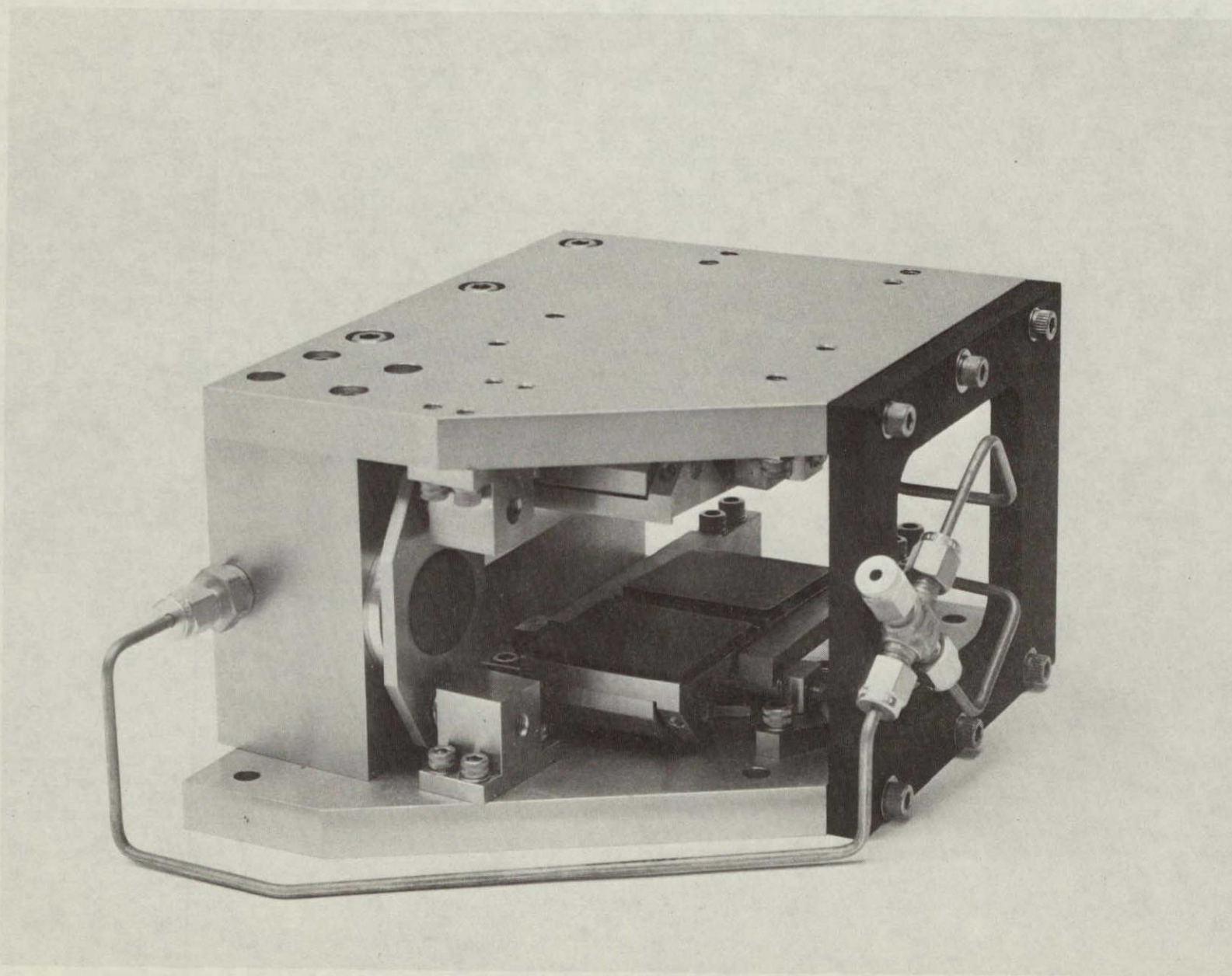
SECTION B-B

SECTION A-A

Figure 3-11 AMCD Back-Up Bearing Layout Drawing

3-18
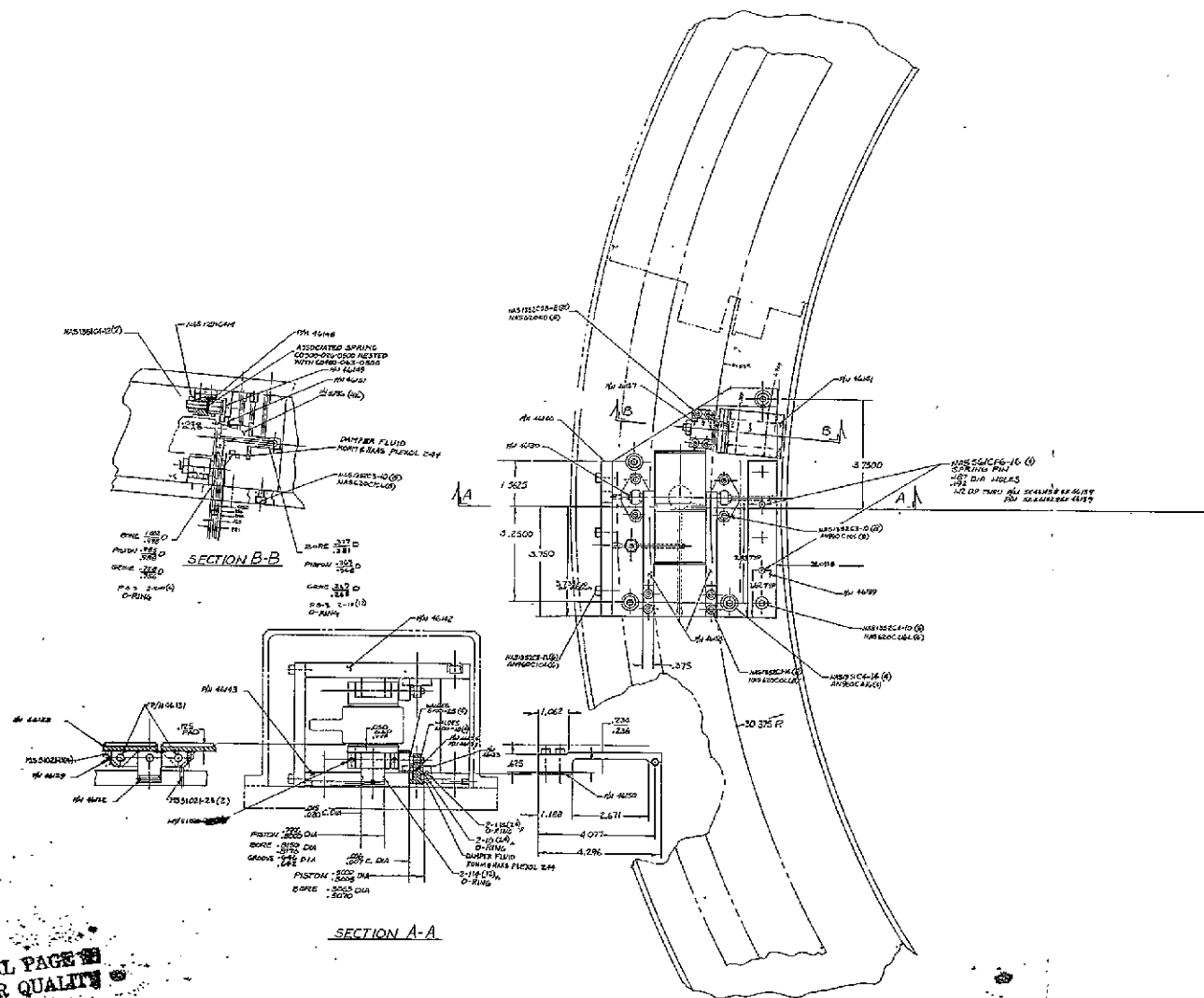
Figure 12   Back-Up Bearing System

3.2.1   Hydrostatic Radial Bearings

The movable radial pads are designed to minimize air flow and maximize air bearing rim reaction forces. The radial pads provide a centering effect on the rim to minimize dynamic and magnetic unbalance forces.

In the normal magnetic suspension mode, the radial pads are held away from the rim and against stops by a set of nested compression springs (total of 22 N (5.0 pounds) of preload). When the radial system, Figure 3-11, is activated, 207 N/cm^2 (300 psig) air is introduced to the pad piston cylinder, which moves the pad outward toward the rim. The piston chamber is ported to the pad surface through a 0.033 cm (0.012 to 0.014 inch) diameter orifice. A sealed, oil-filled dashpot between the piston and pad controls the deployment velocity.

Figure 3-13 shows the relationship between radial pad force and gas flow versus film thickness for various orifice diameters. Because of limited gas available, the smaller orifice diameters were selected.

Since the rim is not at constant radius (because of radial growths), film thickness and flow vary with rim speed. Figure 3-14 shows the relationship fo film thickness and flow versus rim speed.

3.2.2   Hydrodynamic Axial Bearings

Movable, tilt type, axial hydrodynamic pads were used since the rim radial width is large and because of the limited bearing air supply. The axial pads are slightly crowned and combined with the tilt feature are self aligning.

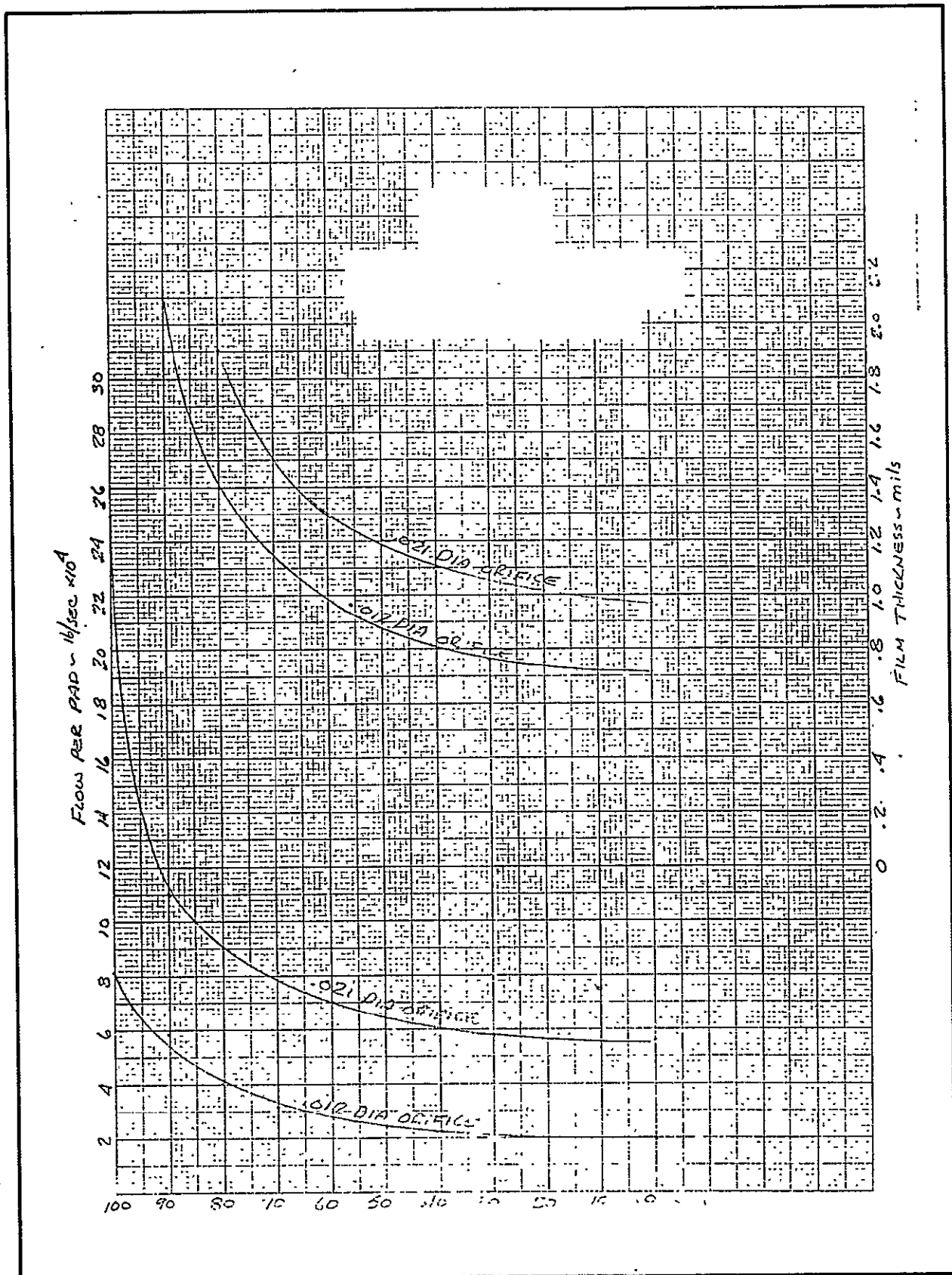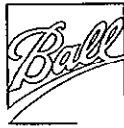Figure 3-13 Single Pad Force and Flow

Figure 3-14   Radial Air Pad Flow and Film Thickness With Rim Centered

In the normal magnetic suspension mode, the axial pads are held
against stops by a flexural spring. The axial system is deployed
in much the same manner as the radial system. When a magnetic
suspension anomaly is detected, the vacuum enclosure is flooded
with external air thus providing the film for the axial bearings.

Figure 3-15, shows the relationship of film thickness with rim
speed. Since the film will support the rim to about 15 radians
per second, the pads are designed to accept several contacts before
replacement is necessary.

3.2.3   Back-Up Bearing Pads

The primary objective in designing the pad material was to pro-
vide a material which would wear smoothly without damage to the
rim or to the pad itself. Sacrificial bearing materials have
been used in gas bearings in the past which exhibit the necessary
qualitites. The material used in the back-up bearings is an epoxy
resin heavily filled with aluminum powder, aluminum oxide power
and molybdenum disulphide powder. The mixture is poured into
silicone rubber molds, degassed in a vacuum chamber, then heat-
cured. The pads are then machined.

When the spinning rim contacts the pads the pad will wear smoothly
and rapidly, acquiring a high polish and yielding a fine dust.
The rim surface should be undamaged by the contact. The aluminum
filler provides high thermal conductivity to sink the heat generated
by the rim contact. The aluminum oxide provides dimensional
stability so the pad will withstand the thermal shock generated
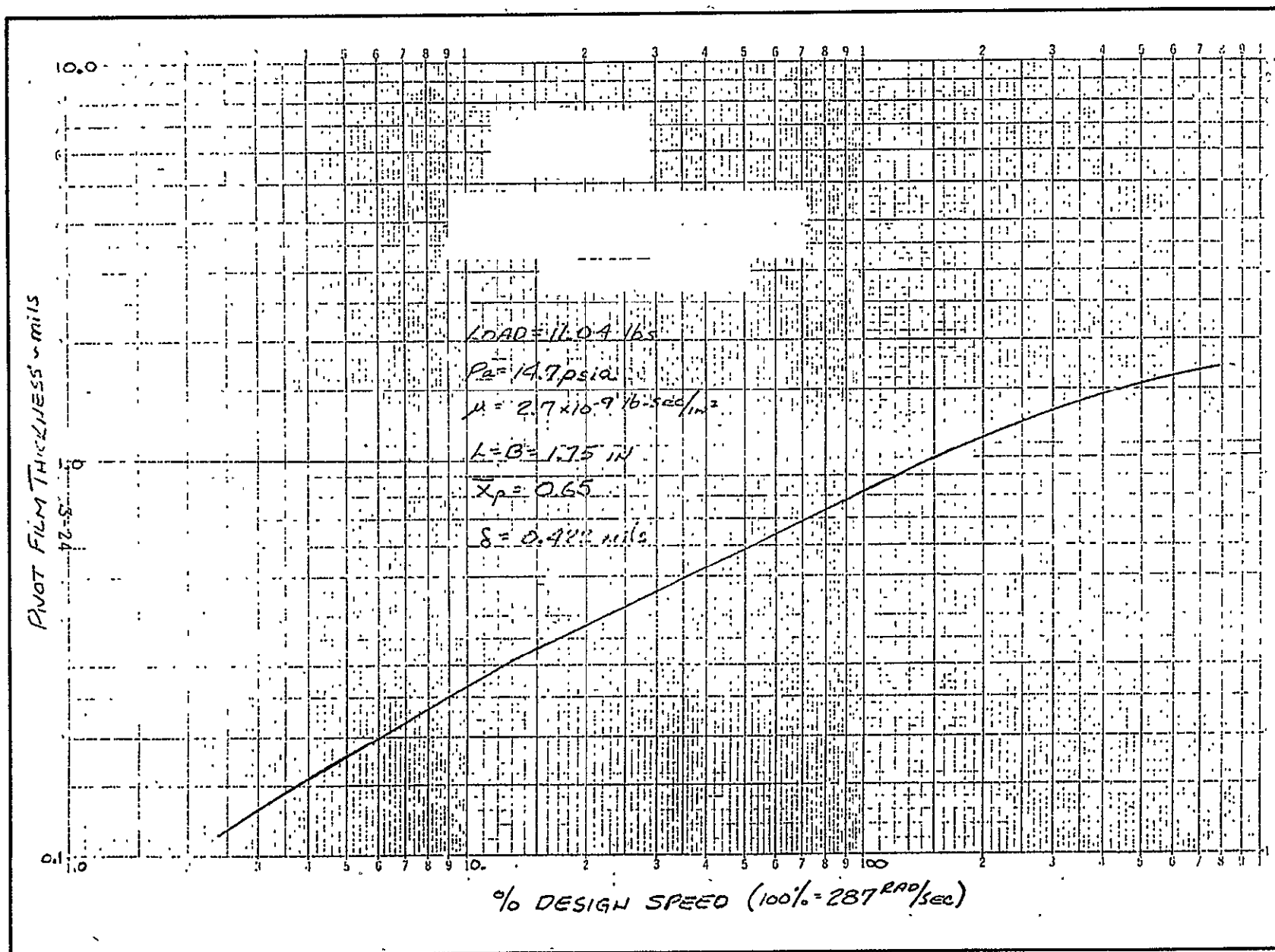by the rim contact.

Figure 3-15 Axial Pad Film Thickness Versus Speed

4.0   SUSPENSION SYSTEM

4.1   System Description

The suspension system consists of three suspension stations
placed symmetrically about the rim. At each suspension station,
the rim can be pulled in either axial direction or radially
inward by magnets. A total of 12 magnets are arranged in sets
of four each to pull in these three directions (up, down, and
inward). The eight axial magnets are driven in concert by one
set of electronics. Axial error signals are developed by a
position sensor located at the center of each station. The
axial servo loops in each of the three stations are independent
of each other. The four radial magnets in each station are also
driven by a set of electronics in response to a radial position
sensor located in the center of that station. But, the radial
servos are interconnected from one station to another so as
to prevent the servos fighting one another even in the presence
of rim radial growth.

4.1.1   Magnet Description

One of the unique features of the AMCD is the support magnet
design. The electromagnets are flux-biased by thin wafers of
samarium cobalt permanent magnet material placed in series in
the magnetic circuit. This has the advantage of (1) providing
a high force per unit current sensitivity at zero current, (2)
providing a linear relationship between force and current, and
(3) providing the static field required for zero power operation.

The support magnet geometry is seen in Figure 4-1. The permanent
magnet biasing is achieved by slanted wafers of samarium cobalt
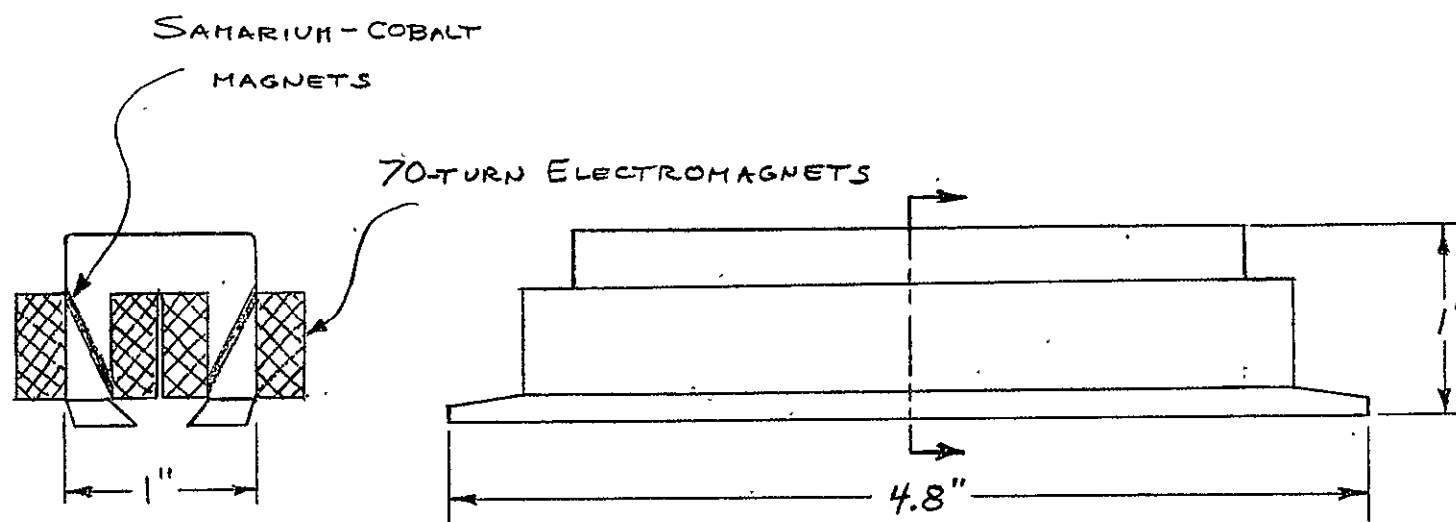in the legs. The wafers are as thin and wide as possible to

SAMARIUM-COBALT
MAGNETS

70-TURN ELECTROMAGNETS

1"

4.8"

1"

Figure 4-1 Support Magnet Geometry

F76-02

minimize their reluctance in the magnetic circuit. The volume of permanent magnet material is sufficient, however, to provide adequate flux-biasing and static lift. The reluctance of the permanent magnets is large but does not more than double the total reluctance since the air gap in this system is large. In many other magnet suspension systems, the gaps are small (about 0.1 mm) and this sort of series flux biasing would greatly increase the total reluctance in the circuit. Control power would thus be large and the systems would be impractical.

The effect of flux-biasing on the force versus current characteristics of the magnets is shown in Figure 4-2. With no biasing, current in either direction produces force of the same sign, with poor "gain" and low efficiency in the vicinity of zero current. Force is simply a function of the square of the current. With biasing, the slope of force versus current is greatly increased at zero current. In the AMCD, top and bottom magnets operate together in a push-pull type of operation. The coils are in series, hence both coils have zero current at the same time. The resultant force-current relationship is linear and has a slope double that of either magnet alone.

Figure 4-3 shows the "U" core of the magnet with the permanent magnets in place. Permanent magnet thickness is 1 mm (0.040 inches). Also shown in Figure 4-3 is a fully assembled magnet ready for potting. After potting, the units measure 4.3 cm x 10.7 cm x 2.5 cm (1.7 in x 4.2 in x .99 in) and weigh 500 grams (1.1 lbs.).

4.1.2   Position Sensors

The position sensors used in both the axial and radial suspension systems are "Multi-vit" sensors manufactured by Kaman Sciences
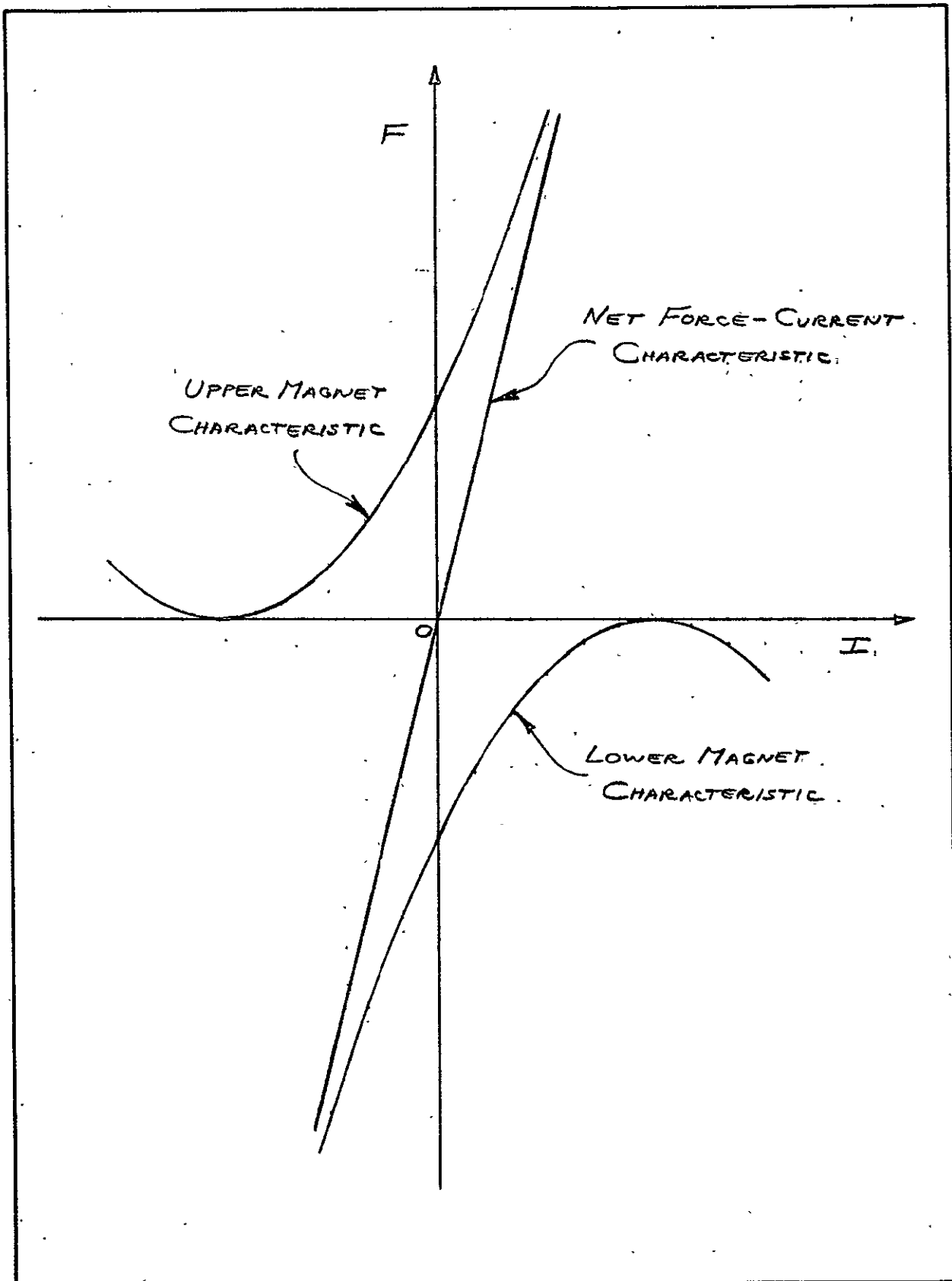
Figure 4-2 Flux-Biased Magnets in Push-Pull Operation
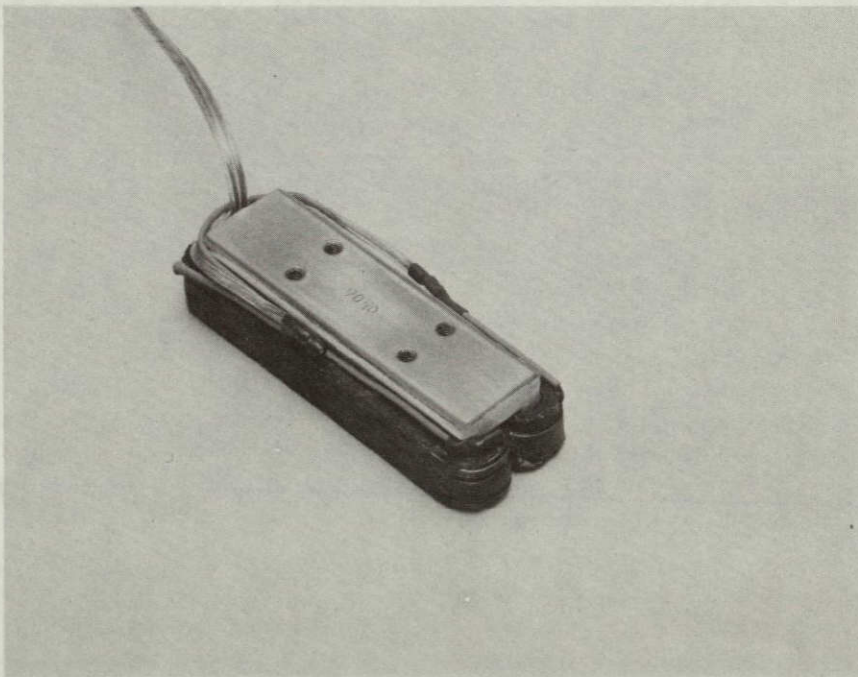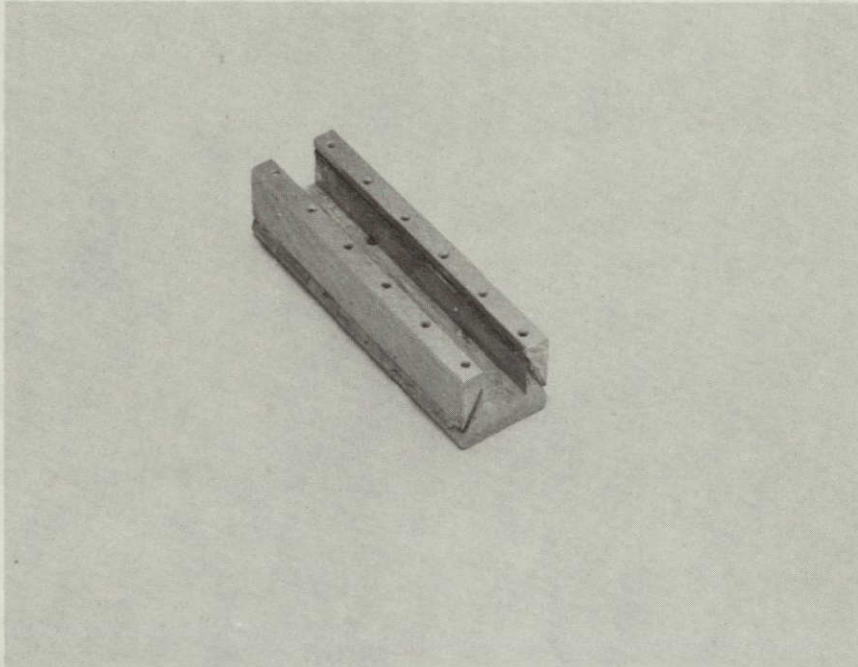
Figure 4-3   Support Magnet Construction

Corporation. These are conventionally called "eddy current" sensors although they are actually sensitive to anything that changes the inductance of the test coil in the probe. Hence, either eddy currents in a conductor or the permeability of a magnetic material can be sensed. In the AMCD, the sensors "look at" the ferrite bands and therefore are operating entirely in a non-eddy-current, magnetic permeability mode. Special calibration of the sensors was required in order to operate in this mode. Linear range of the AMCD sensors is 0.25 cm (0.1 inches) and scale factor was set at 4 volts/cm (10 volts/in.).

4.1.3   Control System

The axial suspension system uses three independent servo loops to control electromagnet currents. An electronic diagram of one of these loops is shown in Figure 4-4. The heart of the electronics is an Inland Controls MA-1 DC servo amplifier which is operated as a current driver to reduce the effects of electromagnet inductance. Equations of motion of this driver and an analysis of the voltage feedback used to damp high frequency roots are given in Appendix A. An analytical block diagram of the entire servo loop is shown in Figure 4-5. Equivalent points on the electronic and analytical diagrams are indicated by letters within hexagons.

The axial suspension system has two modes of operation, a "position" mode and a "virtually zero power" (VZP) mode. In the position mode, rim position error is used to command electromagnet current. The rim has high static and dynamic stiffness about any desired point in the gap. In the VZP mode, the rim position set point is modified by positive feedback of the integral of electromagnet current. The result is that the set point is moved until steady-state current is zero. The permanent magnets are
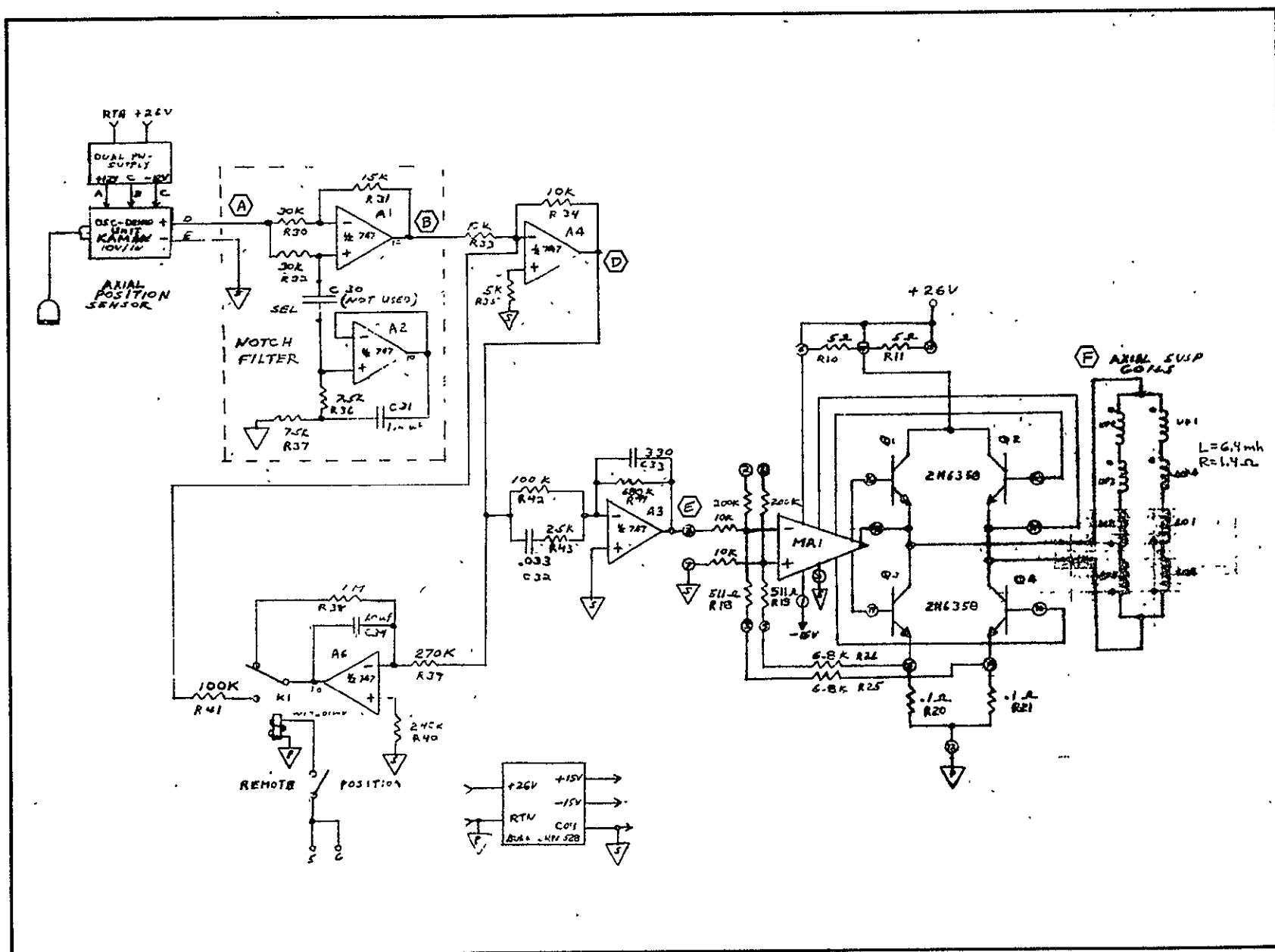
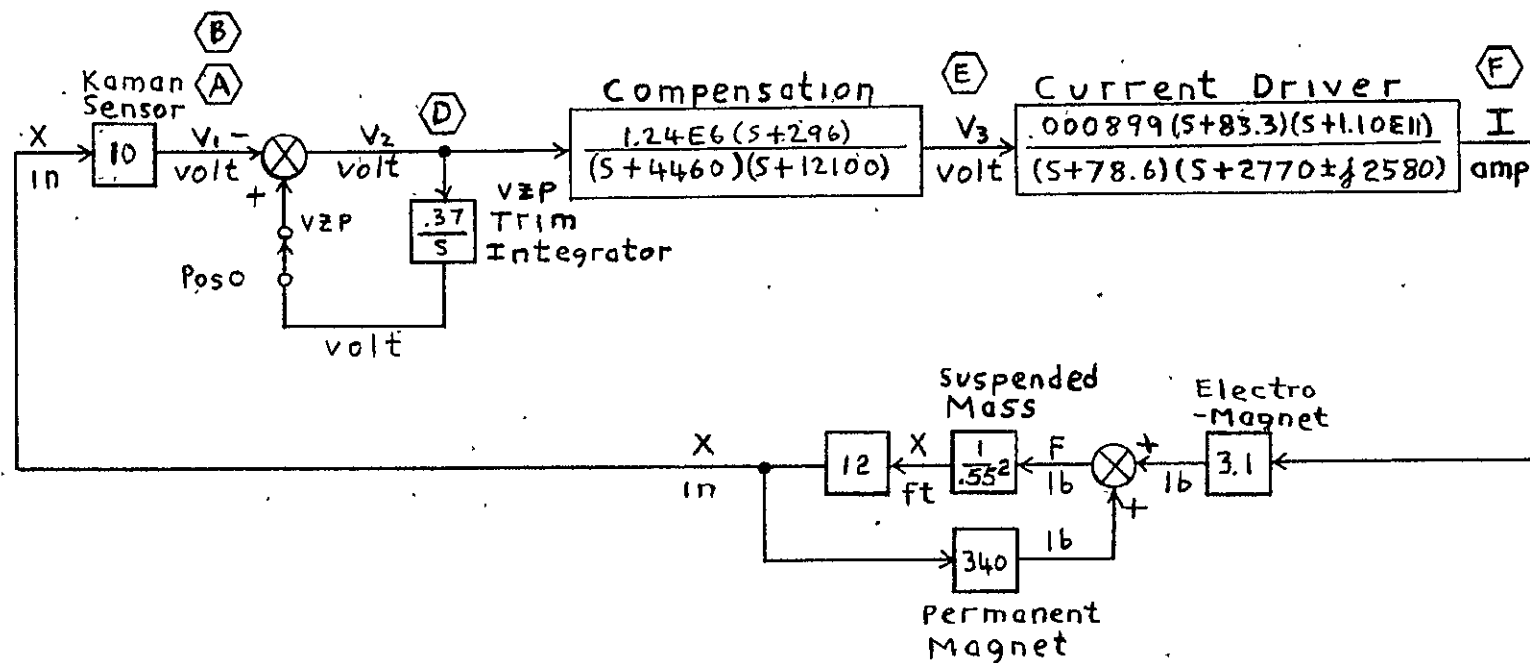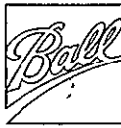Figure 4-4   Axial Suspension Electronics

F76-02

Figure 4-5   AMCD Axial Suspension Station

then providing all of the support of the rim. Dynamic stiffness
is nearly the same as in the position mode but static stiffness
is actual negative. If a downward force is applied to the rim
in the VZP mode, it initially moves downward but then slowly
rises to assume a new zero power position above the old equilibrium
position.

The electronic circuit diagram for a radial servo station is
shown in Figure 4-6 and the corresponding highly coupled analyti-
cal block diagram is shown in Figure 4-7. Again, equivalent
points on the two diagrams are indicated by letters in hexagons.
The large amount of coupling results from three servos control-
ling only two degrees of freedom.

Two modes of operation are available, a position mode and a WAHOO
mode. The position mode is similar to the axial position mode.
The WAHOO mode is a zero power mode that produces zero power
operation in the presence of both static loads and rim expansion.
This is accomplished by adjusting the position set point at each
station as a function of the integral of the sum of the electro-
magnet currents at the other two stations.

The name WAHOO is derived from the poker game WAHOO. This game
is played in a manner such that each player knows what every
other player holds but does not know what he himself holds.
Inspection of the WAHOO trim loops of Figure 4-7 reveals that
for VZP trim purposes, each servo only looks at what the other
two are doing. This innovation was developed by BBRC to meet
the unique requirements of the AMCD.

The derivation of the WAHOO concept is given in Appendix B.
There, it is shown that only the WAHOO concept produces zero
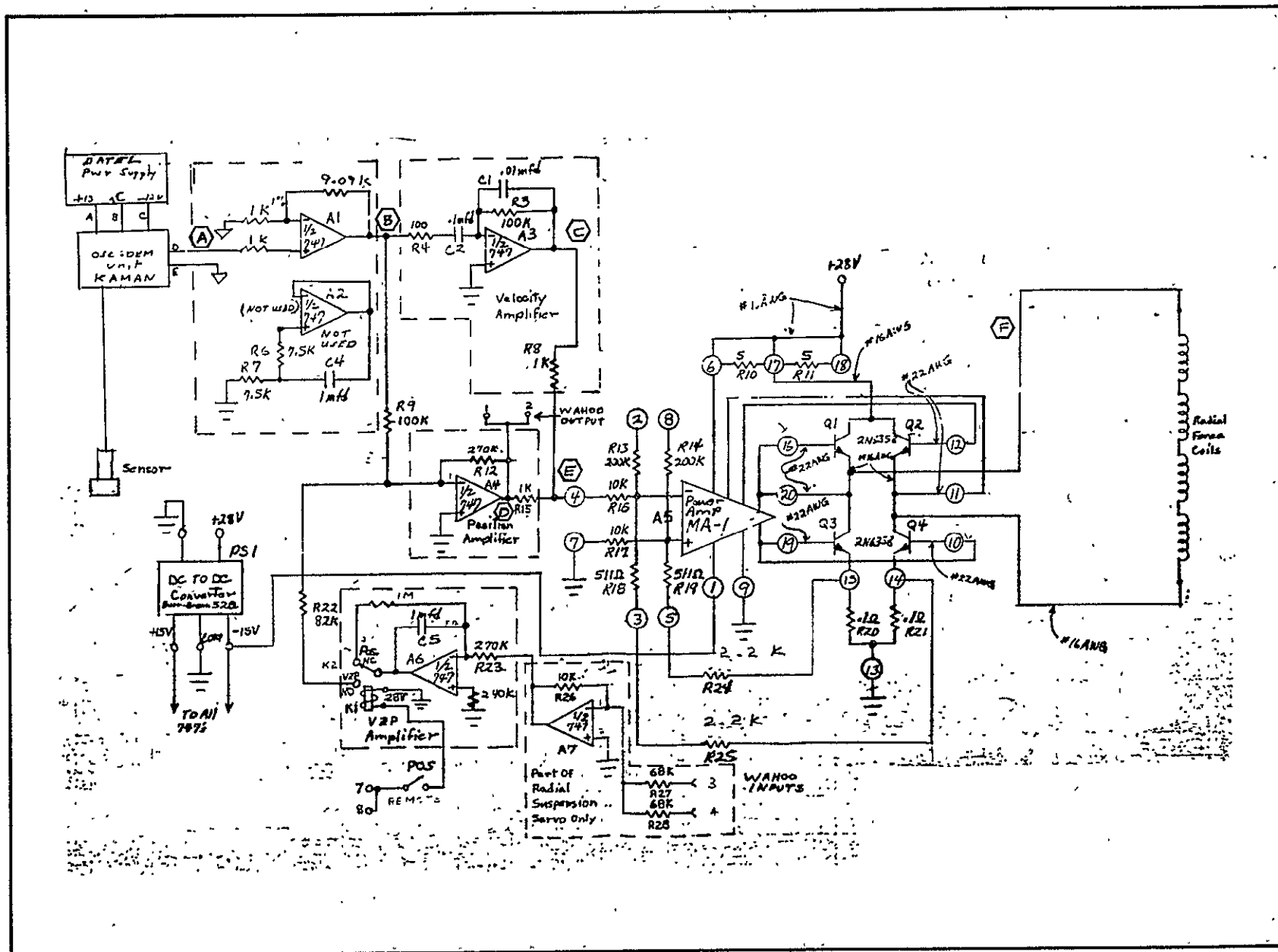power operation for both rim expansion and force disturbances.
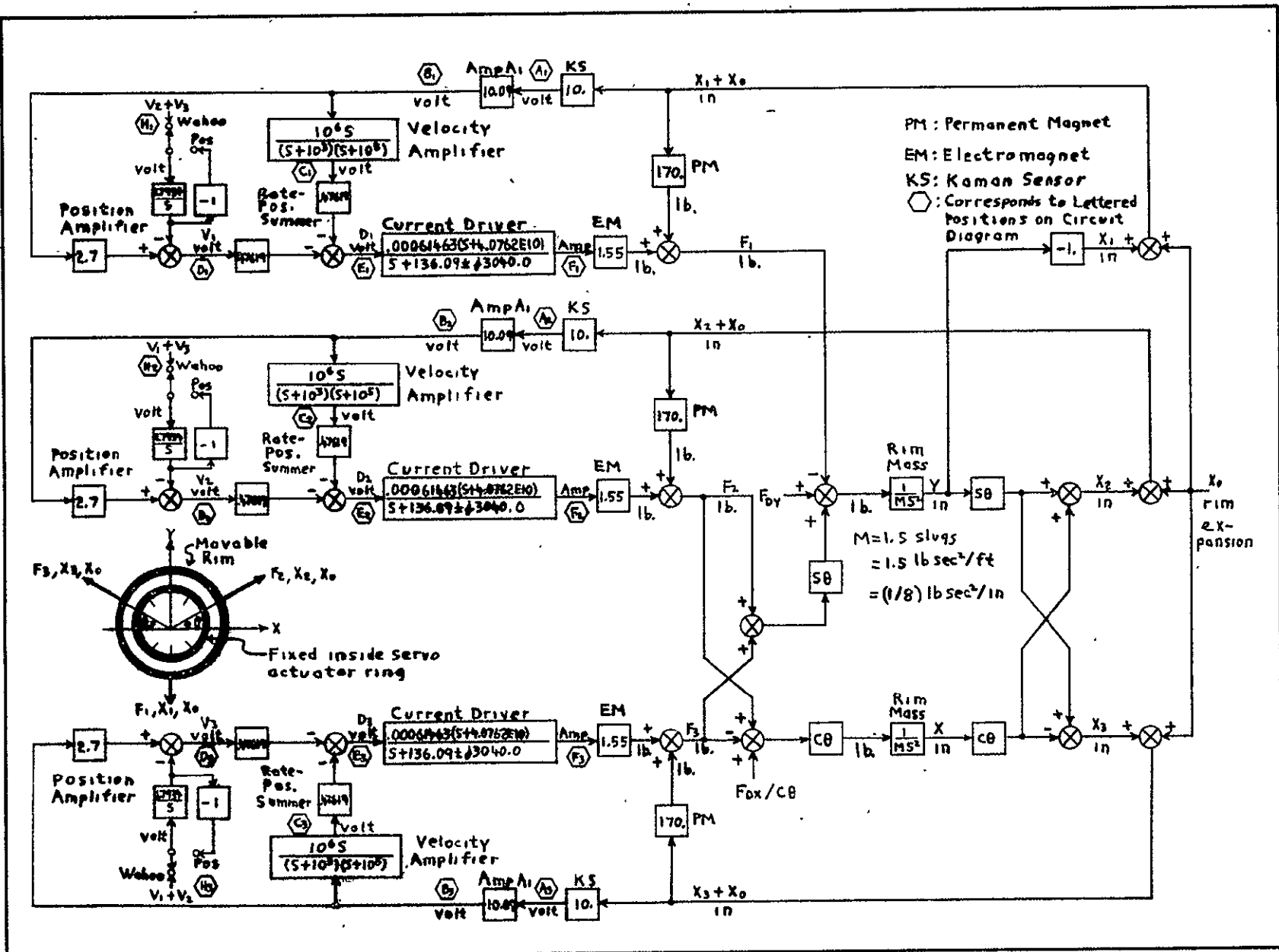
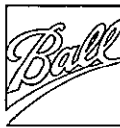Figure 4-6 Radial Suspension Electronics
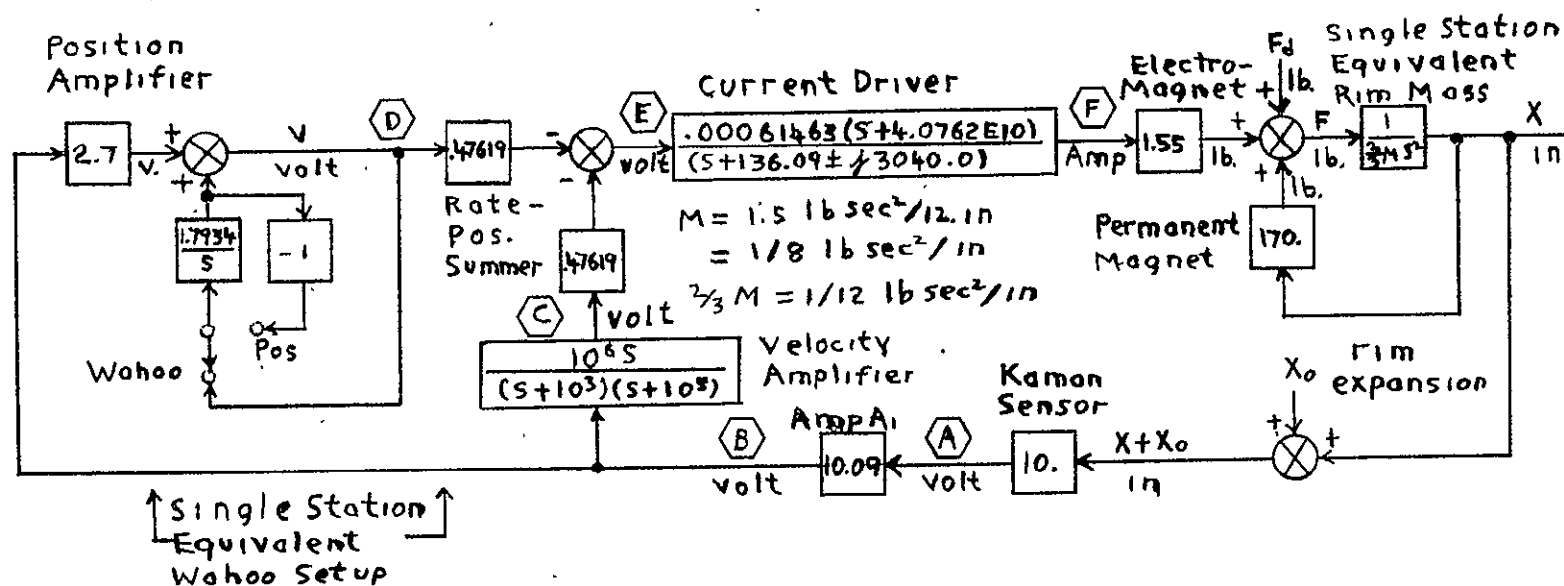
Figure 4-7   AMCD Radial Servos

Appendix B also shows that for single station design purposes, a single station can be represented as shown in Figure 4-8. Two points of interest are immediately evident. The equivalent mass for a single station representation is 2/3 the total rim mass. The WAHOO concept which involves <u>negative</u> feedback to each station from the sum of the other two stations resolves to a <u>positive</u> feedback in the single station representation exactly like VZP in the axial mode. This representation can be used for designing the system characteristic root locations. If the characteristic roots from the single station representation are given by Δ and the WAHOO gain is K_c, it is shown in Appendix B that the three station highly coupled set of characteristic roots are given by $(S + 2K_c)\Delta^2$.

4.2   Performance

4.2.1   Static Performance

At each suspension station, the rim will seek an axial equilibrium position based on the applied load and the control system mode ("position" or "VZP"). These equilibrium positions can be presented in one plot as shown in Figure 4-9. The VZP line is a zero current line and has a slope that indicates static instability, however as shown in the next section, the system can operate in a stable manner along this line. The most usual operating position mode point is about 0.01 cm (.025 inches) above the center of the gap. At this point, the slope P of the VZP line is about 595 newtons/cm (340 lb/in).

In the position mode, an operating line exists for each set point of the position sensor. A family of these is shown in Figure 4-9. The lines are finite in length because of the limited current drive capability of the electronics. The slopes of the lines are approximately 2600 newtons/cm (1500 lb/in).

Position
Amplifier

2.7

V volt (D)

$.47619$

Rate-
Pos.
Summer

(E) Current Driver

$$\frac{.00061463(S+4.0762E101)}{(S+136.09 \pm j3040.0)}$$ Amp

$M = 1.5 \text{ lb sec}^2/12.\text{in}$
$= 1/8 \text{ lb sec}^2/\text{in}$
$2/3 M = 1/12 \text{ lb sec}^2/\text{in}$

Electro-
Magnet

1.55 lb

Permanent
Magnet

$170.$

F_d lb

Single Station
Equivalent
Rim Mass

$\frac{1}{\frac{2}{3}MS^2}$

X in

$1.7734 / S$ -1

Wahoo   Pos

$.47619$

(C) volt

$$\frac{10^6 S}{(S+10^3)(S+10^5)}$$ Velocity
Amplifier

X_0 rim
expansion

(B) Amp A_1 volt 10.09 (A) volt $10.$ $X+X_0$ in   Kaman Sensor

Single Station
Equivalent
Wahoo Set up

⬡ : Corresponds to lettered positions on circuit diagram.

● Single station equivalent mass is 2/3 total mass.

● Note that single station equivalent wahoo is
modelled as a positive feedback self loop. We
would therefore expect it to act like VZP in
the Axial Servos. It does, and furthermore it
is not only VZP to disturbance forces, but
also to rim expansion.

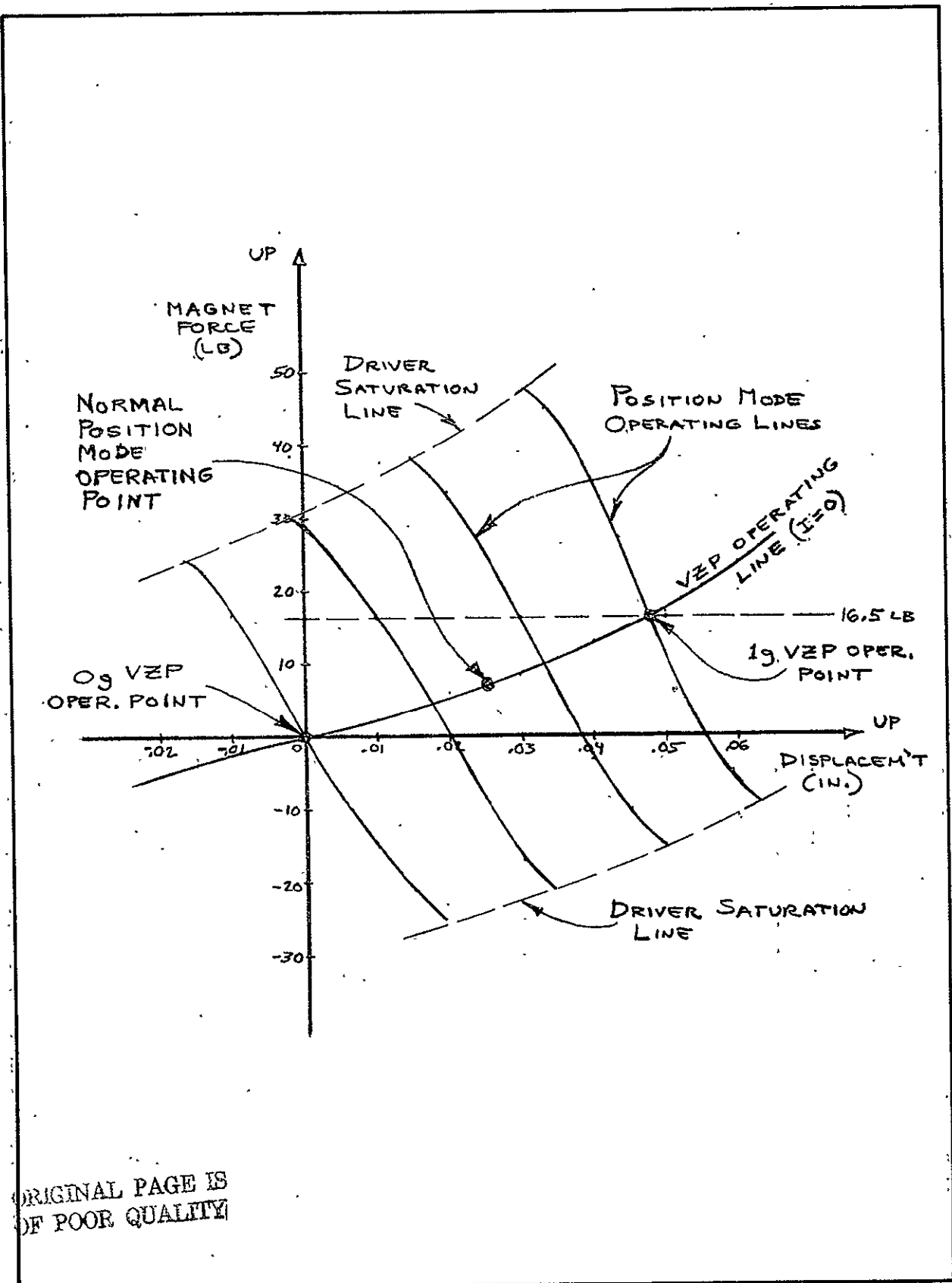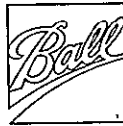Figure 4-8   Equivalent Single Radial Servo Station

Figure 4-9   Typical Static Suspension System Performance

The force sensitivity F of each station is about 13.8 newtons/ ampere (3.1 lb/amp.). Hence, the force produced by a station is given by (in English units):

$$F = 340X + 3.1 \cdot I.$$

4.2.2 Dynamic Performance

The analytical block diagram for an axial suspension station is shown in Figure 4-5. For the position mode, the root locus and Bode plots are shown respectively in Figures 4-10 and 4-11. The root locus plot shows that the dominant pole pair has an undamped natural frequency ω_N (which we define as bandwidth) of 171 rad/sec (27.2 hertz) and a damping ratio ζ of .28. The Bode plot shows that the gain crossover frequency ω_c (which some define as bandwidth) is 182.7 rad/sec (29.0 hertz) and that the system phase margin is 23.2°. Both plots show that the lower gain margin is .22 (-13.1 db) and that the upper gain margin is 20.1 (26.1 db).

For the VZP mode, the root locus and Bode plots are shown respectively in Figures 4-12 and 4-13. The root locus plot shows that the dominant pole pair has the same undamped natural frequency and damping ratio as the position mode, that is, ω_N = 171 rad/sec, ζ = .28. The Bode plot shows that two gain crossover frequencies exist, one at .0838 rad/sec (.013 hertz) and one at 182.3 rad/sec (29.03 hertz). The phase margin at the lower crossover frequency is -77.2° and that at the upper crossover frequency is 23.0°. Both plots show that the lower gain margin is .226 (-12.9 db) and that the upper gain margin is 20.11 (26.1 db).

The response due to the step application of a one pound weight is shown for the position mode in Figure 4-14 and for the VZP
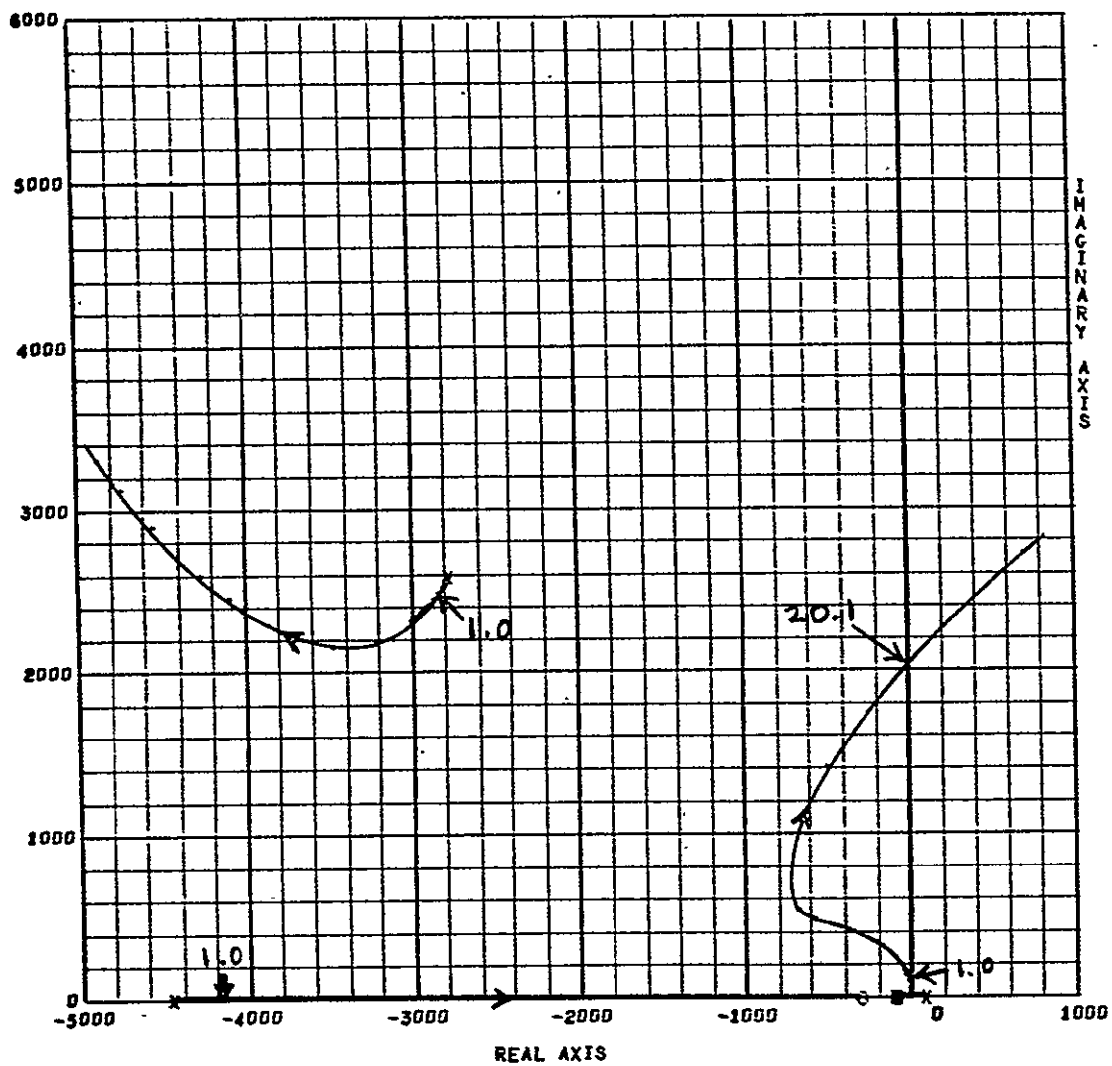
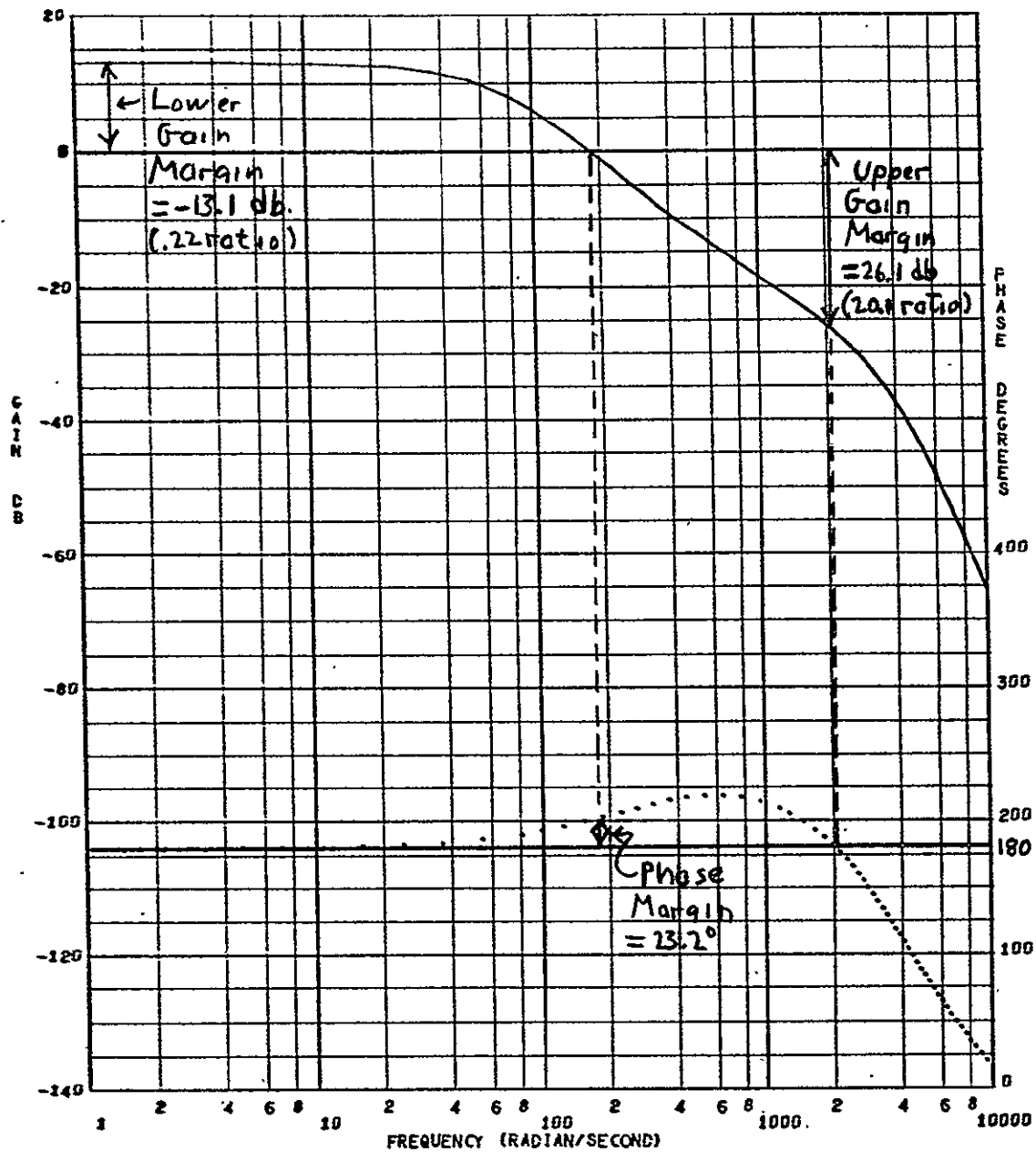Figure 4-10(A)   Root Locus Plot - Nonideal Current Driver With
Voltage Feedback

Figure 4-10 (B) Root Locus Plot - Nonideal Current Driver With
Voltage Feedback

Figure 4-11   Bode Plot - Nonideal Current Driver With
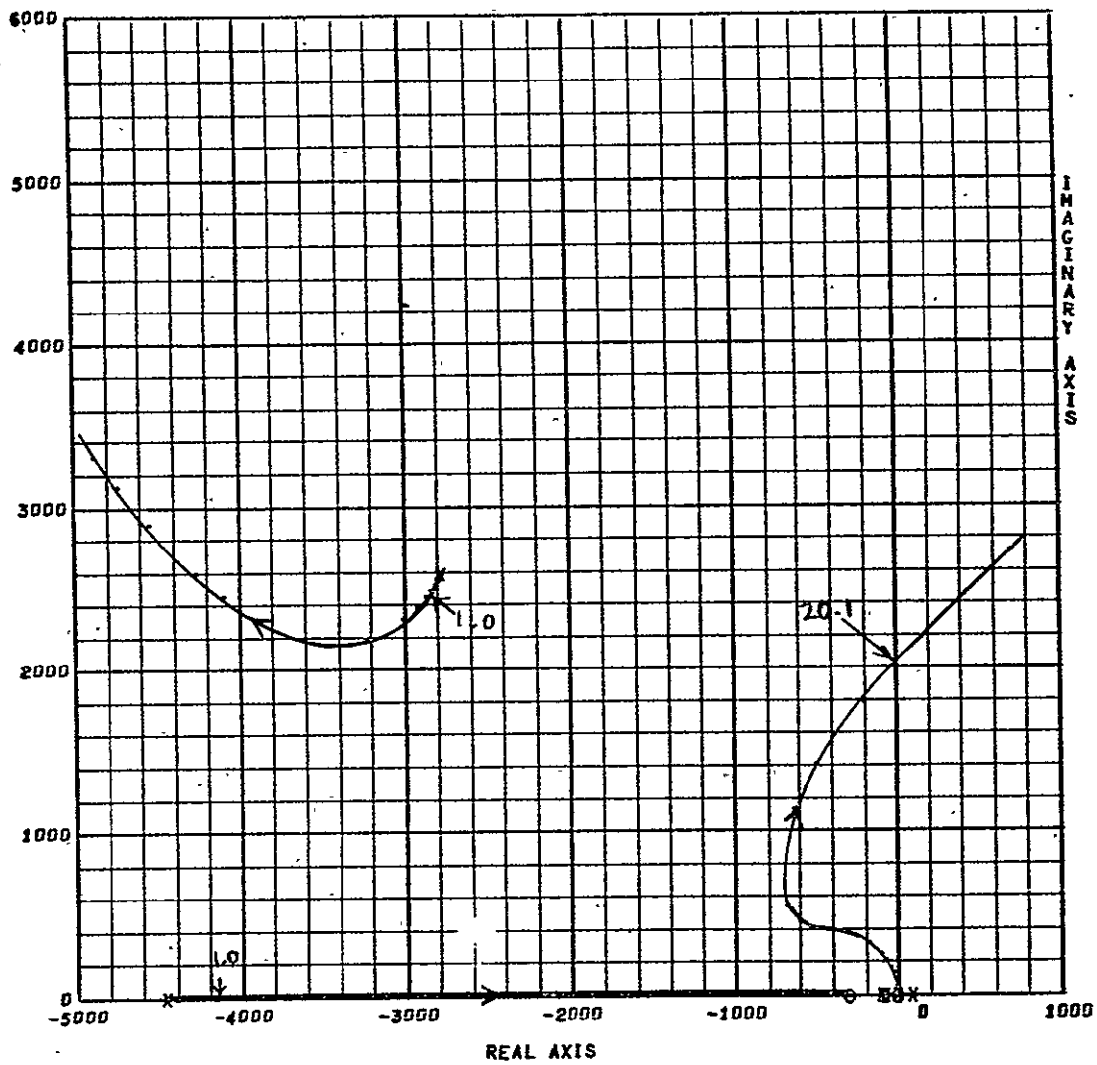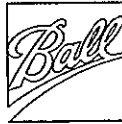   Voltage Feedback

4-18

Figure 4-12(A). Root Locus Plot - Nonideal Current Driver With
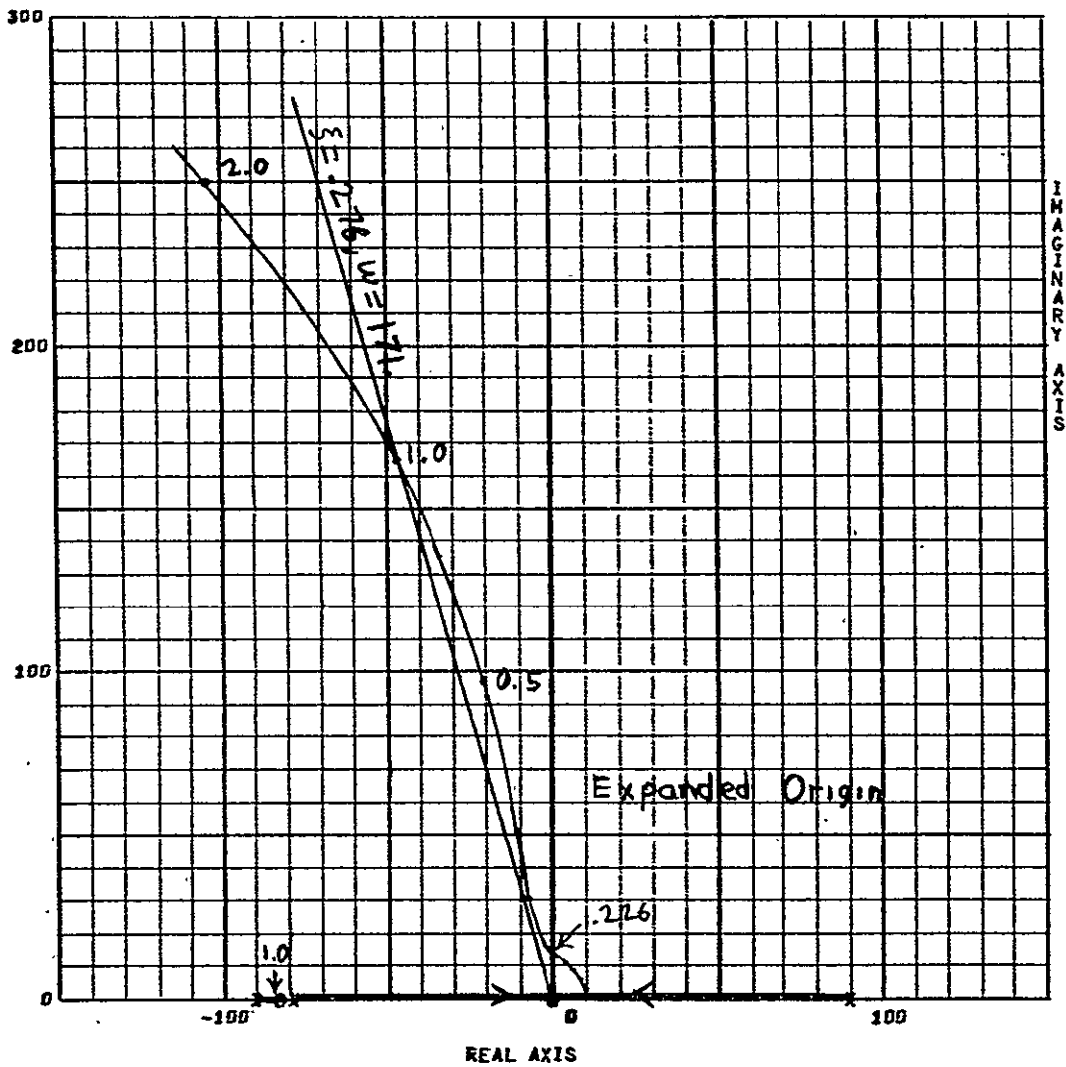Voltage Feedback

Figure 4-12(B)   Root Locus Plot - Nonideal Current Driver
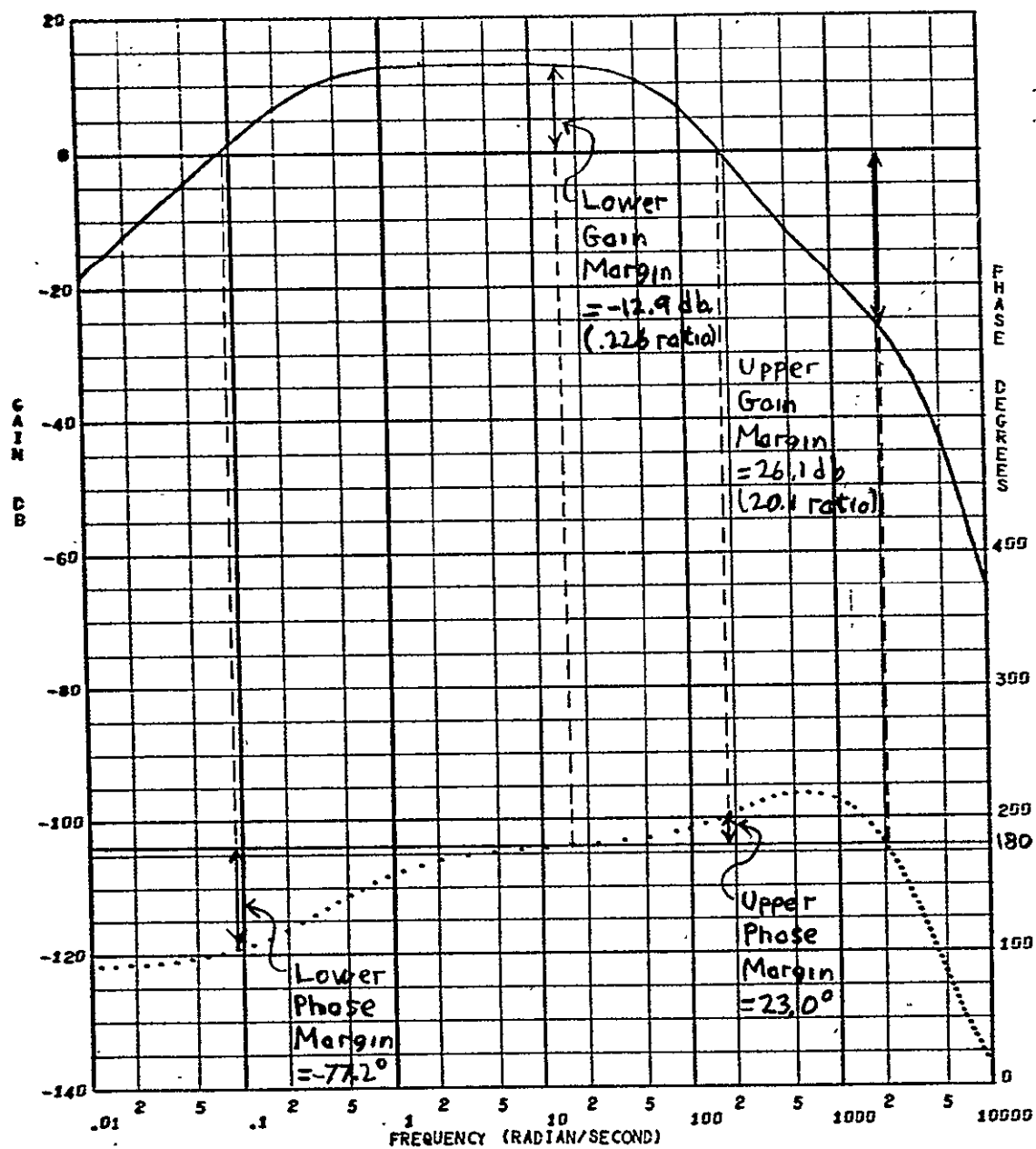With Voltage Feedback

Figure 4-13   Bode Plot - Nonideal Current Driver With
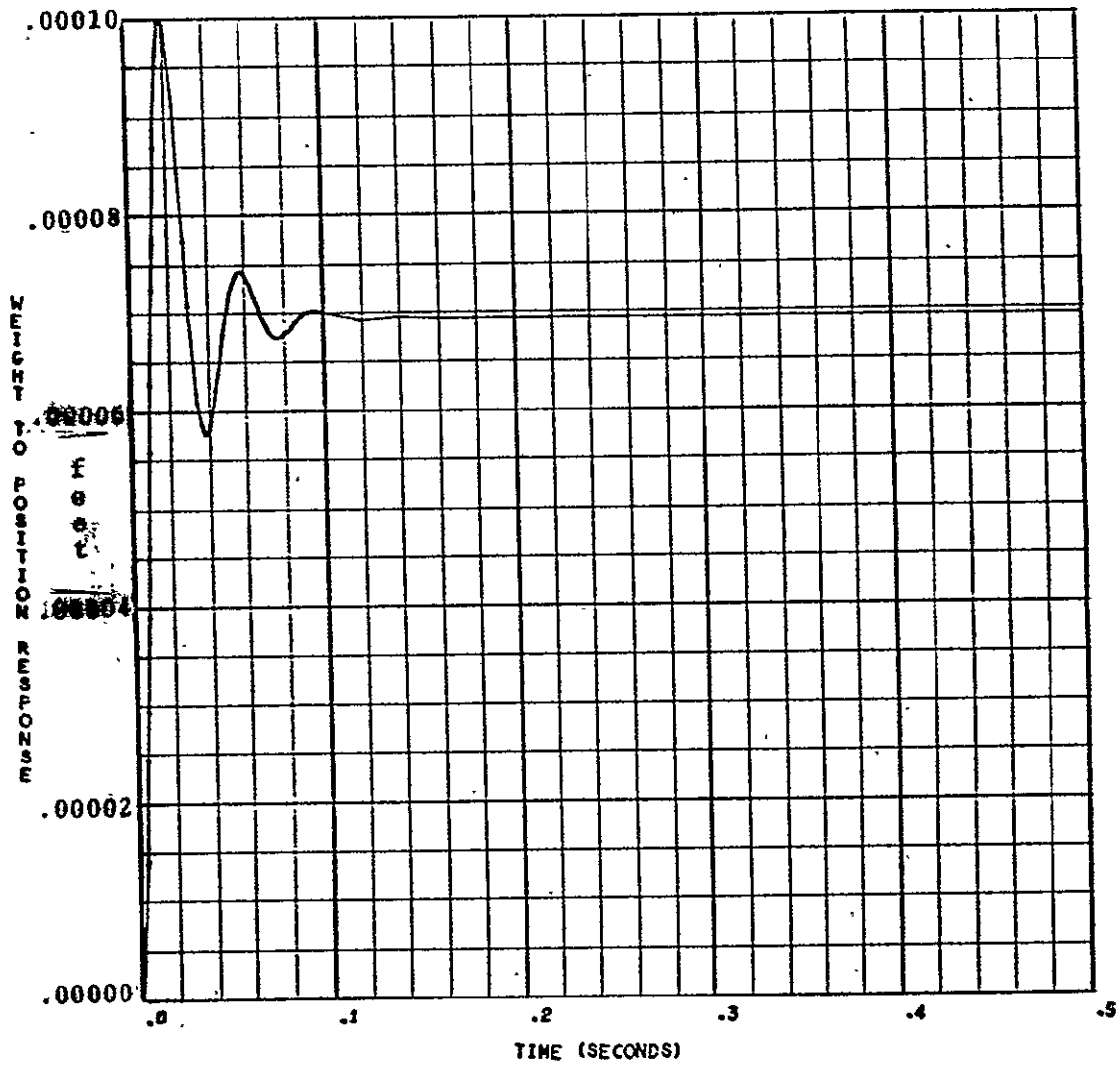Voltage Feedback

Figure 4-14   Nonideal Current Driver With Voltage Feedback

mode in Figure 4-15. The response for the position mode settles out at 6.941E-5 feet (.002 cm). This yields a position mode stiffness of

$$\text{Stiffness} = \frac{1 \text{ lb.}}{6.941E-5 \text{ ft.}} \times \frac{\text{feet}}{12 \text{ in.}} = 1200.6 \frac{\text{lb.}}{\text{in.}} \ (2102 \frac{N}{cm})$$

The response for the VZP mode settles out at -2.451E-4 feet. This yields a VZP mode stiffness of

$$\text{Stiffness} = \frac{1 \text{ lb.}}{-2.451E-4 \text{ ft.}} \times \frac{\text{feet}}{12 \text{ in.}} = -340.0 \frac{\text{lb.}}{\text{in.}} \ (-595 \frac{N}{cm})$$

Note that the stiffness in the VZP mode is just that of the permanent magnet and that the movement in this mode is toward the applied force. That is, if a weight is placed on the rim in the VZP mode, the rim will move up.

Further insight into the system can be found by examining Appendix C. When using current drivers, the usual tendency is to ignore the high frequency dynamics and simply say that the output current is the input voltage times a constant. This can be very misleading in the case of AMCD. In Appendix C are shown root locus plots using both an ideal current driver and a non-ideal current driver without voltage feedback. It shows that voltage feedback is necessary for the axial suspension. Also shown in Appendix C are Nyquist plots and phase-gain root locus plots of the nominal axial system, that is, the system using current drivers with voltage feedback. The esoteric phase-gain root locus plot shows on one plot the sensitivity of the system roots to change in both gain and phase. For example, it shows what would happen if an additional 30° of phase lag were added to the system from some unknown source.
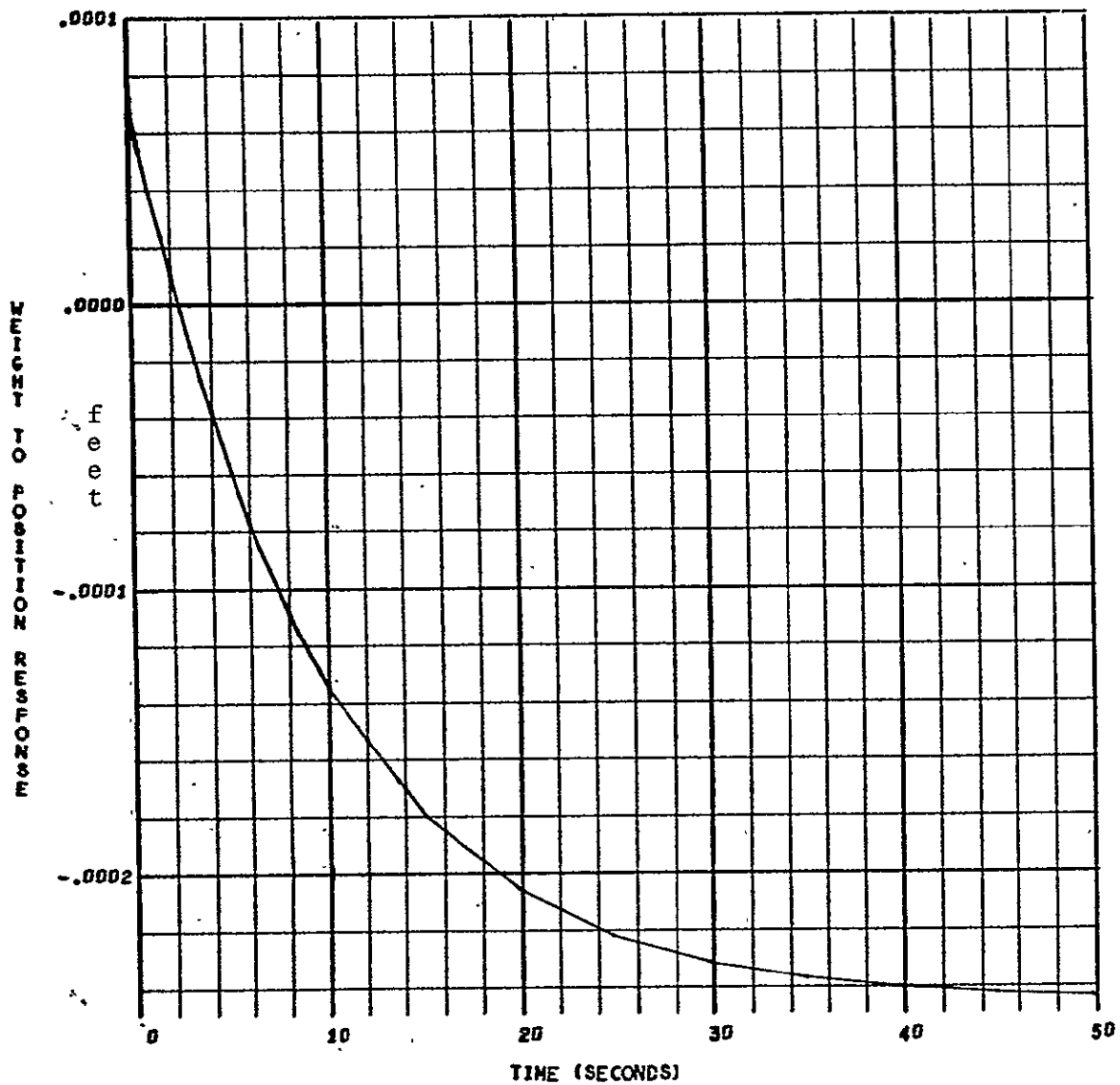
Figure 4-15. Nonideal Current Driver With Voltage Feedback

The equivalent single station radial analytic block diagram is
shown in Figure 4-8. It is very similar to an axial station.
The root locus and Bode plots for the position mode are shown
respectively in Figures 4-16 and 4-17. The root locus plot shows
that the dominant pole pair has an undamped natural frequency
(bandwidth) ω_N of 65.3 rad/sec (10.4 hertz) and damping ratio ζ
of .18. The Bode plot shows that the gain crossover frequency
is 66.6 rad/sec (10.6 hertz) and that the phase margin is 13.5°.
Both plots show that the lower gain margin is .329 (-9.65 db)
and that the upper gain margin is 70.54 (36.97 db).

The root locus and Bode plots for the WAHOO mode is shown in
Figures 4-18 and 4-19. The root locus shows that the dominant
pole pair has an undamped natural frequency of 67.4 rad/sec
(10.7 hertz) and damping ratio of .16. The Bode plot shows that
the upper gain crossover frequency is 69.1 rad/sec (11.0 hertz).
At this frequency, the phase margin is 12.6°. Not shown is the
fact that the system also has a lower gain crossover frequency
of .594 rad/sec (.095 hertz). At this frequency the phase mar-
gin is -71.5°. Both plots show that the lower gain margin is
.389 (-8.21 db) and that the upper gain margin is 67.01 (36.5 db).

The large upper gain margins for both the position and the VZP
modes indicate that current driver voltage feedback is not needed.

Considerable rim bending instabilities were encountered during
the design. Early in the development, the axial system was
designed to be overdamped. This caused a bending mode to be
driven unstable. The compensation was adjusted experimentally
until the bending became stable. Unfortunately, this reduced
the lead in the system resulting in the present underdamped sys-
tem. It is believed that bending will present no problem at
high spin rates because of the effective stiffening of the rim

Figure 4-16   AMCD Radial Suspension Equivalent Single Station
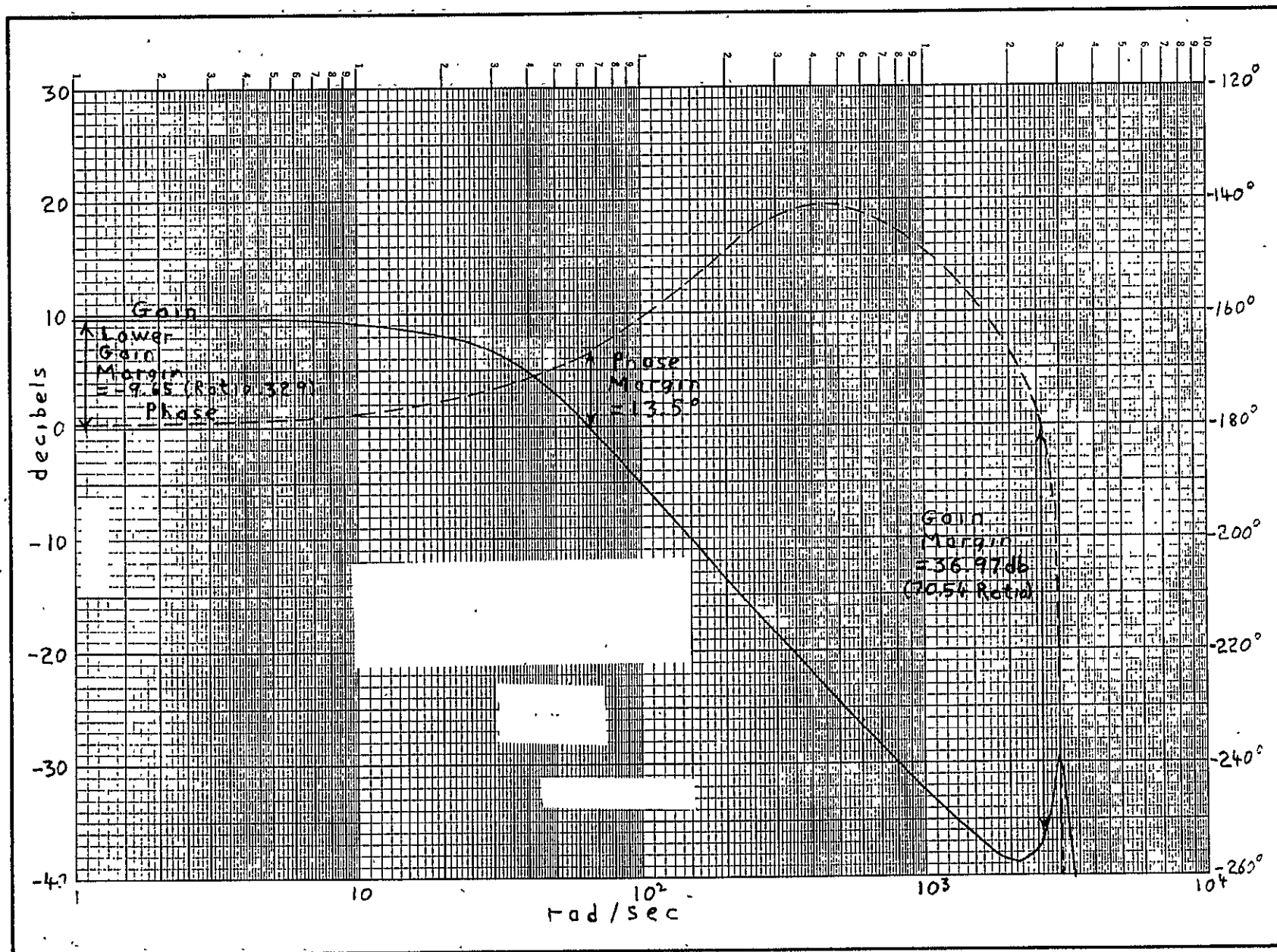Position Mode

Figure 4-17   AMCD Radial Suspension Equivalent Single Station
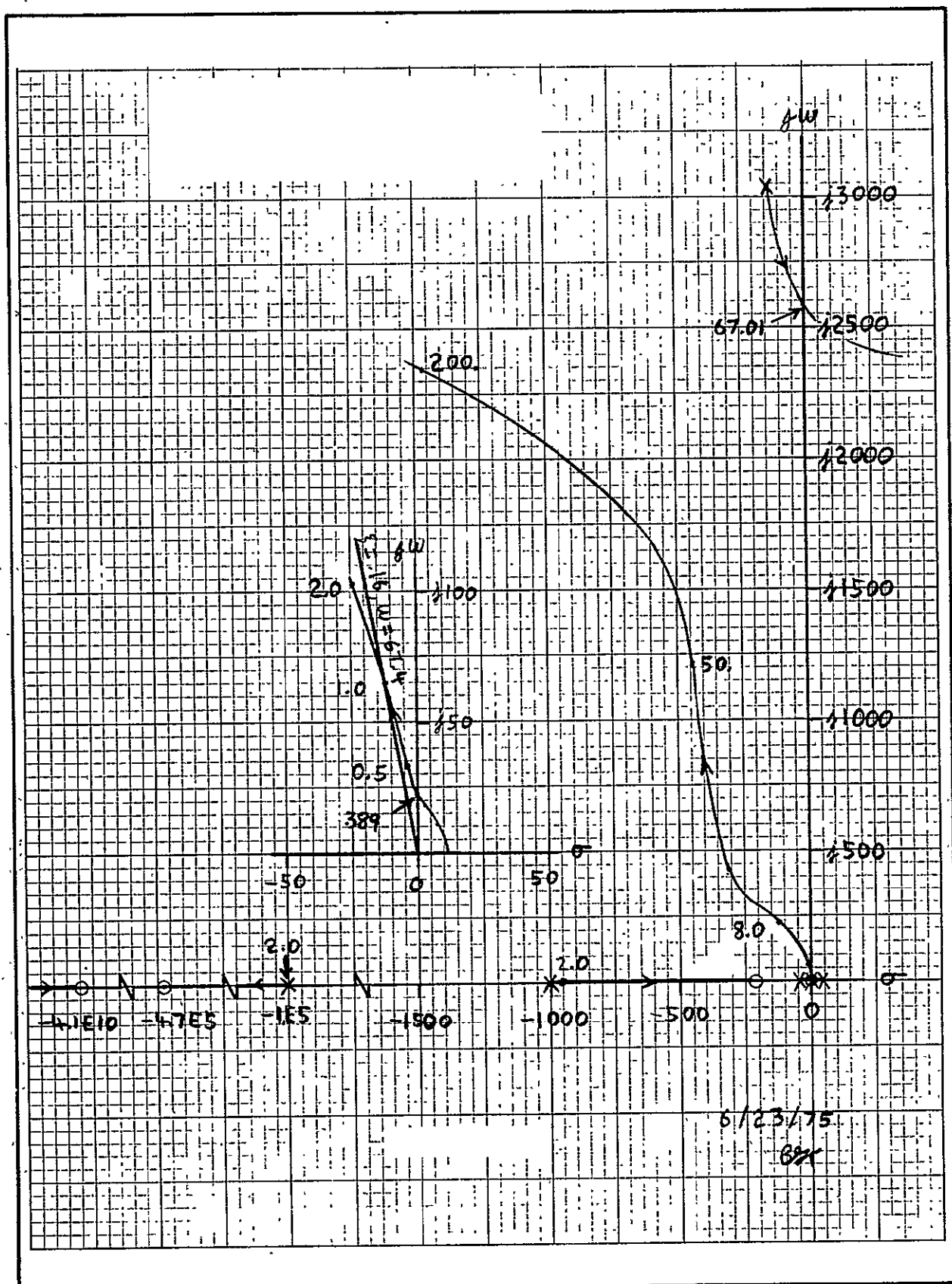   o   Position Mode

Figure 4-18   AMCD Radial Suspension Equivalent Single Station
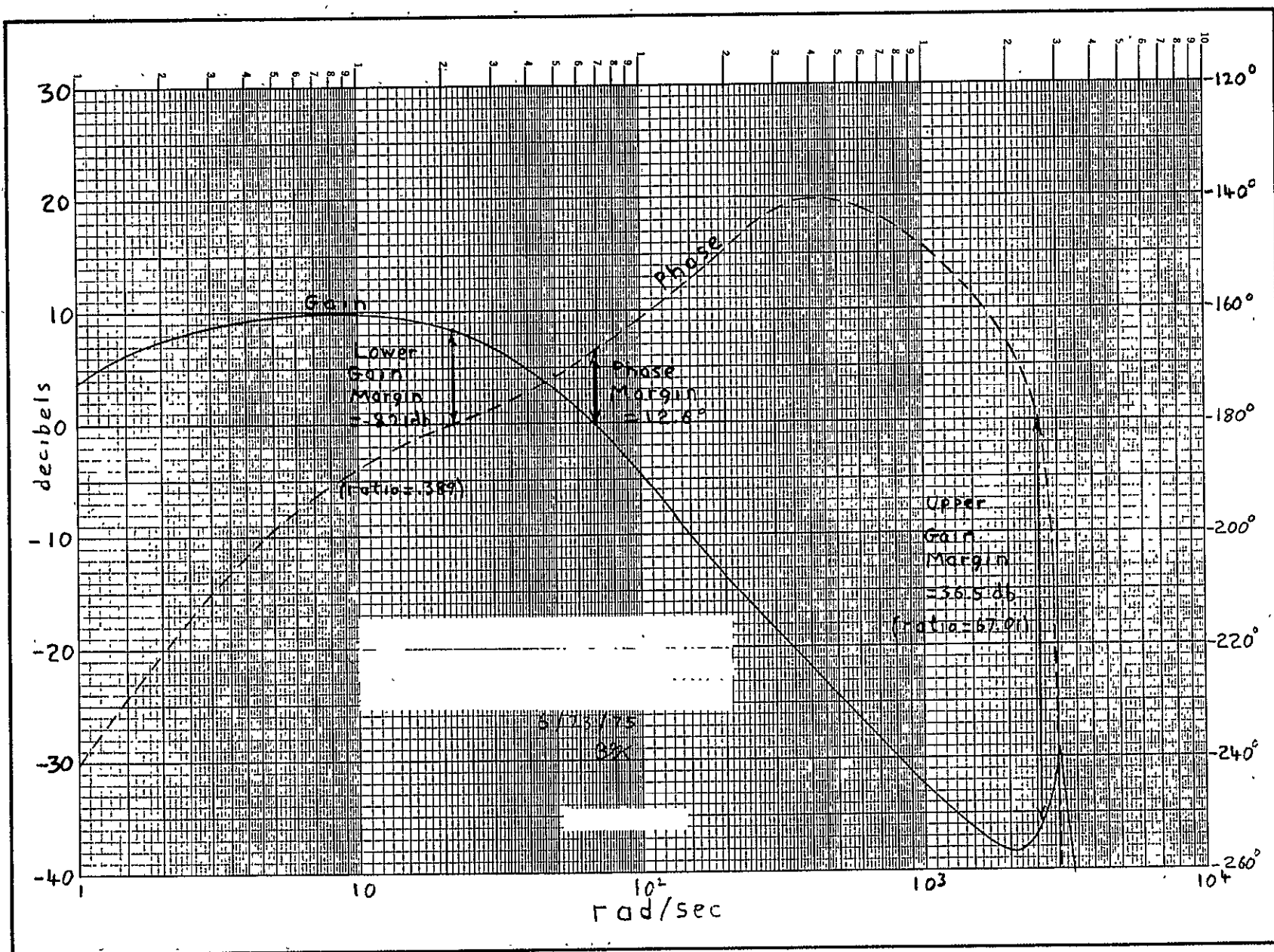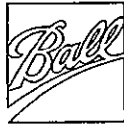o   Wahoo Mode

Figure 4-19   AMCD Radial Suspension Equivalent Single Station
    o Wahoo Mode

and the averaging effect on modal pick-up caused by the bending modes moving rapidly past each position sensor.

As the rim is spun up, the three axial stations become more and more coupled by nutational effects. The result of the coupling is to reduce the dominant roots damping ratios more and more to the point the system could go unstable if the rim is spun fast enough. It is believed that this tendency could be greatly reduced or possibly eliminated by the proper combination of cross feeds from one axial suspension station to the others.

5.0 DRIVE SYSTEM

5.1 System Description

The AMCD drive motor can be thought of as a large permanent magnet, brushless, d.c. torque motor. Samarium cobalt magnets are bonded into the rim at regular intervals. The two phase armature is segmented with a winding set at each of the three suspension stations. Commutation is controlled by Hall effect sensors mounted near the rim which sense position of the samarium cobalt motor magnets.

5.2 Magnet Selection

Alnico was considered along with samarium cobalt for the permanent magnets. The large air gap and segmented winding structure mean the magnets will become nearly air stabilized. The rim was designed with a small outer lip to hold the magnets. This was done to isolate the drive from the suspension as much as possible without adding more mass and complexity to the rim than necessary. This small lip implies a short magnet. Samarium cobalt has high strength for short lengths and does not pay a penalty for air stabilization. In fact it is very difficult to demagnetize this material.

Samarium cobalt magnets 1.4 cm (.55 inches) diameter by .64 cm (.25 inches) length were selected and bonded into the rim with polarities alternated.
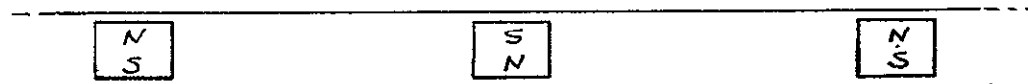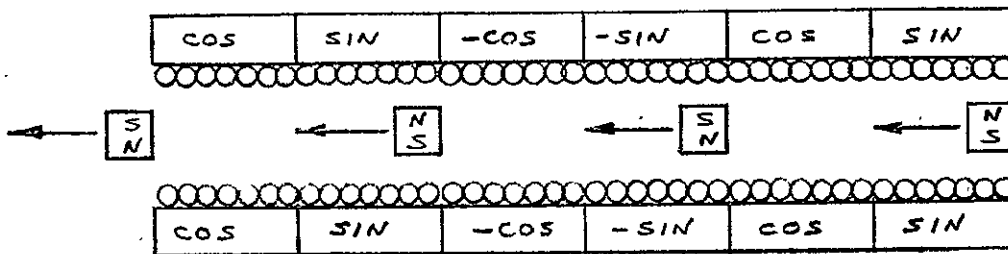

The rim contains a total of 72 magnets spaced 7.3 cm (2.88 inches) apart.

5.3   Core and Winding Design

Each armature segment consists of a pair of bar-shaped winding
assemblies, one above and one below the rim.

The windings are wound toroidally around the cores in a single
layer. The figure above shows only the cross-section of con-
ductors in the air gap as the conductors passing around the other
side of the core add nothing to torque and serve only a connect-
ing purpose. The bar-shaped cores are easy to wind and result
in a compact structure. The single layer of #18 conductors adds
very little to the overall air gap. This effective electro-
magnet design was suggested by P. A. Studer of Goddard Space
Flight Center.

Ferrite material was chosen for the core to reduce losses. Fer-
rite also is easily machined into the required irregular shapes.

The windings are grouped into two phases, SINE and COSINE, each
of which acts upon three magnets at each motor segment. In opera-
tion, current in one phase is acting on the magnets while current
in the other phase is reversing in preparation for a magnet of
opposite polarity.
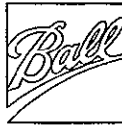
5.4   Motor Commutation

Hall sensors act as commutation devices for the motor. They sense
the position of the permanent magnets in the rim and cause the
drive coil currents to be switched according to magnet position.
The sensors are mounted in pairs, one above the rim and one below,
for each winding phase. Outputs from each pair are summed so that
the switching position is not affected if the rim moves up or down
within the air gap. The SIN pair controls current on the SIN
windings of all three motor segments and likewise, the COS pair
of Hall sensors controls all COS windings.

5.5   Motor Control Electronics

A block diagram of the motor control electronics is shown in Figure
5-1. For each phase, the Hall sensor outputs are summed and
amplified to drive threshold detectors. These detectors sense mag-
net position and polarity. The phase control logic determines the
timing and polarity of the motor coil drivers. Interconnections
between the two phase control logic blocks provide positive direc-
tion and start-up information.

Each of the six coil drivers controls a phase at one of the motor
segments. Associated with each driver is a coil current sensor
which monitors the current in that winding. All six of these
current sensors receive a common reference from the speed control
potentiometer. When current in that particular winding reaches
the reference level, the driver turns off until the current de-
creases. This prevents the current from reaching destructive
levels at low speeds and acts as a speed control at high rim
speeds.

Since the coil drivers are either full on or off, a very efficient
drive is achieved. At low rim speeds the drivers operate as a
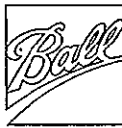
conventional PWM (pulse width modulated) amplifier. A quite
faithful square wave current of controlled amplitude is fed to
the coils. At high speeds, high acceleration (or deceleration)
is possible with the drivers full on for the period between mag-
nets with current rise and fall limited by the inductance of the
coils.

5.6   Torque Calculations

The equation for the force between a magnetic field and a current
carrying conductor is:

$$F = BLI$$

where

> F = Force in Newtons .
> B = Flux Density in Teslas (Webers/Meter^2)
> L = Conductor Length in Meters
> I = Current in Amps

If the magnetic field is created by a permanent magnet the force
can be considered to act on the magnet if the conductor is held
stationary which is the case with the AMCD motor.

To arrive at design force, each of the factors B, L, and I must
be evaluated.

A force calculation will be made for one magnet face interacting
with a coil. This can be then doubled to account for both ends of
the magnet, next tripled to take into account the three magnets
in one motor segment, and tripled again to realize the total force
for the three motor segments. Then using the radius of the rim,
we can calculate developed torque.

Flux Density Calculation (B)

The large air gap makes it difficult to estimate how much of the magnet flux will couple through the winding core and how much will be lost to leakage. A measurement of coupling flux was made using a pair of soft iron bars similar to the ferrite cores.
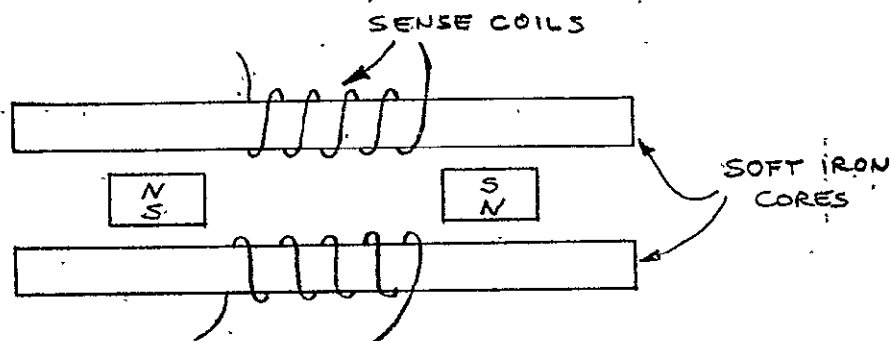
The flux measured was 0.375×10^{-4} Webers with magnets of average strength.

This flux that couples through the ferrite core must be converted to flux density (B) in the air gap where it interacts with the coil windings. There are two practical choices for doing this. We can assume all the flux goes straight up from the surface of the magnet and reacts with only those turns above the magnet or we can assume the flux spreads out evenly over the winding area and reacts with all the turns equally. Of course, the truth lies somewhere in between but the second approach gives an adequate approximation.

The winding area in the air gap for one magnet coil phase is 1.9×3.6 cm or 6.8 cm^2.

Flux density then is

$$B = \frac{\phi m}{A} = \frac{0.375 \times 10^{-4} \text{ Webers}}{6.8 \times 10^{-4} \text{ m}^2} = 0.055 \text{ Web/M}^2.$$

Conductor Length Calculation (L)

In the winding phase area there are 28 turns with an effective length of 1.9 cm each.

Total effective length is then

$$L = 1.9 \times 28 = 53.2 \text{ cm} = 0.532 \text{ M.}$$

Current (I)

The electronics are designed so that the coil drivers and wiring can handle 4 amperes. Also, the inductance of the coils was examined to be sure that currents of this magnitude can be reversed at maximum rim speed frequencies with a 60 volt power supply. Force (and torque) will then be calculated for the design maximum of 4 amps.

Force

We can now calculate force from the equation

$$F = BLI$$
$$= 0.055 \times 0.532 \times 4 = 0.117 \text{ Newtons.}$$

Recall that this is the force for a single magnet surface interface. For the total motor this is multiplied by 18.

$$\text{Total Force} = 0.117 \times 18 = 1.76 \text{ Newtons.}$$

This times the magnet radius (0.838 meters) gives total torque.

Total Torque = 1.76 x 0.838 = 1.76 Newton-Meters.
(1.3 lb-ft)

A small (1/4 diameter) test wheel was built to check the above torque calculations. Acceleration measurements were made and from the known wheel inertia, torque was determined. Correlation within 10% of the calculated torque was achieved.
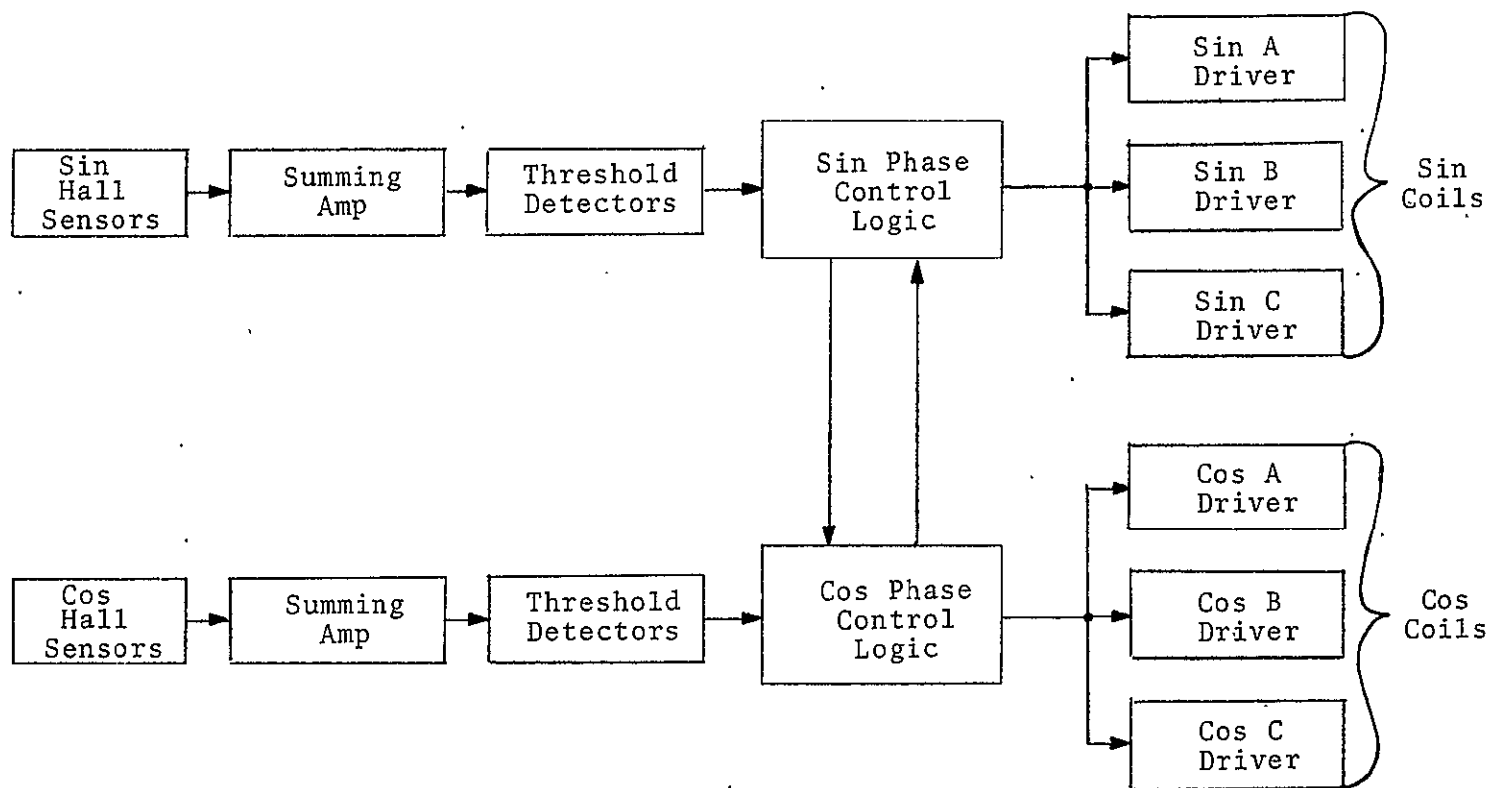
Figure 5-1 Motor Control Electronics.

6.0 REFERENCES

1. Anderson, Willard W.; and Groom, Nelson J.: The Annular Momentum Control Device (AMCD) and Potential Applications. NASA TN D-7866, 1975.

APPENDIX A

CURRENT DRIVER EQUATIONS AND TRANSFER FUNCTIONS

Appendix A
Current Driver Equations and Transfer Functions

When using current drivers, the usual tendency is to ignore the
high frequency dynamics and simply say that the output current is
just the input voltage times a constant. This was very mis-
leading in the case of AMCD as shown in Appendix C. The circuit
diagram of a current driver with voltage feedback and its equi-
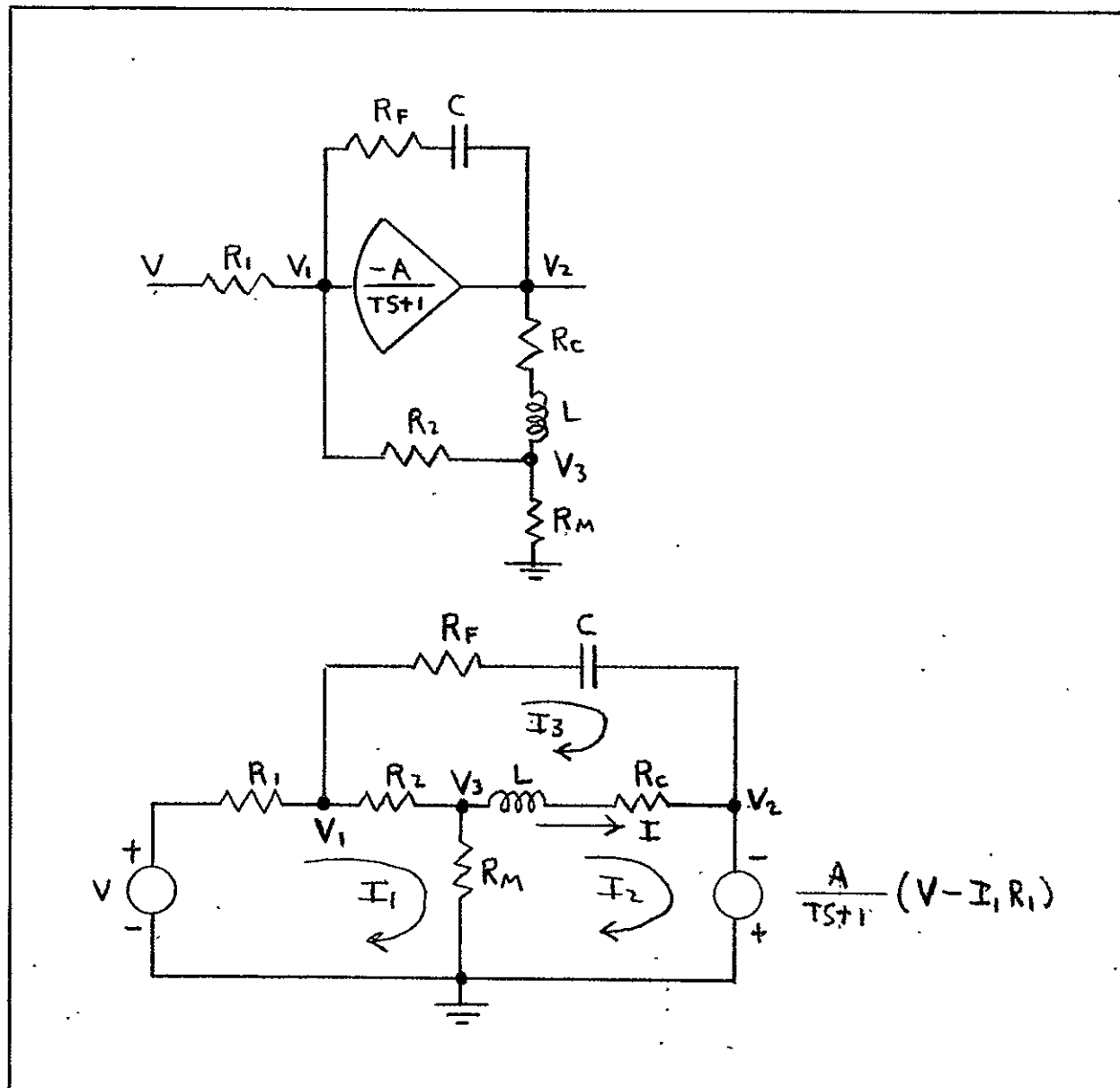valent diagram are shown in Figure A-1.

Figure A-1 Current Driver and Equivalent Circuit

The beginning equations of motion are the following:

$$\begin{bmatrix} R_{11} & -R_M & -R_2 \\ -R_M & SL + R_{22} & -(SL + R_C) \\ -R_2 & -(SL + R_C) & SL + R_{33} + S^{-1}C^{-1} \end{bmatrix} \begin{pmatrix} I_1 \\ I_2 \\ I_3 \end{pmatrix} = \begin{pmatrix} 1 \\ A(TS+1)^{-1} \\ 0 \end{pmatrix} V + \begin{pmatrix} 0 \\ -AR_1(TS+1)^{-1} \\ 0 \end{pmatrix} I_1$$

where

$$R_{11} \triangleq R_1 + R_2 + R_M$$

$$R_{22} \triangleq R_M + R_C$$

$$R_{33} \triangleq R_2 + R_F + R_C$$

Transposing I_1 to the left hand side we obtain:

$$\begin{bmatrix} R_{11} & -R_M & -R_2 \\ -R_M(TS+1) + AR_1 & (TS+1)(SL+R_{22}) & -(TS+1)(SL+R_C) \\ -SR_2 & -S(SL+R_C) & S^2L+SR_{33}+C^{-1} \end{bmatrix} \begin{pmatrix} I_1 \\ I_2 \\ I_3 \end{pmatrix} = \begin{pmatrix} 1 \\ A \\ 0 \end{pmatrix} V$$

What we really want is the current through the inductance

$$= I_2 - I_3$$

Adding this equation to the system we obtain:

$$\begin{bmatrix} C_{11} & C_{12} & C_{13} & 0 \\ B_{21}S+C_{21} & A_{22}S^2+B_{22}S+C_{22} & A_{23}S^2+B_{23}S+C_{23} & 0 \\ B_{31}S & A_{32}S^2+B_{32}S & A_{33}S^2+B_{33}S+C_{33} & 0 \\ 0 & -1 & 1 & 1 \end{bmatrix} \begin{pmatrix} I_1 \\ I_2 \\ I_3 \\ I \end{pmatrix} = \begin{pmatrix} 1 \\ A \\ 0 \\ 0 \end{pmatrix} V$$

where by definition

$$C_{11} = R_{11} \qquad B_{22} = L + TR_{22} \qquad A_{32} = -L$$

$$C_{12} = -R_M \qquad C_{22} = R_{22} \qquad B_{32} = -R_C$$

$$C_{13} = -R_2 \qquad A_{23} = -TL \qquad A_{33} = L$$

$$B_{21} = -R_M T \qquad B_{23} = -L - TR_C \qquad B_{33} = R_{33}$$

$$C_{21} = AR_1 - R_M \qquad C_{23} = -R_C \qquad C_{33} = C^{-1}$$

$$A_{22} = TL \qquad B_{31} = -R_2$$

If the voltage feedback is removed, these equations reduce very simply to:

$$\begin{bmatrix} R_1 + R_2 + R_M & -R_M \\ -R_M(TS+1) + AR_1 & (SL + R_C + R_M)(TS+1) \end{bmatrix} \begin{pmatrix} I_1 \\ I_2 \end{pmatrix} = \begin{pmatrix} 1 \\ A \end{pmatrix} V$$

where I_2 is the current through the inductance. We want the transfer function I_2/V. First divide the second equation through by LT to obtain

$$\begin{bmatrix} R_1 + R_2 + R_M & -R_M \\ -R_M L^{-1}(S+T^{-1}) + L^{-1}T^{-1}AR_1 & \left[S + L^{-1}(R_C + R_M)\right](S+T^{-1}) \end{bmatrix} \begin{pmatrix} I_1 \\ I_2 \end{pmatrix} = \begin{pmatrix} 1 \\ AL^{-1}T^{-1} \end{pmatrix} V$$

A-4

Then, by Cramer's rule

$$\frac{I_2}{V} = \frac{(R_1+R_2+R_M)AL^{-1}T^{-1}+R_ML^{-1}(S+T^{-1})-L^{-1}T^{-1}AR_1}{(R_1+R_2+R_M)(S+T^{-1})\left[S+L^{-1}(R_C+R_M)\right]-R^2_ML^{-1}(S+T^{-1})+L^{-1}T^{-1}AR_1R_M}$$

$$= \frac{(R_2+R_M)AL^{-1}T^{-1}+R_ML^{-1}(S+T^{-1})}{(R_1+R_2+R_M)(S+T^{-1})(S+L^{-1}R_C)+L^{-1}R_M(R_1+R_2)(S+T^{-1})+L^{-1}T^{-1}AR_1R_M}$$

Further manipulation yields

$$\frac{I_2}{V} = \frac{R_ML^{-1}}{(R_1+R_2+R_M)}\frac{S+T^{-1}+(R_2+R_M)AR_M^{-1}T^{-1}}{(S+T^{-1})(S+L^{-1}R_C)+\frac{L^{-1}R_M(R_1+R_2)}{R_1+R_2+R_M}\left[S+T^{-1}+\frac{\cancel{L^{-1}}T^{-1}AR_1\cancel{R_M}}{\cancel{L^{-1}}\cancel{R_M}(R_1+R_2)}\right]}$$

Finally, the desired current driver without voltage feedback transfer function is given by

$$\frac{I_2}{V} = \frac{R_ML^{-1}}{(R_1+R_2+R_M)}\frac{S+T^{-1}\left[1+A(1+R_2R_M^{-1})\right]}{(S+T^{-1})(S+L^{-1}R_C)+\frac{L^{-1}R_M(R_1+R_2)}{R_1+R_2+R_M}\left\{S+T^{-1}\left[1+\frac{AR_1}{R_1+R_2}\right]\right\}}$$
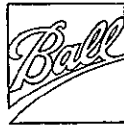
For infinite amplifier open loop gain, $A = \infty$, the transfer function reduces to

$$\lim_{A \to \infty} \frac{I_2}{V} = \frac{R_M^{-1}}{R_1 + R_2 + R_M} \cdot \frac{L^{-1}(1+R_2R_M^{-1})}{\frac{L^{-1}R_M(R_1+R_2)L^{-1}R_1}{(R_1+R_2+R_M)(R_1+R_2)}}$$

$$= \frac{(1+R_2R_M^{-1})}{R_1} = \frac{R_2}{R_1}\left(\frac{1}{R_2} + \frac{1}{R_M}\right) \cong \frac{R_2}{R_1R_M} \text{ for } R_2 >> R_M$$
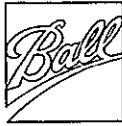
This is the transfer function which is used

$$\frac{I_2}{V} = \frac{R_2}{R_1R_M}$$

if the high frequency roots may be ignored.

When the high frequency roots are not to be ignored and

$$\text{if} \quad A, R_2, R_1 >> \max(R_M, R_C, 1)$$

$$\text{and} \quad \frac{R_M A R_1}{R_1 + R_2} >> R_C$$

A-6

The transfer function simplifies to

$$\frac{I_2}{V} = \frac{R_M L^{-1}}{R_1+R_2} \cdot \frac{S+T^{-1}AR_2 R_M^{-1}}{(S+T^{-1})(S+L^{-1}R_C)+L^{-1}R_M(S+T^{-1}AR_1/R_1+R_2)}$$

$$= \frac{R_M L^{-1}}{R_1+R_2} \cdot \frac{S+T^{-1}AR_2 R_M^{-1}}{\underbrace{S^2+(T^{-1}+L^{-1}R_C+L^{-1}R_M)S+\dfrac{T^{-1}L^{-1}R_M AR_1}{R_1+R_2}}}$$

$$\cong S+\frac{T^{-1}+L^{-1}(R_C+R_M)}{2} \pm \sqrt{j \frac{R_M AR_1}{TL(R_1+R_2)}}$$

The dc gain of this transfer function reduces to the same transfer function used if the high frequency roots may be ignored, that is

$$\frac{I_2}{V} = \frac{R_2}{R_1 R_M}$$

For the radial MA-1 Current Driver

$$R_1 = 10. \ K\Omega \qquad R_2 = 2.711 \ K\Omega \qquad R_M = .1\Omega$$

$$R_C = 3.0 \ \Omega \qquad L = .0128 \ h \qquad T^{-1} = 30. \qquad A = 50119$$

Then the radial current driver without voltage feedback has the transfer function

$$\frac{I_2}{V} = \frac{.00061463(S+4.0762E10)}{S+136.09\pm j3040.0}$$
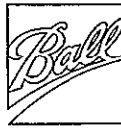
For the axial MA-1 current driver

R_1 = 10K $\qquad$ R_2 = 7.311K $\qquad$ C = .01 µf $\qquad$ R_{11} = 1.7311E4

L = .0064 $\qquad$ R_F = 1.2M $\qquad$ R_C = 1.4 $\qquad$ R_{22} = 1.5

A = 50119 $\qquad$ R_M = .1 $\qquad$ T^{-1} = 30 $\qquad$ R_{33} = 1.2073E6

Then

C_{11} = 1.7311E4 $\qquad$ B_{22} = 5.64E-2 $\qquad$ A_{32} = -.0064

C_{12} = -.1 $\qquad$ C_{22} = 1.5 $\qquad$ B_{32} = -1.4

C_{13} = -7.311E3 $\qquad$ A_{23} = -2.1333E-4 $\qquad$ A_{33} = .0064

B_{21} = -3.3333E-3 $\qquad$ B_{23} = -5.3067E-2 $\qquad$ B_{33} = 1.2073E6

C_{21} = 5.0119E8 $\qquad$ C_{23} = -1.4 $\qquad$ C_{33} = 1.0E8

A_{22} = 2.1333E-4 $\qquad$ B_{31} = -7.311E3

Without voltage feedback, the axial current driver has the transfer function

$$\frac{I_2}{V} = \frac{.00090261(S+1.0993E11)}{S+132.19 \pm j3683.9}$$

Note that without voltage feedback the damping ratio on both the radial and axial current driver high frequency roots is less than .05. This appears to be all right for the radial servos but is very bad for the axial servos as shown in Appendix C. Consequently, voltage feedback has not been employed for the radial servo's current drivers but has for the axial servo's current drivers.

The effects of this feedback has been determined numerically. Figure A-2(A) shows the effect of increasing R_F, the voltage feedback resistor, from zero to infinity with the feedback capacitor C held at .01 µf. If only the capacitor is used for voltage feedback, the current driver roots are still lightly damped but at a much lower frequency. As the resistance is increased the roots increase in damping, become real, then decrease in damping at a high frequency, finally moving to the no voltage feedback position for $R_F = \infty$. Figure A-2(B) shows the effect of increasing the voltage feedback capacitor C from zero to infinity while holding the feedback resistor at one megohm. For C = 0, the roots start at the no voltage feedback position. As C is increased the roots decrease in frequency and increase in damping ratio until C = .00091 µf. Further increases result in decreased damping ratio and increased frequency. At the chosen voltage feedback values of C = .01 µf, R_F = 1.0 MΩ, the axial current driver transfer function is

$$\frac{I}{V} = \frac{.0008994(S+83.3)(S+1.099E11)}{(S+78.6)(S+2771\pm j2583)}$$

Varying R_F for C=.01 μf
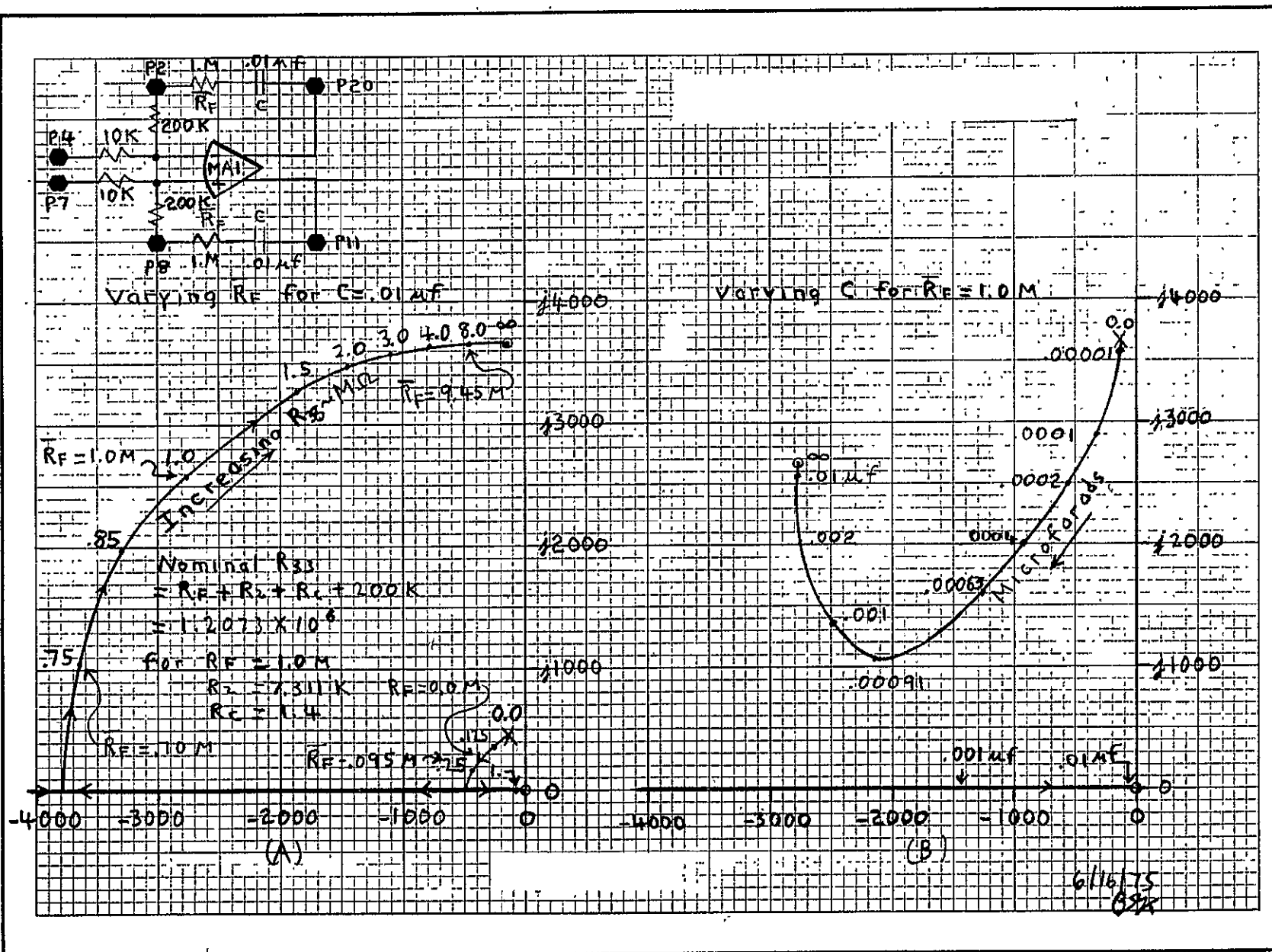
Varying C for R_F=1.0 M

P2 1.M .01μf

P20

R_F C

200K

P4 10K

P7 10K MA1

200K

R_F C

P8 1.M .01μf

P11

1.5 2.0 3.0 4.0 8.0 ∞

Increasing R_33 MΩ   R_F=9.45M

R_F=1.0 M 1.0

.85

Nominal R_33

= R_F + R_2 + R_1 + 200k

= 1.2073 × 10^6

.75 for R_F = 1.0 M

R_2 = 7.311 K   R_F=0.0 M

R_1 = 1.4

R_F=.10 M   R_F=.095 M   0.0

.175

1.7

+4000

+3000

+2000

+1000

.01μf

.002

.001

.00063

.00091

.0001

.0002

.0004

.01μf

.001μf .01μf

+4000

+3000

+2000

+1000

0.0

.00001

-4000 -3000 -2000 -1000 0

-4000 -3000 -2000 -1000 0

(A)

(B)

6/16/75

Figure A-2 Effect of Voltage Feedback on AMCD Axial Current Driver

APPENDIX B

THE WAHOO CONCEPT

Appendix B
The WAHOO Concept

Introduction

Two conditions may occur which cause the radial electromagnets
to draw more current than necessary. First, if the rim is tipped,
a gravitational force tends to pull the rim sideways. This force
is countered by the servos at the expense of causing the electro-
magnets to draw more current. Second, as the rim spins up,
centrifugal forces cause it to expand. To each radial sensor,
this expansion is viewed as rim movement to be countered by the
servos. So, each electromagnet draws more current to try to pull
the rim inward. But since the forces are all directed inward and
spaced 120° around the rim, the resultant of the forces is zero
so the rim does not move. The net result of the expansion then
is that only the current in the electromagnets increases. Trim
loops are developed in this appendix which lead to VZP (Virtually
Zero Power) operation for the radial servos when either the rim
is tipped or expands or both. The system employing these trim
loops is called the WAHOO system.

Because the three radial servos are controlling only two degrees
of freedom, the radial servo system is very highly coupled. This
very high degree of coupling makes it difficult to design each
servo as a single uncoupled system. Hence, in this appendix we
also develop equations to show how the three-servo radial system
may be designed using a single station servo radial equivalent.

Development of the WAHOO Concept

The AMCD rim is suspended radially by three servos pulling on
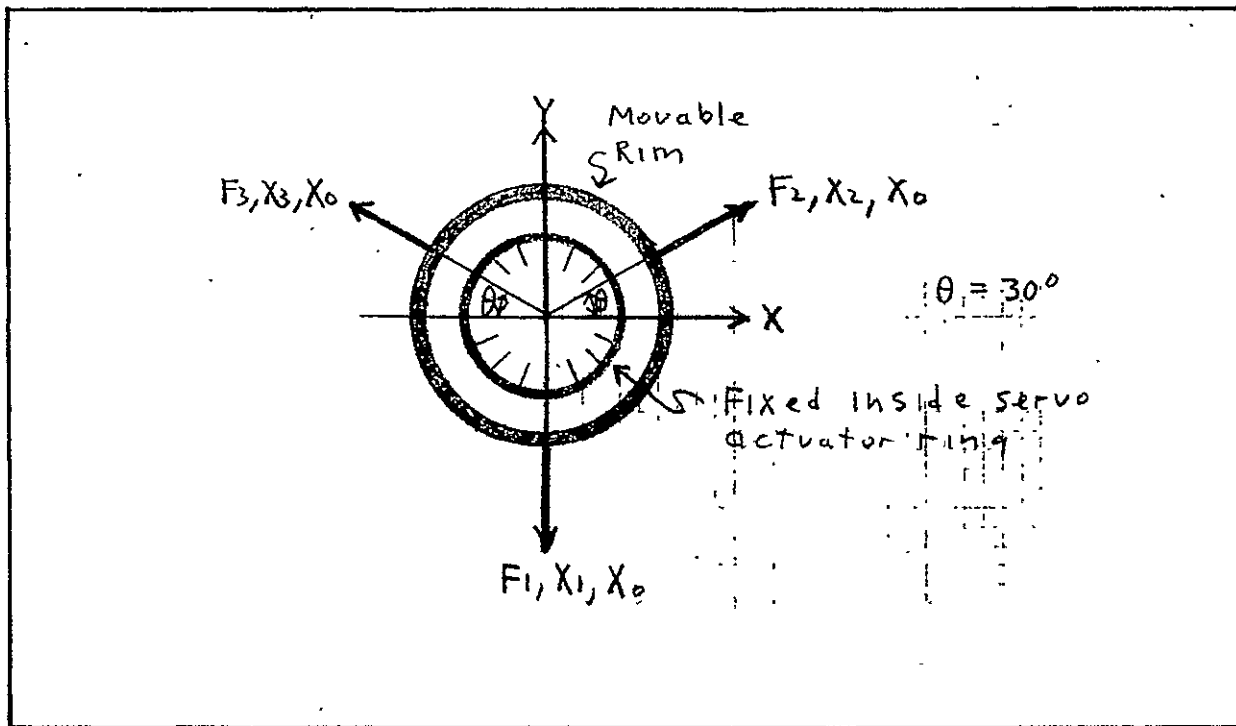it from the inside much like shown in Figure B-1.

Figure B-1   Radial Servo Sign Convention

The sensor outputs are denoted by X_1, X_2, and X_3. As the rim spins up, it expands by the amount X_0. The sign convention is chosen such that positive forces and displacements are outwards. The equations of motion of the rim are:

$$(F_2 - F_3)C\theta = M\ddot{X}$$

$$(F_2 + F_3)S\theta - F_1 = M\ddot{Y}$$

$$X_2 = XC\theta + YS\theta$$

$$X_3 = -XC\theta + YS\theta$$

$$X_1 = -Y \qquad\qquad\qquad\qquad (B-1)$$

The force acting at each station is composed of a permanent magnet force and an electromagnet force. That is:

$$F_1 = P(X_1 + X_0) + E\,D_1$$

$$F_2 = P(X_2 + X_0) + E\,D_2 \qquad\qquad \text{(B-2)}$$

$$F_3 = P(X_3 + X_0) + E\,D_3$$

These equations are combined with the servo equations in Figure B-2.

From the block diagram, the equations of motion using five variables are:

$$V_1 = K_P(-Y + X_0) - (1/S)(K_S V_1 + K_C V_2 + K_C V_3)$$

$$\ddot{Y} = M^{-1}\{-P(-Y+X_0) + \frac{EK_R N}{D}(-Y+X_0) + EV_1 + PS\Theta(YS\Theta + XC\Theta + X_0)$$

$$-\frac{EK_R N}{D}\,S\Theta(YS\Theta + XC\Theta + X_0) - ES\Theta V_2 + PS\Theta(YS\Theta - XC\Theta + X_0)$$

$$-\frac{EK_R N}{D}\,S\Theta(YS\Theta - XC\Theta + X_0) - ES\Theta V_3 + F_Y\}$$

$$V_2 = K_P(YS\Theta + XC\Theta + X_0) - (1/S)(K_S V_2 + K_C V_1 + K_C V_3)$$

$$\ddot{X} = M^{-1}\{PC\Theta(YS\Theta + XC\Theta + X_0) - \frac{EK_R N}{D}\,C\Theta(YS\Theta + XC\Theta + X_0) - EC\Theta V_2$$

$$-PC\Theta(YS\Theta - XC\Theta + X_0) + \frac{EK_R N}{D}\,C\Theta(YS\Theta - XC\Theta + X_0) + EC\Theta V_3\}$$

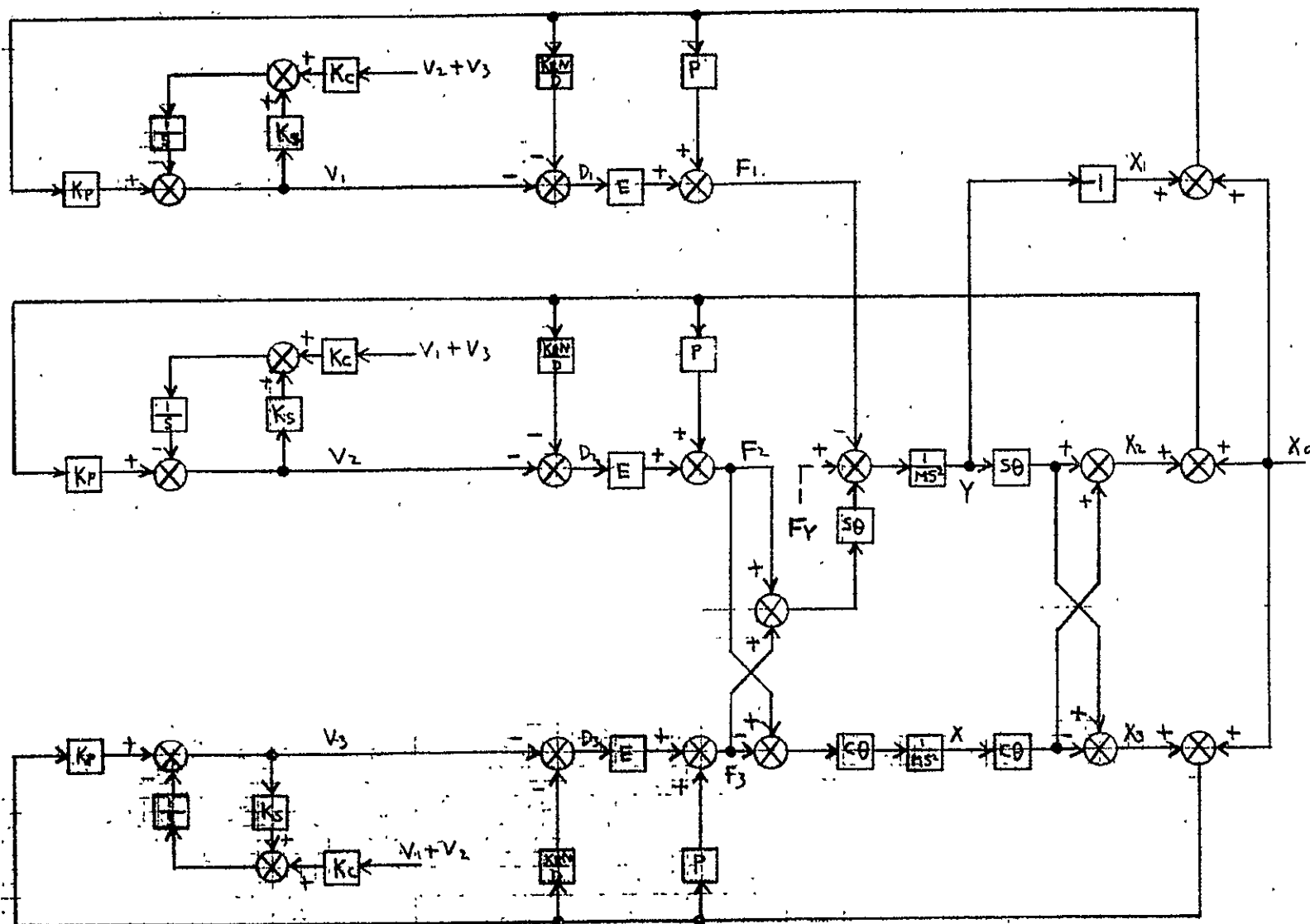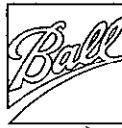$$V_3 = K_P(YS\Theta - XC\Theta + X_0) - (1/S)(K_S V_3 + K_C V_1 + K_C V_2) \qquad\qquad \text{(B-3)}$$

Figure B-2 AMCD Radial Servos With Trim Loops

Rearranging,

- $(S+K_S)V_1+K_PSY+K_CV_2+K_CV_3 = K_PSX_0$

- $-M^{-1}DEV_1+[DS^2-DM^{-1}P(1+2S^2\Theta)+M^{-1}EK_RN(1+2S^2\Theta)]Y$

  $+M^{-1}DES\Theta V_2+M^{-1}DES\Theta V_3 = [M^{-1}DP(-1+2S\Theta)+M^{-1}EK_RN(1-2S\Theta)]X_0+M^{-1}DF_Y$

- $K_CV_1-K_PS\Theta SY+(S+K_S)V_2-K_PC\Theta SX+K_CV_3 = K_PSX_0$

- $M^{-1}DEC\Theta V_2+[DS^2-DM^{-1}P(2C^2\Theta)+M^{-1}EK_RN(2C^2\Theta)]X-M^{-1}DEC\Theta V_3 = 0$

- $K_CV_1-K_PS\Theta SY+K_CV_2+K_PC\Theta SX+(S+K_S)V_3 = K_PSX_0$ (B-4)

Since $\Theta = 30°$

$$1+2S^2\Theta = 1+2(.5)^2 = 1.5$$

$$-1+2S\Theta = -1+2(.5) = 0$$

$$2C^2\Theta = 2(\frac{\sqrt{3}}{2})^2 = 1.5 \qquad (B-5)$$

Using these simplifications, the Laplace transformed radial servo equations of motion in matrix form are:

$$
\begin{bmatrix}
(S+K_S) & K_PS & K_C & 0 & K_C \\
-M^{-1}DE & \begin{matrix}DS^2 \\ +1.5M^{-1}EK_RN \\ -1.5M^{-1}DP\end{matrix} & .5M^{-1}DE & 0 & .5M^{-1}DE \\
K_C & -.5K_PS & (S+K_S) & -.5\sqrt{3}K_PS & K_C \\
0 & 0 & .5\sqrt{3}M^{-1}DE & \begin{matrix}DS^2 \\ +1.5M^{-1}EK_RN \\ -1.5M^{-1}DP\end{matrix} & -.5\sqrt{3}M^{-1}DE \\
K_C & -.5K_PS & K_C & .5\sqrt{3}K_PS & (S+K_S)
\end{bmatrix}
\begin{bmatrix} V_1 \\ Y \\ V_2 \\ X \\ V_3 \end{bmatrix}
=
\begin{bmatrix} K_PS \\ 0 \\ K_PS \\ 0 \\ K_PS \end{bmatrix} X_0
+
\begin{bmatrix} 0 \\ M^{-1}D \\ 0 \\ 0 \\ 0 \end{bmatrix} F_Y
$$

The system characteristic equation is the determinant of the coefficient matrix. With much algebraic effort, it can be reduced to

$$\Delta = (S+K_S+2K_C)X$$

$$[(S+K_S-K_C)(DS^2+1.5M^{-1}EK_RN-1.5M^{-1}DP)+1.5K_PM^{-1}DES]^2$$

<div align="right">(B-7)</div>

Now, let's simplify the expression by removing the high frequency roots. In the Cambion hardware.

$$\frac{K_RN}{D} = \frac{10^7 S}{(S+1000)(S+10000)} \cong S \text{ for low frequencies}$$

With this approximation $K_R = D = 1$ and $N = S$. Then,

$$\Delta = (S+K_S+2K_C)[(S+K_S-K_C)(S^2+1.5M^{-1}ES-1.5M^{-1}P)+1.5K_PM^{-1}ES]^2$$

So the roots separate into $-(K_S+2K_C)$ and two identical sets within the brackets. Immediately, we see that $K_S+2K_C \geq 0$ for stability. Now looking within the brackets, we see that $S^2+1.5M^{-1}ES-1.5M^{-1}P$ represents the permanent magnet roots at $\pm\sqrt{1.5M^{-1}P}$ moved to the left some by the rate feedback; however one remains in the right half plane. Taking these roots and the one at $-(K_S-K_C)$ as poles of a root locus plot and S as the zero, Figure B-3 shows that for stability $K_C \geq K_S$.
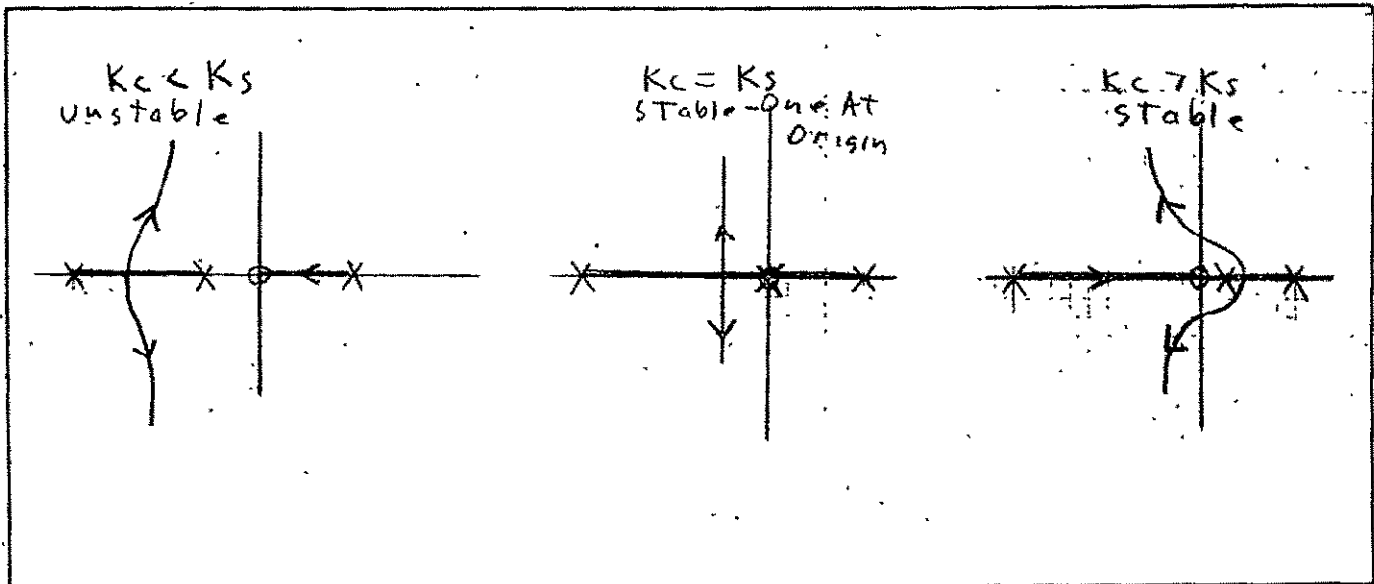
Figure B-3   Effect of Trim Loop Gains

Let's look at three special cases:
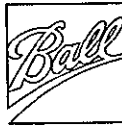
I. No Trim Loop: $K_C = K_S = 0$: No VZP

$$\Delta = S^3 [(S^2 + 1.5M^{-1}ES - 1.5M^{-1}P) + 1.5K_pM^{-1}E]^2 \tag{B-8}$$

There are three roots at the origin from the three unconnected integrators and two identical quadratic pairs. The system is stable.

II. No Cross Feed Trims: $K_C = 0$

$$\Delta = (S + K_S)[(S + K_S)(S^2 + 1.5M^{-1}ES - 1.5M^{-1}P) + 1.5K_pM^{-1}ES]^2 \tag{B-9}$$

This is unstable for both signs of K_S $\therefore$ self trim loops alone will not work.

III. No Self Feed Trim: $K_S = 0$: WAHOO SERVO

$$\Delta = (S+2K_C)[(S-K_C)(S^2+1.5M^{-1}ES-1.5M^{-1}P)+1.5K_pM^{-1}ES]^2$$

This can be made stable for all positive values of K_C.

IV. One Integrator Trim: $K_C = K_S \triangleq K$

$$\Delta = (S+3K)S^2[(S^2+1.5M^{-1}ES-1.5M^{-1}P)+1.5K_pM^{-1}E]^2 \qquad \text{(B-10)}$$

This can be made stable for all positive values of K.

- Main conclusion to here: Cross Feed is necessary for stability if VZP is needed. Self Feed is not.

Now a question arises. Do the two stable systems (III and IV) provide zero power operation in the face of both rim expansion and force disturbances and do they translate due to these effects? To answer this, look at the transfer function V_1/X_0, V_1/F_y, Y/X_0, and Y/F_y. From (B-6), after much algebraic manipulation, we obtain the numerators:

$$\text{Num }(V_1/X_0) = K_pS[(S+K_S-K_C)(DS^2+1.5M^{-1}EK_RN-1.5M^{-1}DP)+1.5K_pM^{-1}DES]^2$$

$$\text{(B-11)}$$

$$\text{Num }(V_1/F_y) = -M^{-1}DK_pS(S+K_S+2K_C)X$$
$$[(S+K_S-K_C)(DS^2+1.5M^{-1}EK_RN-1.5M^{-1}DP)+1.5K_pM^{-1}DES]$$

$$\text{(B-12)}$$

$$\text{Num } (Y/X_0) = 0 \tag{B-13}$$

$$\text{Num } (Y/F_y) = M^{-1}D(S+K_S+2K_C)(S+K_S-K_C)X$$

$$[(S+K_S-K_C)(DS^2+1.5M^{-1}EK_RN-1.5M^{-1}DP)+1.5K_PM^{-1}DES] \tag{B-14}$$

Repeating (B-7)

$$\Delta = (S+K_S+2K_C)[(S+K_S-K_C)(DS^2+1.5M^{-1}EK_RN-1.5M^{-1}DP)+1.5K_PM^{-1}DES]^2 \tag{B-7}$$

Then the transfer functions are

$$\frac{V_1}{X_0} = \frac{\text{Num } (V_1/X_0)}{\Delta} = \frac{K_PS}{(S+K_S+2K_C)} \tag{B-15}$$

$$\frac{V_1}{F_y} = \frac{\text{Num } (V_1/F_y)}{\Delta} = \frac{-M^{-1}DK_PS}{(S+K_S-K_C)(DS^2+1.5M^{-1}EK_RN-1.5M^{-1}DP)+1.5K_PM^{-1}DES} \tag{B-16}$$

$$\frac{Y}{X_0} = \frac{\text{Num } (Y/X_0)}{\Delta} = 0 \tag{B-17}$$

$$\frac{Y}{F_y} = \frac{M^{-1}D(S+K_S-K_C)}{(S+K_S-K_C)(DS^2+1.5M^{-1}EK_RN-1.5M^{-1}DP)+1.5K_PM^{-1}DES} \qquad \text{(B-18)}$$

Now we can answer the question.

- WAHOO Servo: $K_S = 0$

Because of the S in the numerators of V_1/X_0 and V_1/F_y the steady state power goes to zero for both rim expansion and force disturbances. From Y/X_0, the rim does not translate for rim expansion. From Y/F_y, the rim does translate for disturbance forces with a stiffness of

$$\left.\frac{F_y}{Y}\right|_{S=0} = -1.5P \qquad \text{(B-19)}$$

Therefore, the rim translates toward the disturbance.

- Single Integrator Trim: $K_C = K_S$

From V_1/X_0, the steady-state power goes to zero for rim expansion. With $K_C = K_S$, the S cancels out of the numerator of V_1/F_y; therefore, the system power is not zero for force disturbances. From Y/X_0, the system does not translate for rim expansion. From Y/F_y, the rim does translate for force disturbances with a stiffness of

$$\left.\frac{F_y}{Y}\right|_{S=0} = 1.5(K_PE-P) \qquad \text{(B-20)}$$
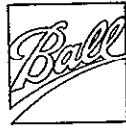
Therefore, the rim translates away from the disturbances with the same stiffness it has with no trim.

Radial Single Station Servo Equivalent

Because three servos are controlling only two degrees of freedom, the radial servo system is very highly coupled. This makes it difficult to design each servo as a single uncoupled system. From the characteristic equation $\Delta=0$ derived in the preceding section we may deduce a single station equivalent. From (B-7), considering only the WAHOO servo,

$$\Delta = (S+2K_C)[(S-K_C)(DS^2+1.5M^{-1}EK_RN-1.5M^{-1}DP)+1.5K_pM^{-1}DES]^2$$

$$(B-21)$$

We note that there is one root at $-2K_C$ and a repeated set of roots within the brackets. We would expect only two repeated sets because we are only controlling two degrees of freedom even though three servos are used to accomplish it. Looking at the quantity within the brackets

$$(S-K_C)(DS^2+1.5M^{-1}EK_RN-1.5M^{-1}DP)+1.5K_pM^{-1}DES = 0 \qquad (B-22)$$

we first divide through by $S^2D(S-K_C)$ to obtain

$$1 + \frac{E}{2/3\ M}\frac{K_RN}{DS^2} - \frac{P}{2/3\ MS^2} + \frac{K_pE}{2/3\ MS^2}\frac{S}{S-K_C} = 0 \qquad (B-23)$$

This is just the characteristic equation of the following servo, which is the single station equivalent.
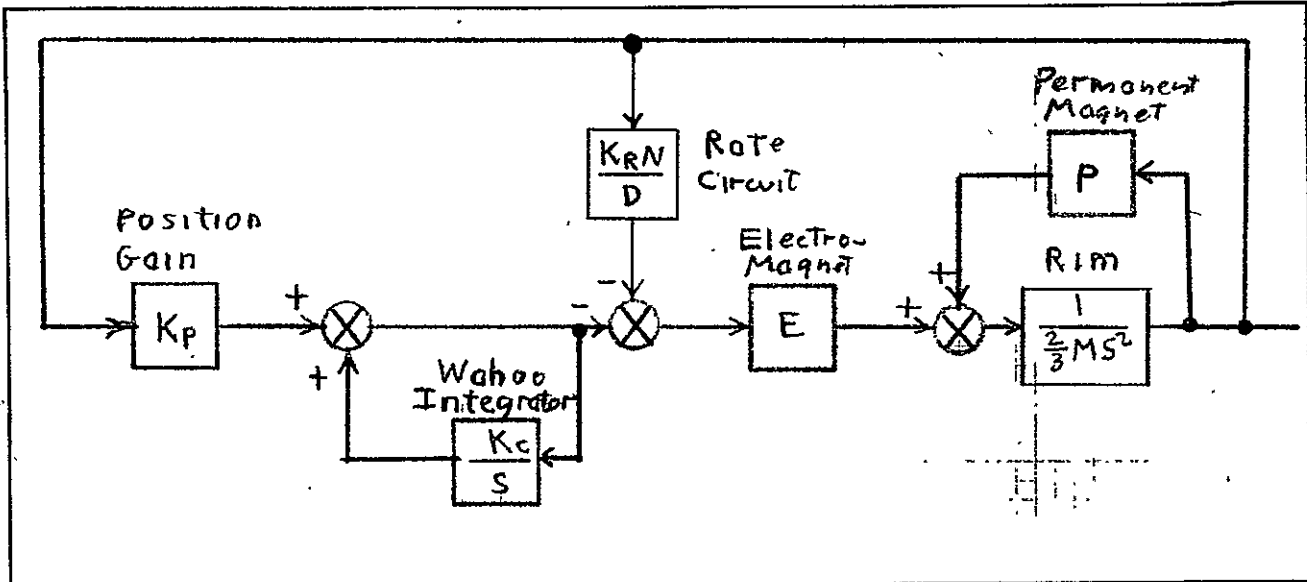

Figure B-4   Equivalent Single Radial Servo Station

Two points of interest are immediately evident.   The equivalent mass is 2/3 the total rim mass.   The WAHOO concept which involves negative feedback to each station from the sum of the other two stations resolves to a positive feedback in the single station representation exactly like VZP in the axial mode. Using this single station equivalent, the system may be designed just like an uncoupled servo, the final three-servo coupled system roots being given by (B-21).

Conclusions

- Only the WAHOO trim system is stable and produces zero steady-state power for both force disturbances and rim expansion. WAHOO trim consists of the sum of voltages from servos i and j being fed back to servo K in a negative sense for each i, j, and k.   That is, for trim purposes, each servo only monitors what the other two are doing-not itself.   The system stiffness is -1.5P where P is the permanent magnet stiffness at each station.

C.2

- The highly coupled three servo radial systems may be designed using a single station servo radial equivalent.

APPENDIX C

SOME ADDITIONAL SERVO INSIGHTS

Appendix C
Some Additional Servo Insights

The purpose of this appendix is to provide additional insight into the inner workings of the system. To build up a feel for the final axial system, a series of stability plots are shown to show the state of the system at various stages of its design.

The axial servos were originally designed assuming an ideal current driver, that is, one whose output current is just a constant times the input voltage. This is what is usually assumed concerning current drivers. Figure C-1 is the axial position mode root locus plot of such a system. It indicates that no stability problems exist, an upper gain margin of 120.6 and a lower gain margin of .22 being evident. The actual servo did not exhibit such stability.

Figure C-2 shows the same root locus plot (that is, axial position mode) if a realistic current driver is used. The realistic current driver has low damped (ζ = .036) high frequency roots (ω = 3685 rad/sec) which are driven unstable at a gain of 4.79 (compared with 120.6 above). The actual servo exhibited this instability at even lower gain margins. At the times we were experiencing this instability, the root locus plot of Figure C-2 had not been made. Indeed, the realistic current driver transfer function had not even been derived. We did, however, suspect the current driver and fixed the problem experimentally by trying different values of components in the voltage feedback circuit. We eventually arrived at C = .01 µf and R_F = 1.0 MΩ for feedback components. Appendix A shows that this was a near optimum choice. Figure 4-10 shows that this fix increaseds the systems gppnrmgain margin from 4.79 to 20.1.

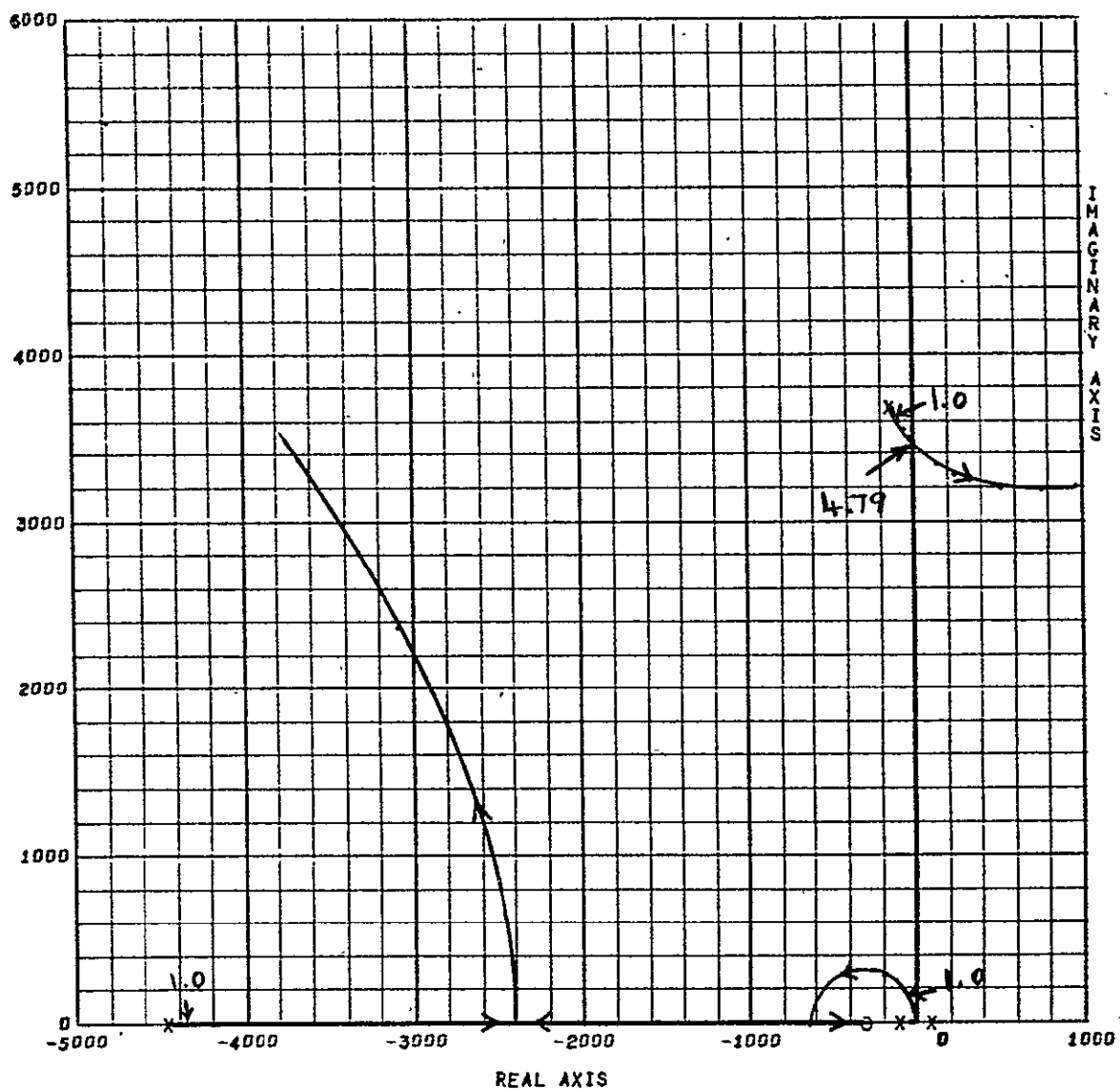Figure C-1 AMCD Axial Servo With Ideal Current Driver

Figure C-2 Root Locus Plot Nonideal Current Driver Without
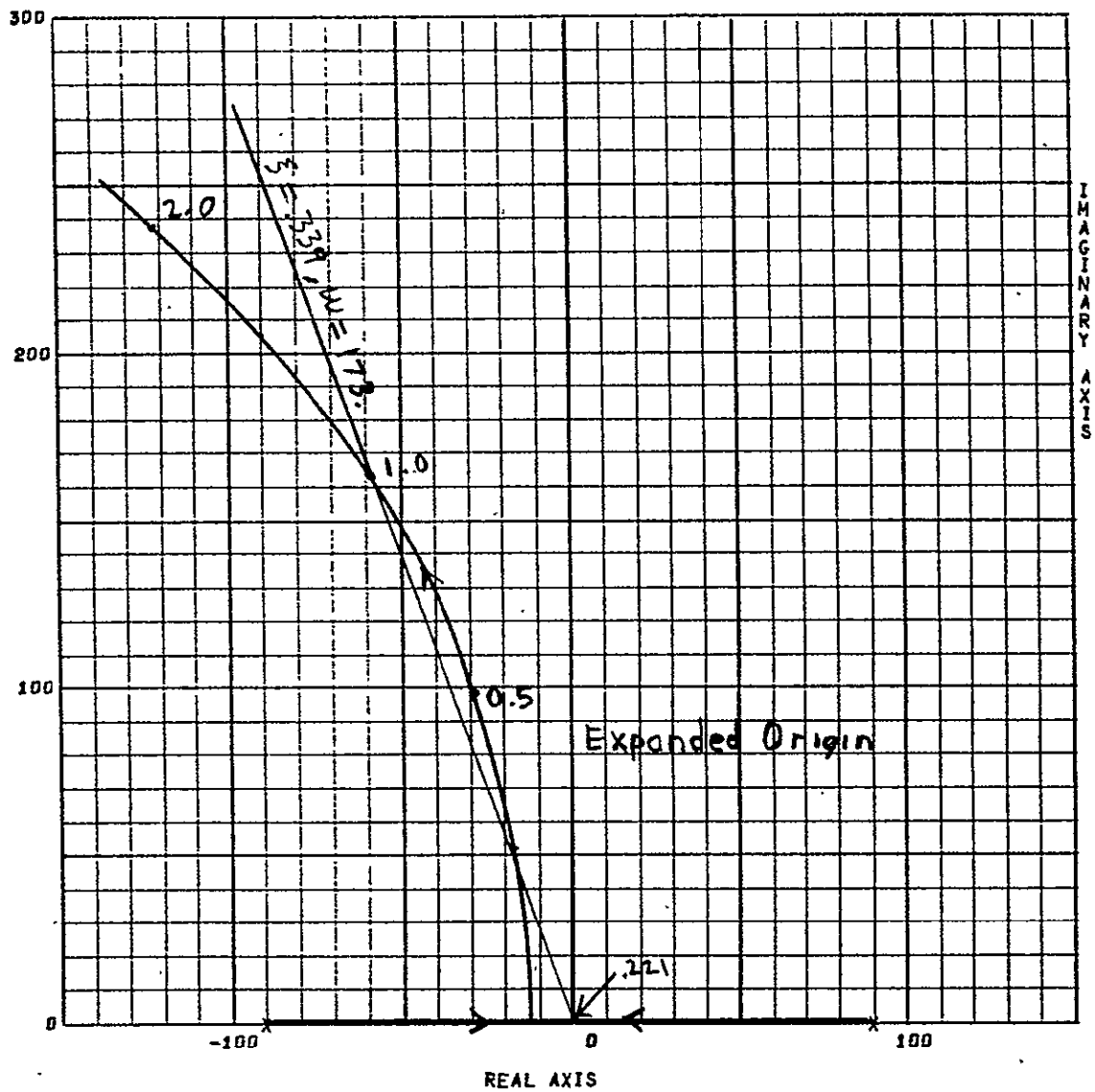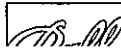Voltage Feedback

Figure C-2(B) Root Locus Plot - Nonideal Current Driver
Without Voltage Feedback

The final axial system root locus and Bode plots are shown in Figures 4-10 and 4-11 for the position mode and in Figures 4-12 and 4-13 for the VZP mode. Sometimes, additional insight may be obtained from other stability plots. The axial position mode and VZP mode Nyquist plots are shown in Figures C-3 and C-4. A plot which yields root sensitivity information from both changes in gain and phase is the gain phase root locus plot. Gain-phase root locus plots for the axial position and VZP modes appears in Figures C-5 and C-6. For example, Figure C-5 reveals that if the gain remained nominal and for some unknown reason an additional 23.2° of phase lag were introduced, the axial position mode would go unstable.
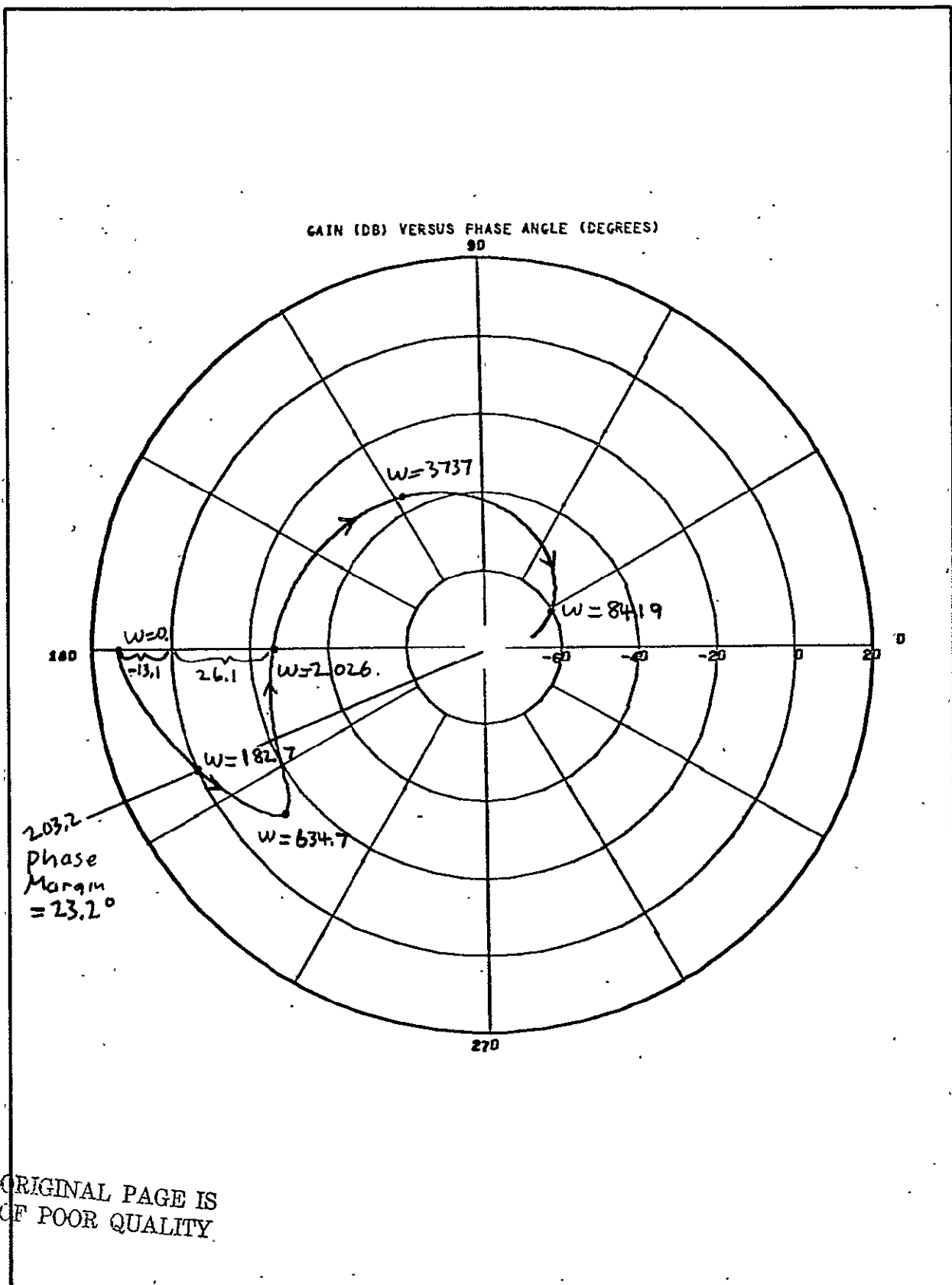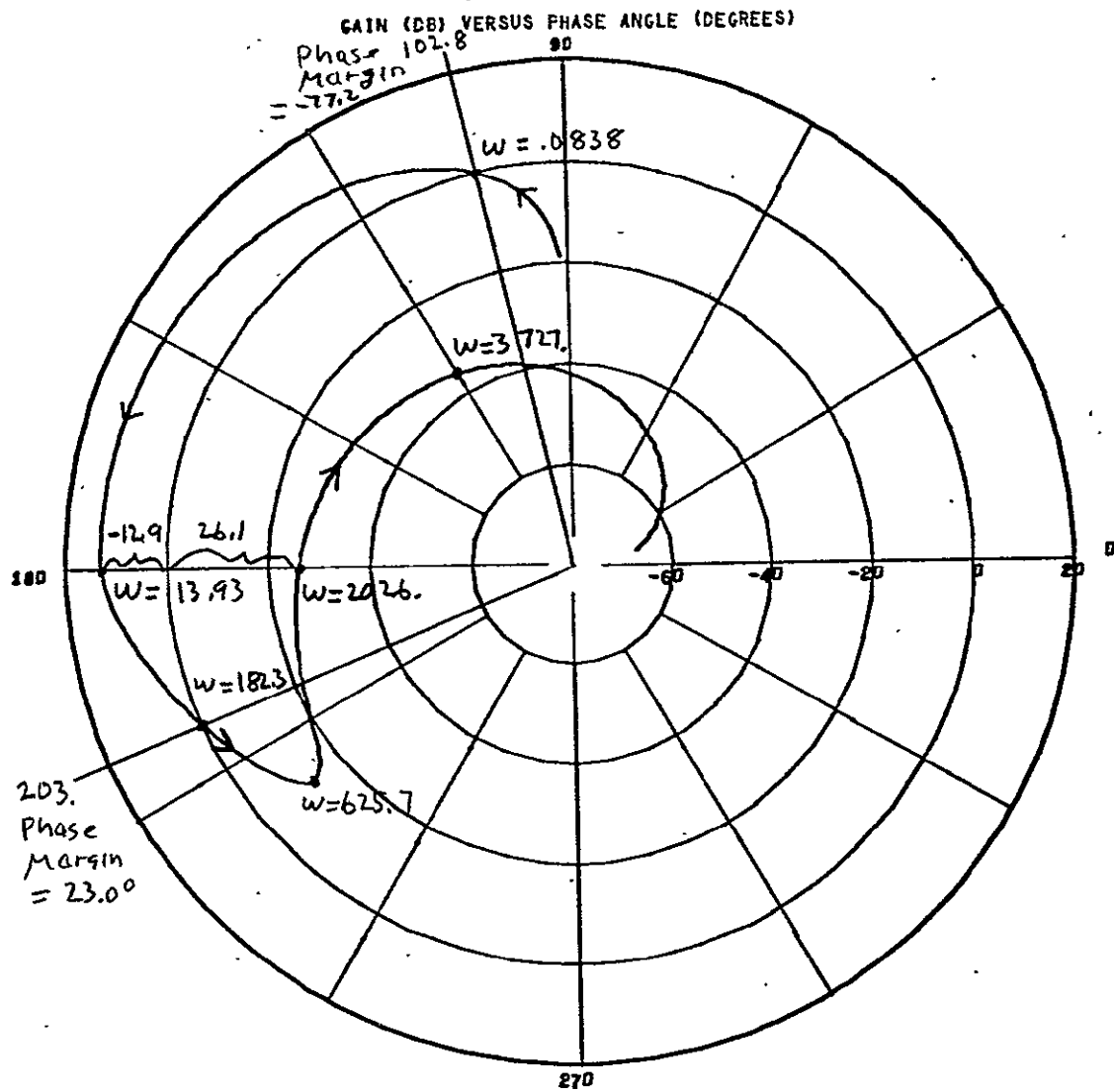
CAIN (DB) VERSUS PHASE ANGLE (DEGREES)

W=3737

W=84.19

W=0.
-13.1   26.1   W=2.026.

W=182.7

W=634.7

203.2
Phase
Margin
=23.2°

Figure C-3   Nyquist Plot - Nonideal Current Driver With
Voltage Feedback

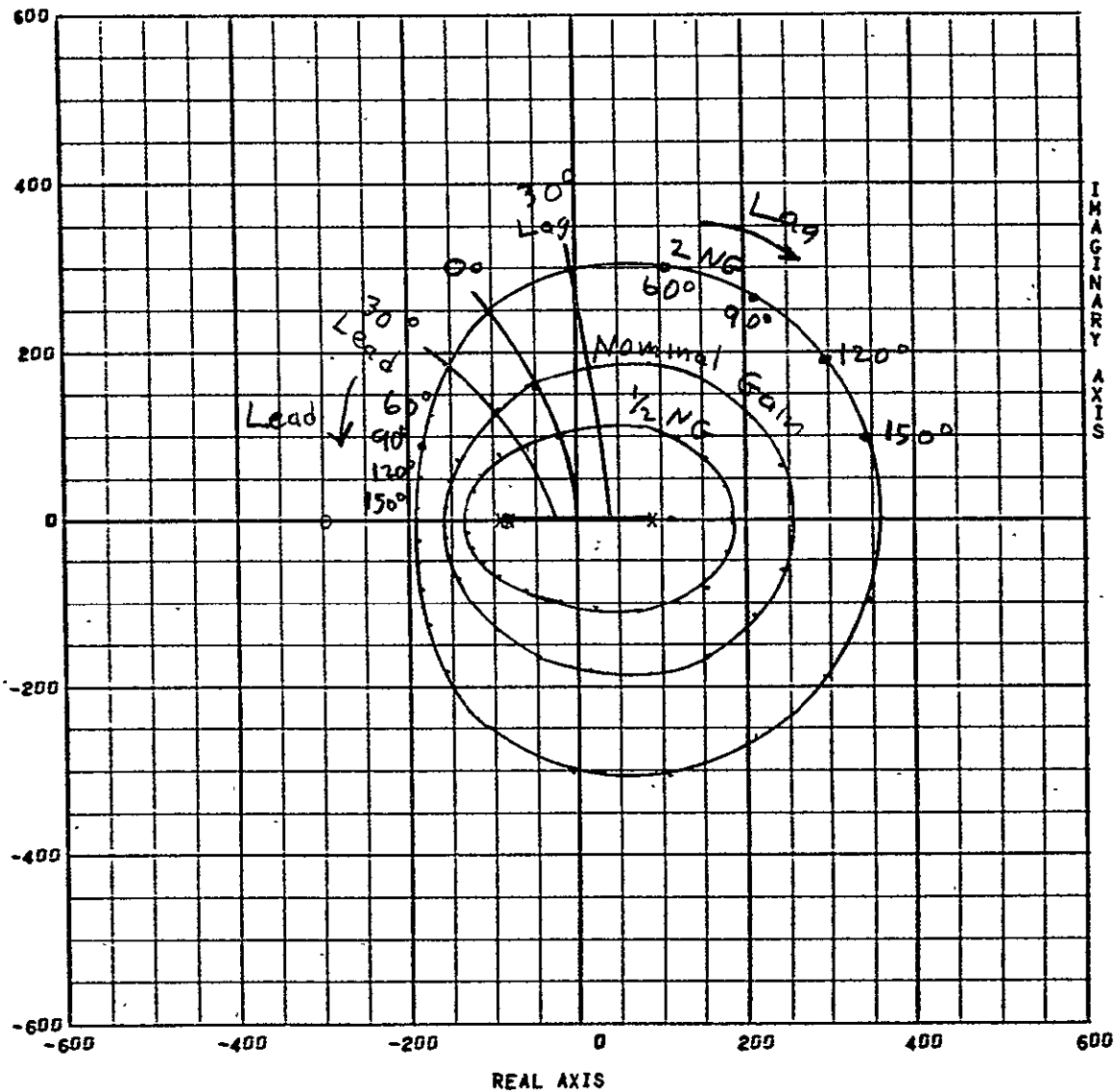Figure C-4   Nyquist Plot -- Nonideal Current Driver With
Voltage Feedback

Figure C-5 Gain-Phase Root Locus Plot - Nonideal Current Driver
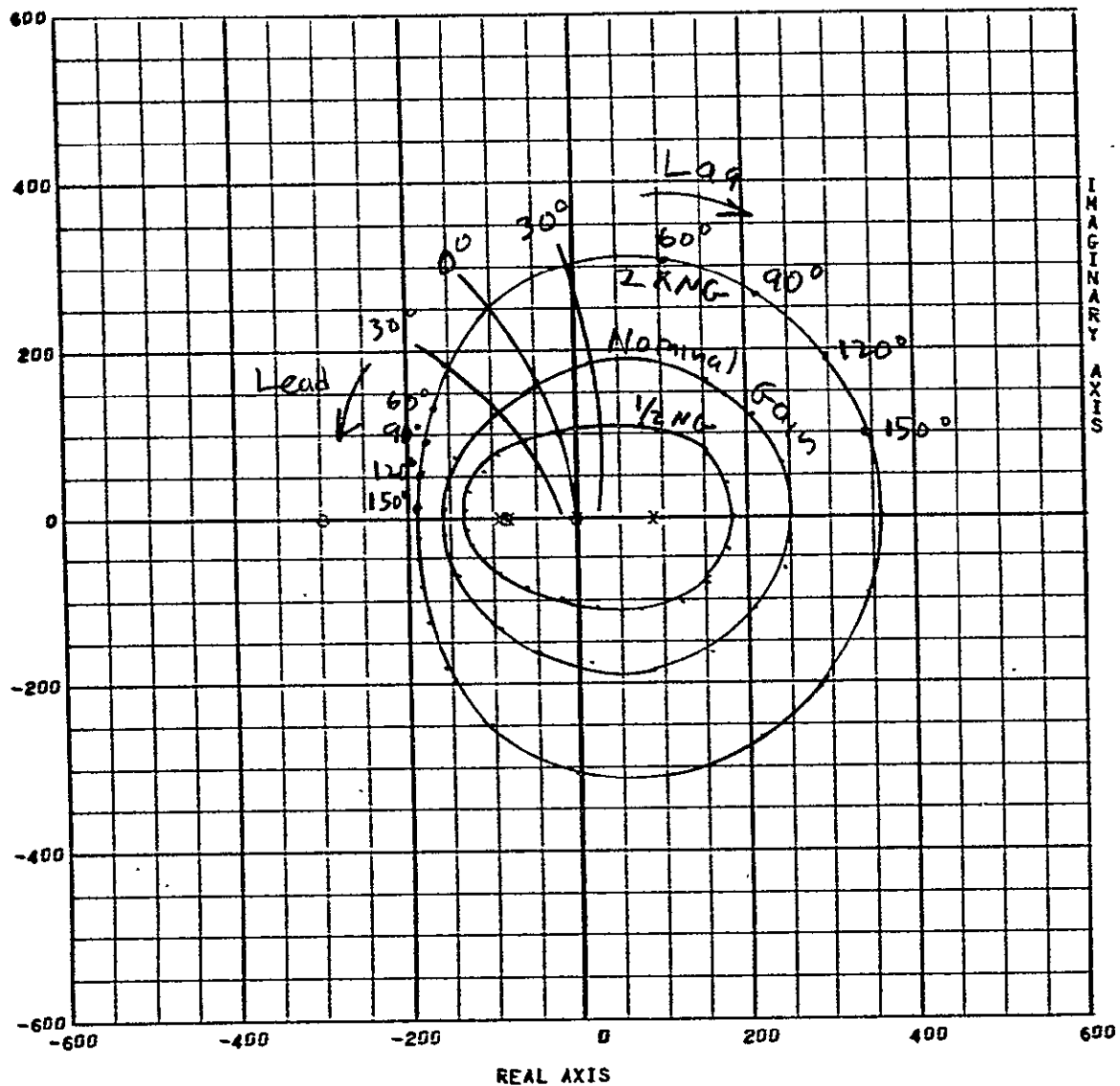With Voltage Feedback

Figure C-6 Gain-Phase Root Locus Plot - Nonideal Current Driver
With Voltage Feedback